Search for Third Generation Squarks in the Missing Transverse Energy plus Jet Sample at CDF Run II

Búsquedas de squarks de la tercera familia en sucesos con jets y momento transverso neto en el experimento CDF run II

CIEMAT
and
Departamento de Física Atómica, Molecular y Nuclear
(Universidad Complutense de Madrid)

PhD Dissertation
Miguel Vidal Maroño
to apply for the degree of Doctor of Philosophy in Physics.

Supervised by
Dr. Oscar González López

March 2010

Dr. Oscar González López, investigador titular del Departamento de Investigación Básica, del Centro de Investigaciones Energéticas, Medioambientales y Tecnológicas (CIEMAT),

Certifica:

Que la presente memoria: **"Search for Third Generation Squarks in the Missing Transverse Energy plus Jet Sample at CDF Run II"**, ha sido realizada bajo mi dirección en el Departamento de Física Atómica, Molecular y Nuclear de la Facultad de Ciencias Físicas de la Universidad Complutense de Madrid por *Miguel Vidal Maroño,* para optar al grado de Doctor en Ciencias Físicas.

Y para que así conste, en cumplimiento de la legislación vigente, presento ante la Universidad Complutense de Madrid esta memoria, firmando el presente certificado:

Madrid, a 23 de noviembre de 2009

Contents

List of Figures

List of Tables

Chapter 1

Introduction

The twentieth century leaves behind one of the most impressive legacies, in terms of human knowledge, ever achieved. In particular the Standard Model (SM) of particle physics has proven to be one of the most accurate descriptions of Nature. The level of accuracy of some theoretical predictions has never been attained before. It includes the electromagnetic interaction, and the weak and strong force, developing the Lagrangian from symmetry principles.

There are two different types of fundamental constituents of Nature, in the framework of the Standard Model: bosons and fermions. Bosons are those particles responsible for carrying the interactions among the fermions, which constitute matter. Fermions are divide into six quarks and six leptons, forming a three-folded structure. All these fermions and bosons have an antimatter partner.

However, several difficulties point along with the idea that the Standard Model is only an effective low energy theory. These limitations include the difficulty to incorporate gravity and the lack of justification to fine tuning of some perturbative corrections. Moreover, some regions of the theory are not understood, like the mass spectrum of the Standard Model or the mechanism for electroweak symmetry breaking.

Supersymmetry is a newer theoretical framework, thought to adress the problems found in the Standard Model, while preserving all its predictive power. It introduces a new symmetry that relates a new boson to each SM fermion and a new fermion to each SM boson. In this way, for every existing boson in the SM it must exist a fermionic super-partner (named with a sufix ino), and likewise, for every fermion a bosonic super-partner (named with a prefix s) must also exist. Moreover, another symmetry called R-parity is introduced to prevent baryon and lepton number violating interactions. If R-parity is conserved, super-particles can only be

pair-produced and they cannot decay completely in SM particles. This implies the existence of a lightest SUSY particle (LSP) which would provide a candidate for cold dark matter, that account for 23% of the universe content, as strongly suggested by recent astrophysical data [1].

The Tevatron is a hadron collider operating at Fermilab, USA. This accelerator provides proton-antiproton ($p\bar{p}$) collisions with a center of mass energy of $\sqrt{s}$ =1.96 TeV. CDF and DØ are the detectors built to analyse the products of the collisions provided by the Tevatron. Both experiments have produced a very significant scientific output in the last few years, like the discovery of the top quark or the measurement of the B_s mixing. The Tevatron experiments are also reaching sensitivity to the SM Higgs boson.

The scientific program of CDF includes a broad spectrum on searches for physics signatures beyond the Standard Model. Tevatron is still the energy frontier, what means an unique opportunity to produce a discovery in physic beyond the Standard Model.

The analyses presented in this thesis focus on the search for third generation squarks in the missing transverse energy plus jets final state. The production of sbottom ($\tilde{b}$) and stop ($\tilde{t}$) quarks could be highly enhanced at the Tevatron, giving the possibility of discovering new physics or limiting the parameter space available in the theory.

No signal is found over the predicted Standard Model background in both searches. Instead, 95% confidence level limits are set on the production cross section, and then translated into the mass plane of the hypothetical particles.

This thesis sketches the basic theory concepts of the Standard Model and the Minimal Supersymmetric Extension in Chapter 2. Chapter 3, describes the Tevatron and CDF. Based on the CDF subsystems information, Chapter 4 and 5 describe the analysis objet reconstruction and the heavy flavor tagging tools. The development of the analyses is shown in Chapter 6 and Chapter 7. Finally, Chapter 8 is devoted to discuss the results and conclusions of this work, and future prospects.

Chapter 2

Theory Introduction

The present chapter describes the theoretical framework that motivates this thesis. It contains a brief introduction to the SM, and one of its most famous extensions, the Minimal Supersymmetric extension of the Standard Model (MSSM). The description of the particular signatures searched for as part of this thesis is also included.

2.1 Standard Model

The Standard Model is a quantum field theory that has proven to describe to an unprecedented level of precision many experimental results [2]. A complete description of the theory can be easily found in the scientific literature [3, 4].

Based on several group symmetries, the SM includes the electromagnetic, weak and strong interaction. The building blocks of Nature, according to the SM, are a close set of fermions and bosons. The fermions are responsible for matter, while the bosons mediate interactions.

The fermionic sector ensembles six quarks and six leptons and their antiparticles, divided in three parallel families, presented in figure 2.1. The members of these families are identical in every observable, except for the mass. Our most immediate world is made with the particles of the first family: the up quark (u) and down quark (d) that form the protons and neutrons in nuclei and the electrons (e^-) and its associated neutrino (ν_e), as listed in Table 2.1. The particles in the other two families are more massive and decay rapidly to the ones of the first family.

The interactions of the fermions in Table 2.1 are mediated by the bosonic constituents of the SM. These bosons carry the fundamental forces derived from the symmetries, as summarized

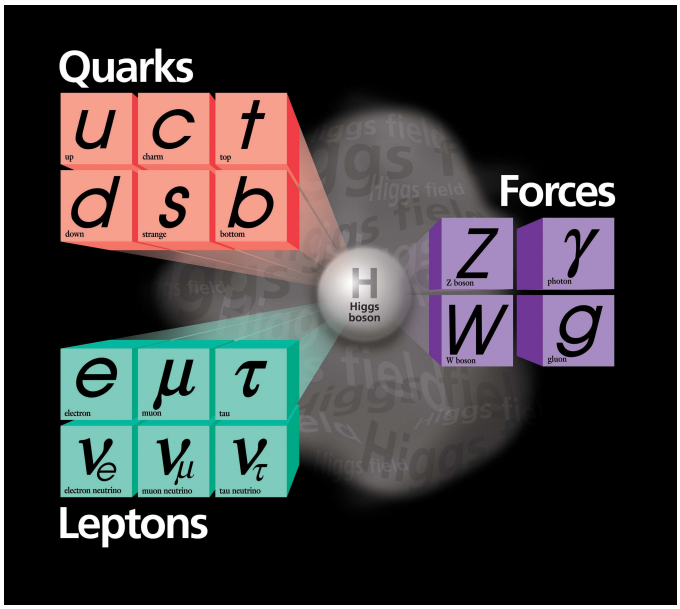

Figure 2.1: Elementary particles in the Standard Model.(Image courtesy of Fermilab Visual Media Services)

	1^{st} Generation	2^{nd} Generation	3^{rd} Generation
quarks	Up (u) 1.5-3.0 MeV/c^2	Charm (c) 1.25±0.09 GeV/c^2	Top (t) 173.1±1.3 GeV/c^2
	Down (d) 3.0-7.0 MeV/c^2	Strange (s) 95±25 MeV/c^2	Bottom (b) 4.20±0.07 GeV/c^2
leptons	Electron neutrino (ν_e) < 2 eV/c^2	Muon neutrino (ν_μ) < 0.19 MeV/c^2	Tau neutrino (ν_τ) < 18.2 MeV/c^2
	Electron (e) 0.511 MeV/c^2	Muon (μ) 105.66 MeV/c^2	Tau (τ) $1776.99^{+0.29}_{-0.26}$ MeV/c^2

Table 2.1: The fermion sector of the SM. All masses are taken from the Particle Data Group (PDG) [5], except for the top quark mass, where the last Tevatron combination is quoted in [6].

in Table 2.2. The overall symmetry of the SM is the combination of the color symmetry group for the strong force $SU(3)_C$, weak-isospin symmetry for the weak interaction of left handed particles $SU(2)_L$ and hypercharge symmetry $U(1)_Y$, expressed as $SU(3)_C \otimes SU(2)_L \otimes U(1)_Y$. However, the original symmetry is broken in our universe, as it will be detailed latter.

Even if gravity is the interaction that has been known for the longest time and is the closest to our every day life experience, it still has not been successfully included in the SM framework. This is one of the main arguments against the SM being the theory of everything, therefore suggesting that there needs to be a somewhat more general theory. This new theory would have to include all the symmetries of the SM, and, simultaneously accept that forth interaction.

In the following sections, an introduction to the different parts of the SM is presented. After a brief explanation of the symmetry originating each interaction, a short discussion of the couplings and eigenstates will be shown.

Interaction	Particle	Mass
electromagnetic	photon, γ	0
strong	gluon, g	0
weak	$W^{\pm}$	80.403±0.029 GeV/c^2
	Z^0	91.188±0.002 GeV/c^2

Table 2.2: The gauge bosons of the SM and their associated interactions [6].

2.1.1 Quantum Electrodynamics

Quantum Electrodynamics (QED) was developed in the late 1940s and early 1950s chiefly by Feynman, Schwinger and Tomonaga [7], describing electromagnetic interactions of electrons and photons. This is a quantum relativistic renormalizable theory which is invariant under a change of phase or gauge, θ:

$$\psi \rightarrow \psi' = e^{iQ\theta}\psi \ , \tag{2.1}$$

where Q represents the charge and ψ is the Dirac field (spin 1/2). In order to promote the global symmetry under U(1) transformations, responsible for the conservation of the charge, to a local one ($\theta = \theta(x)$), the covariant derivative needs to be introduced:

$$D_\mu \equiv \partial_\mu - ieQA_\mu \ , \tag{2.2}$$

where A_μ is a field that satisfies:

$$A_\mu \rightarrow A'_\mu \equiv A_\mu + \frac{1}{e}\partial_\mu \theta \ . \tag{2.3}$$

Therefore, the Lagrangian describing the theory becomes:

$$\mathcal{L} = \bar{\psi}(i\gamma^\mu D_\mu - m)\psi = \bar{\psi}(i\gamma^\mu \partial_\mu - m)\psi + \mathcal{L}_I \tag{2.4}$$

where the last term corresponds to the interaction with the new field, A_μ:

$$\mathcal{L}_I = eQA_\mu(\bar{\psi}\gamma^\mu\psi) \tag{2.5}$$

In addition, the kinetic energy of the new field needs to be introduced. From Maxwell's equations, the kinetic term must be of the form:

$$\mathcal{L}_K = -\frac{1}{4}F_{\mu\nu}F^{\mu\nu} \tag{2.6}$$

where $F_{\mu\nu} \equiv \partial_\mu A_\nu - \partial_\nu A_\mu$.

Thus, in this theory the electromagnetic interaction is described by two quantum fields: one for the charged particles and one for the photon. The strength of the interaction is usually described by the coupling constant α_{em} whose value depends on the momentum transfer q^2 in an interaction. At $q^2 \rightarrow 0$ (or low energies) the coupling constant value is that of the fine structure constant, $\alpha_{em} = \frac{e^2}{4\pi/hc} = \frac{1}{137}$. At larger scales (short distances) its value increases, being $\alpha_{em}(m_Z) \approx \frac{1}{128}$ at the scale given by the mass of the Z boson.

2.1.2 Quantum Chromodynamics

One of the cornerstones of the Standard Model is Quantum Chromodynamics (QCD) that describes the strong interaction. Following the way opened by QED and Yang-Mills theories, QCD was developed in 1973 [8] in the context of Quantum Field Theory based in SU(3) symmetry group [9]. It is a non-abelian theory and the Lagrangian, that describes the strong interaction of colored quarks and gluons[1], is given by:

$$\mathcal{L}_{QCD} = \sum_{flavor} \bar{q_a}(i\gamma^\mu D_\mu - m_q)_{ab} q_b - \frac{1}{4}F^A_{\alpha\beta}F_A^{\alpha\beta}, \tag{2.7}$$

[1]The charge associated with the strong interaction is the color charge. The color property was introduced for quarks to satisfy the requirement of Pauli exclusion principle [3]. Posterior experiment results proved the validity of color hypothesis

where the sum runs over the six different flavors of the quarks. $F^A_{\alpha\beta}$ is the field strength tensor derived from the gluon field A^A_α as,

$$F^A_{\alpha\beta} = [\partial_\alpha A^A_\beta - \partial_\beta A^A_\alpha - g f^{ABC} A^B_\alpha A^C_\beta], \tag{2.8}$$

and the indices A,B,C run over the eight color degrees of freedom of gluon field, g is the coupling constant, which determines the strength of the interaction between colored quanta, and f^{ABC} are the structure constants of the SU(3) color group. The third term in equation 2.8 shows the non-abelian nature of QCD. This term describes the property of interaction between gluons, resulting in the very different behavior of the strong interaction compared to the electromagnetic interaction. This self-coupling is the reason for the strong coupling constant, $\alpha_s = \frac{g^2}{4\pi}$, is large at small energies (large distances) and decreases at high energies (small distance) as is shown in figure 2.2.

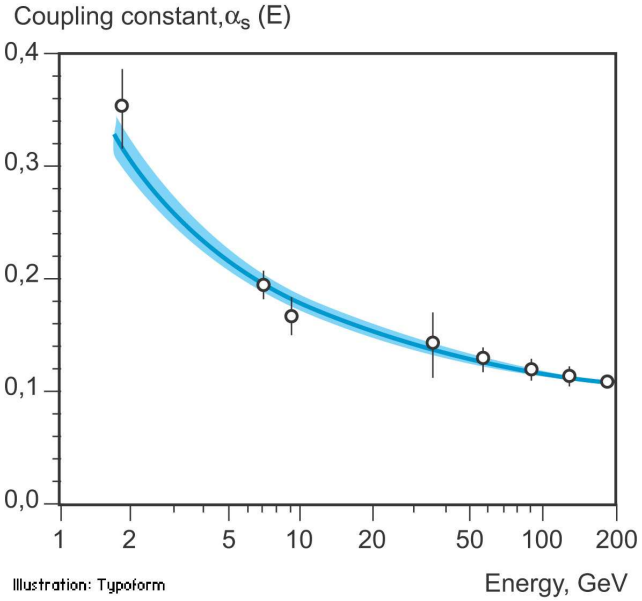

Figure 2.2: The value of the running coupling constant, α_S, as a function of the energy scale E.

This characteristic running of α_S is used to explain the observed behavior of the strong interaction:

- Asymptotic freedom: At high energies (small distance) the strong interaction proceeds via color field of reduced strength and the quarks and gluons behave as essentially free, non-interacting particles.

- Confinement: At low energies (or large distance) the strength of the color field is increasing, since the potential behaves as $V(r) \sim \lambda r$, and in this way the quarks and gluons can

never be observed as free particles. If two interacting partons are separated, the energy of the field increases so much that it creates new interacting particles and at the end it is left with colorless hadrons containing the partons. Therefore partons are not observed as free particles.

It is important to note that the asymptotic freedom property allows the application of perturbation theory to calculate cross section measurements in scattering processes where quarks and gluons are involved. Moreover, this property explains the partial success of the naïve Quark Parton Model approach, which is going to be presented below.

2.1.3 Parton Distribution Functions

The partonic structure of hadrons plays a fundamental rôle in elementary particle physics. The comparison of data with SM predictions, precision measurements of SM parameters, and searches for signals of physics beyond the SM, all rely on the parton picture of hadronic beam particles.

Perturbative QCD is not able to predict the x-dependence of the PDFs. PDFs at a given scale Q_0^2 are extracted from fits to data and DGLAP equations are used to predict PDFs to a higher scale Q^2. The PDFs are parametrized and the parameters are determined by a χ^2 minimization over data from different type of measurements: structure functions in deep-inelastic e, μ or ν scattering, measurements of Drell-Yan production, W-asymmetry in $p\bar{p}$ collisions and inclusive jet cross sections. Different groups provide parameterizations of parton densities. Among others, PDFs come from Martin, Roberts, Stirling and Thorne (MRST) group [10] and the "Coordinated Theoretical-Experimental Project on QCD"(CTEQ Collaboration) [11].

A Hessian method is used to evaluate the PDFs uncertainties. A brief description of the method is given below, for more details see [12, 13].

In the Hessian method, a large matrix (20×20 for CTEQ, 15×15 for MRST), with dimensions equal to the number of free parameters in the fit, has to be diagonalized. The result is 20 (15) orthogonal eigenvectors for CTEQ (MRST), denoted as a_i, which provides the basis for the determination of the PDFs uncertainties for any cross section. The Hessian matrix can be expressed as:

$$H_{ij} = \frac{1}{2}\frac{\partial^2 \hat{\chi}^2}{\partial a_i \partial a_j}. \tag{2.9}$$

This matrix determines the behavior of $\hat{\chi}^2(a)$ in the neighborhood of the minimum. The

point a_0 in the n-dimensional parameter space, where $\hat{\chi}^2(a)$ is minimum, is the best fit to the global data set. Points in some small neighborhood of a_0 are also acceptable fits. For each eigenvector two displacements from a_0, in the + and - directions along the vector, denoted a_i^+ and a_i^- for the i^{th} eigenvector are considered. At these points, $\hat{\chi}^2 = \hat{\chi}_0^2 + T^2$ where $\hat{\chi}_0^2 = \hat{\chi}^2(a_0)$ is the minimum, and T is a parameter called tolerance. Any PDFs set with $\hat{\chi}^2 - \hat{\chi}_0^2 < T^2$ is considered to be an acceptable fit to the global data set. In particular, the $2n$ PDFs sets $a_i^{\pm}$ span the parameter space in the neighborhood of the minimum. CTEQ group chooses T^2 ∼100 and MRST group uses T^2 ∼50.

Any quantity Γ that depends on PDFs has a predicted value $\Gamma_0 = \Gamma(a_0)$ and an associated, a priori asymmetric, uncertainty $\delta\Gamma$. The + (-) uncertainties are calculated as:

$$\delta\Gamma_+ = \left(\sum_{k=1}^{n} [max(\Gamma(a_i^+), \Gamma(a_i^-), \Gamma(a_0)) - \Gamma(a_0)]^2 \right)^{1/2} \tag{2.10}$$

and

$$\delta\Gamma_- = \left(\sum_{k=1}^{n} [min(\Gamma(a_i^+), \Gamma(a_i^-), \Gamma(a_0)) - \Gamma(a_0)]^2 \right)^{1/2}. \tag{2.11}$$

In figure 2.3 the uncertainties on gluon and u-quark distributions are shown. The u-quark distribution is tightly constrained for x≤ 0.8, whereas the uncertainty on the gluon distribution can be larger than a factor of 2 at high x.

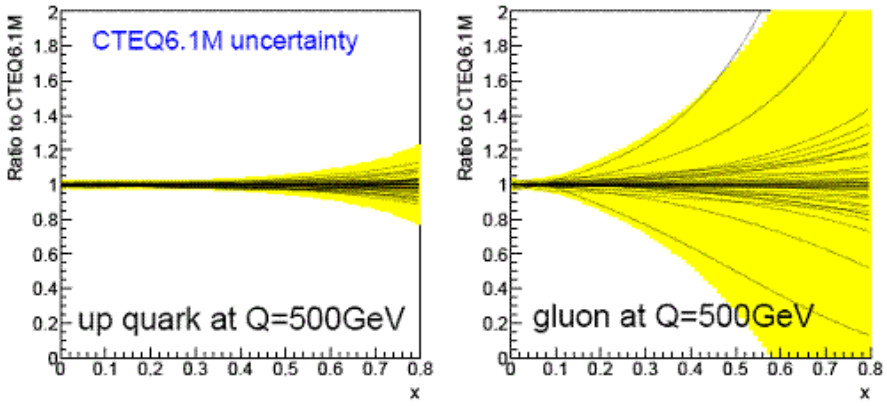

Figure 2.3: Uncertainty on gluon and u-quark PDFs. The yellow bands represent the global uncertainty. The curves are the ratios of the 40 eigenvector basis sets to the standard set, CTEQ6.1M.

2.1.4 Electroweak Theory

The weak theory was proposed by Enrico Fermi in 1934 in order to explain the proton β-decay [14]. In this theory four fermions directly interacted with one another in such a way that a neutron (or a down-quark) could be directly split into an electron, an antineutrino and a proton (an up-quark). The strength of the Fermi's interaction was given by the Fermi constant, G_F.

Feynman diagrams described the interaction remarkably well at tree level but loop diagrams could not be calculated reliably because Fermi's interaction was not renormalizable. The solution came in 1967 when the electromagnetic and weak interactions were successfully unified by Glashow, Salam and Weinberg [15, 16, 17]. This unification constituted the Standard Electroweak Model which is the core of the SM. The idea of the unification is to combine both interactions into one single theoretical framework in which they would appear as two manifestations of the same fundamental interaction. These interactions are unified under the group $\mathrm{SU(2)_L} \otimes \mathrm{U(1)_Y}$. The first part of the group has dimension three and therefore, three generators are needed: $t_i = \frac{\sigma_i}{2}(i = 1, 2, 3)$ where σ_i are the Pauli matrices. These generators, due to the global gauge invariance under SU(2), introduce a new quantum number called the *w*eak isospin (T). This number is associated to the different spin-like multiplets. Since weak force only interacts with left-handed particles (right-handed antiparticles), the left-handed fermions transform as doublets while the right handed ones transform as singlets:

$$f_L^i = \begin{pmatrix} \nu_L^i \\ l_L^i \end{pmatrix} \quad , \quad \begin{pmatrix} u_L^i \\ d_L^i \end{pmatrix} \tag{2.12}$$

$$f_R^i = l_R^i, u_R^i, d_R^i \tag{2.13}$$

where $i = 1, 2, 3$ corresponds to the family index. Hence, the weak interaction is divided into a "charged part" (that is, exchanging the components of the doublet) and a "neutral part" (that is, leaving the doublets as they are). Since SU(2) is a non-Abelian group, it allows self-interactions of these gauge fields.

Since the group $U(1)_Y$ has only one dimension, its structure is more simple having only one generator called the hypercharge $\hat{Y}$. Once the $\mathrm{SU(2)_L} \otimes \mathrm{U(1)_Y}$ group is defined, the SM electroweak Lagrangian is obtained by requiring invariance under local gauge transformations to obtain an interacting field theory, following the analogy with QED. This is achieved by replacing the derivatives of the fields by the corresponding covariant derivative, which now has the form:

$$D_\mu \equiv \partial_\mu - ig\vec{T}\vec{W}_\mu - ig'\frac{Y}{2}B_\mu \, , \tag{2.14}$$

where g and g' are the coupling constants corresponding to $SU(2)_L$ and $U(1)_Y$, respectively.

$$\mathcal{L}_{EW} = \mathcal{L}_f + \mathcal{L}_G + \mathcal{L}_{SSB} + \mathcal{L}_{YW} \ . \tag{2.15}$$

The first term corresponds to the fermion Lagrangian:

$$\mathcal{L}_f = \sum_{f=l,q} \bar{f} i \not{D} f \ . \tag{2.16}$$

The second term is the contribution from the gauge fields:

$$\mathcal{L}_G = -\frac{1}{4} W^i_{\mu\nu} W^{\mu\nu}_i - \frac{1}{4} B_{\mu\nu} B^{\mu\nu} + \mathcal{L}_{GF} + \mathcal{L}_{FP} \ , \tag{2.17}$$

where $W^i_{\mu\nu}$ (with $i = 1, 2, 3$) and $B_{\mu\nu}$ are, respectively, the field strength tensors for $SU(2)_L$ and $U(1)_Y$ defined as:

$$W^i_{\mu\nu} \equiv \partial_\mu W^i_\nu - \partial_\nu W^i_\mu + g\epsilon^{ijk} W^j_\mu W^k_\nu \tag{2.18}$$

$$B_{\mu\nu} \equiv \partial_\mu B_\nu - \partial_\nu B_\mu \tag{2.19}$$

and $\mathcal{L}_{GF}$ and $\mathcal{L}_{FP}$ are the gauge fixing and Faddeev-Popov Lagrangians that are needed in any YM theory [18].

The last two terms of the electroweak Lagrangian (equation 2.15) are the symmetry breaking sector and the Yukawa Lagrangian, respectively, which will be described in next subsection.

The gauge fields presented at equation 2.18 can be rewritten as:

$$\begin{aligned} W^\pm_\mu &= \frac{1}{\sqrt{2}}(W^1_\mu \mp i W^2_\mu) \\ Z_\mu &= \cos\theta_W W^3_\mu - \sin\theta_W B_\mu \\ A_\mu &= \sin\theta_W W^3_\mu + \cos\theta_W B_\mu \end{aligned} \tag{2.20}$$

where, A_μ represents the photon field and $\cos\theta_W = \frac{g}{\sqrt{g'^2+g^2}}$ is the weak mixing angle, which relates both couplings by the simple relation $\tan\theta_W = g'/g$. In addition, $W^\pm_\mu$ and Z_μ fields are associated to the physical $W^\pm$ and Z^0 boson particles. In this framework, the electron charge and the Fermi constant can be written in terms of the couplings through the following relations:

$$\begin{aligned} e &= g \sin\theta_W \\ G_F &= \frac{\sqrt{2}}{8} \frac{g^2}{m^2_W} \ . \end{aligned} \tag{2.21}$$

The electric charge $\hat{Q}$, the third component of the weak isospin $\hat{T}_3$, and the weak-hypercharge $\hat{Y}$ are linearly related by the Gell-Mann-Nishijima formula:

$$\hat{Q} = \hat{T}_3 + \hat{Y}/2 \, . \tag{2.22}$$

Hence, the global and local conservation of weak-isospin and hypercharge naturally implies charge conservation, as required by QED, and the electromagnetic and weak interactions are unified under the same theoretical framework.

2.1.5 The Higgs Mechanism

As shown, the Standard Model formalism allows the unification of electromagnetic and weak interactions through the exploitation of a local gauge symmetry. Nevertheless, this gauge symmetry requires massless $W^{\pm}$ and Z bosons. This requirement is in contradiction with the observation and one needs to introduce a mechanism for generating non-zero masses while preserving the renormalizability of the theory. In the SM, the Higgs mechanism of Spontaneous Symmetry Breaking (SSB) is proposed.

In this mechanisim a new field, the Higgs field, is introduced such as:

$$\Phi \equiv \begin{pmatrix} \phi^+ \\ \phi^0 \end{pmatrix} \, . \tag{2.23}$$

The correspondent kinetic and potential term in the Lagrangian has the form:

$$\mathcal{L}_{\Phi} = (D_{\mu}\Phi)^{\dagger} D^{\mu}\Phi - V(\Phi) \, , \tag{2.24}$$

where

$$V(\Phi) = \mu^2 \Phi^{\dagger}\Phi + \lambda(\Phi^{\dagger}\Phi)^2 \, . \tag{2.25}$$

If $\lambda > 0$ and $\mu^2 < 0$ the potential $V(\Phi)$ has a minimum for:

$$\Phi^{\dagger}\Phi = -\frac{\mu^2}{2\lambda} \equiv \frac{v^2}{2} \, . \tag{2.26}$$

Thus, the field Φ has a non-zero vacuum expectation value (VEV):

$$\langle 0|\Phi|0\rangle = \frac{v}{\sqrt{2}} \neq 0 \, . \tag{2.27}$$

Choosing one of a set of degenerate states of minimum energy breaks the gauge symmetry.

As stated by the Goldstone theorem, fields that acquire a VEV will have an associated massless Goldstone boson which will disappear transformed into the longitudinal component of a massive gauge boson. Since the photon is known to be massless, the symmetry is chosen to be broken so that only the fields with zero electric charge (the ones that cannot couple to the electromagnetic interaction) acquire a VEV. In such a way, the symmetry of the photon-associated operator, $\hat{Q}$ is preserved:

$$\Phi_0 \equiv \langle 0|\Phi|0\rangle \equiv \begin{pmatrix} 0 \\ v \end{pmatrix} Q\Phi_0 = 0 \, . \tag{2.28}$$

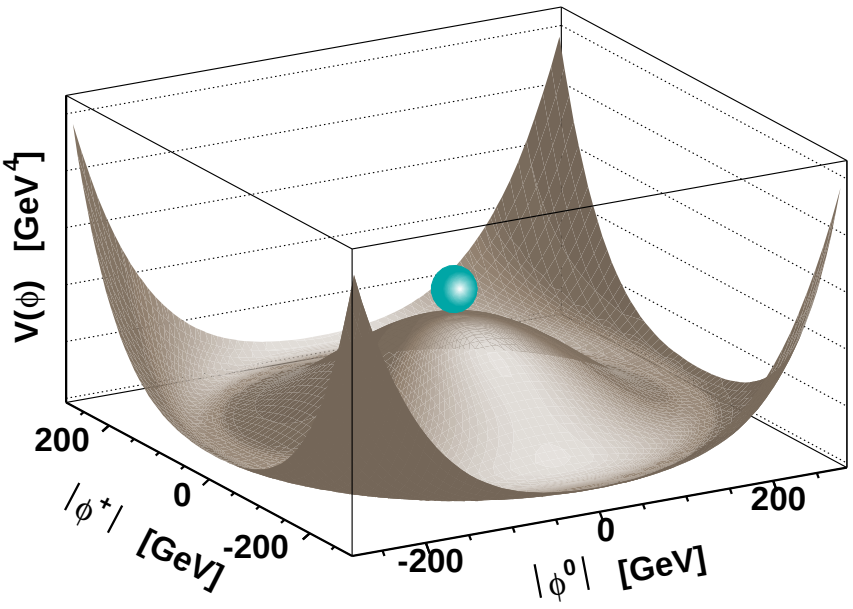

Figure 2.4: The minimum of the Higgs potential occurs at $-\mu^2/(2\lambda)$, not at zero

Expanding around the true minimum of the theory, the complex field ϕ becomes:

$$\Phi(x) = e^{i\frac{\vec{\tau}}{2}\vec{\xi}(x)} \frac{1}{\sqrt{2}} \begin{pmatrix} 0 \\ v + H(x) \end{pmatrix} \, . \tag{2.29}$$

where the three parameters $\vec{\xi}(x)$ correspond to the motion through the degenerated minima in the SU(2) space. Since the Lagrangian is locally gauge invariant, one can choose $\vec{\xi}(x) = 0$. Hence, introducing this expansion into the SM Lagrangian (equation 2.15), one obtains the tree level predictions for massive fermions (coming from the $\mathcal{L}_{YW}$ part), massive gauge bosons

(coming from the kinetic part of $\mathcal{L}_{SSB}$) and a new *Higgs boson*. These relations are:

$$M_W = \frac{vg}{2} \tag{2.30}$$

$$M_Z = v\frac{\sqrt{g^2+g'^2}}{2} \tag{2.31}$$

$$M_H = \sqrt{-2\mu^2} = \sqrt{2\lambda}v \tag{2.32}$$

$$m_f = \lambda_f \frac{v}{\sqrt{2}} \tag{2.33}$$

$$m_\gamma^2 = 0 \tag{2.34}$$

where f stands for the fermions in the theory. These relations can also be expressed as a function of the weak mixing angle,

$$M_z = \frac{\frac{1}{2}vg}{\cos\theta_W} \ , \tag{2.35}$$

which leads to the SM prediction

$$\frac{M_W^2}{M_Z^2} = cos^2\theta_W \ . \tag{2.36}$$

This prediction was tested once the $W^\pm$ and Z vector bosons were discovered in 1983 by UA1 and UA2 collaborations at the CERN SPS [19, 20].

The ten independent fields before SSB (three massless gauge bosons ($W^\pm$, Z), with two polarization states each, and one SU(2) doublet of complex scalars) are now represented by three massive bosons, which account for nine degrees of freedom, and a new physical scalar particle called the Higgs boson, which accounts for the last degree of freedom.

This new particle, which is the missing piece to confirm the Higgs mechanism, has the couplings completely defined by the other parameters of the model:

$$\lambda_{HHH} = 3\frac{M_H^2}{M_Z^2} \tag{2.37}$$

$$\lambda_{HVV} = 2\sqrt{2G_F}M_V^2 \tag{2.38}$$

$$\lambda_{Hff} = 2\sqrt{2G_F}m_f \tag{2.39}$$

where $V = W, Z$ and G_F is the Fermi constant. The vacuum expectation value v is determined experimentally from the partial width $\Gamma(\mu \to \nu_\mu \bar{\nu}_e e)$ at low energies ($q^2 << M_W^2$):

$$\frac{G_F}{\sqrt{2}} = \frac{g^2}{8M_W^2} = \frac{1}{2v^2} \ , \tag{2.40}$$

where, substituting experimental values:

$$v = (\sqrt{2}G_F)^{-\frac{1}{2}} = 246 \text{ GeV} \ , \tag{2.41}$$

which sets the electroweak symmetry breaking scale.

This new particle allows Yukawa-like terms in the Lagrangian:

$$g_f[(\bar{f}_L\phi)f_R + \text{h.c.}] \,, \tag{2.42}$$

which can be written in terms of the VEV:

$$\sqrt{\frac{1}{2}}g_f v(\bar{f}_L f_R + \bar{f}_R f_L) \,. \tag{2.43}$$

Therefore, not only the bosons acquire mass through the Higgs mechanism but also the fermions with $m_f = g_f v/\sqrt{2}$. Noticeably, the strength of the coupling is proportional to the masses. However, the masses are not predicted by the model, but the relation of the couplings to the fermions contain all the predictive power of the model for proving masses of the fermions.

2.1.6 Standard Model Limitations

The SM description of the different processes involving electroweak or strong interactions is extremely accurate. At the present time, no experiment has been able to find any clear deviation from the SM predictions. Nevertheless, physicists are still pushing to find such deviations. The main reason is that the SM present serious theoretically motivated problems, starting from the fact that gravity is not accommodated in the theory, what prevent it from being the ultimate theory, the Theory of Everything (TOE), that would describe Nature in a comprehensive manner.

Even accepting the peculiar set of group representations and hypercharges required by the model, the SM contains at least 19 free parameters, such as couplings, masses and mixings, which are not predicted but must be measured by the experiment. In addition, more parameters would be needed if one wants to accommodate non-accelerator observations such as the cosmological baryon asymmetry, neutrino masses and mixings or the problematic cosmological constant.

The SM leaves also several questions unanswered such as why are there three generations, spatial dimensions or colors, how do we understand neutrino oscillations and massive neutrinos, why are the electric charge of the proton and the electron exactly opposite or whether the Higgs mechanism is really the process through which the electroweak symmetry breaking occurs and lay beneath the origin of masses. In addition, the model cannot explain which are the mechanisms to produce the matter-antimatter asymmetry observed in the universe or what is the relation between the strong and electroweak forces.

Perhaps the most surprising feature of the SM is the accurate description of the interactions between particles with masses 17 orders of magnitude smaller than the Planck mass and the difficulty to accommodate gravity within this framework [21]. This feature may be an indication that the SM is an effective theory, that is a "low energy" limit of a more fundamental one. But this assumption automatically leads to the question of up to which energy scale will the SM be valid.

However, spin zero fields are radically different from fermions and gauge bosons. The latter are protected from large radiative corrections to their masses due to chiral and gauge symmetries, respectively. In the SM there is no mechanism to prevent scalar particles from acquiring large masses through radiative corrections. Therefore, m_H^2 receives enormous quantum corrections from the virtual effects of every particle which couples to the Higgs field.

Due to these corrections, the Higgs mass would be

$$m_{h_{SM}}^2 = (m_h^2)_0 + \Delta M_H^2 \tag{2.44}$$

where $(m_h^2)_0$ is the bare Higgs mass and ΔM_H^2 is the correction given by

$$\Delta M_H^2 = -\frac{\lambda_f^2}{16\pi^2}\left[2\Lambda^2 + \mathcal{O}\left(m_f^2 \ln\left(\frac{\Lambda}{m_f}\right)\right)\right] i \tag{2.45}$$

where λ_f is the Yukawa coupling of the fermion f and Λ is an energy cutoff which is interpreted as the energy scale at which new physics enters and changes the high-energy behavior of the theory. If the SM needs to describe nature until the Planck scale, then the quantum correction ΔM_H^2 is about 30 orders of magnitude larger than the bare Higgs mass square. A cancellation of these corrections at all orders would call for an incredible "fine tunning" which seems very unlikely [22]. This problem is present even if there is no direct coupling between the Standard model Higgs boson and the unknown heavy particles [23].

In a model with spontaneous electroweak symmetry breaking, the problem affects not only to the Higgs mass but also its expectation value and the masses of other particles that get their masses through this mechanism such as the W, Z, quarks and charged leptons. This situation has also an analogy with the self-energy corrections on the electron, which is solved by the presence of the positron [24]. Hence, it is unnatural to have all the SM particles masses at the electroweak scale unless the model is somehow cut off and embedded in a richer structure at energies no bigger than the TeV scale.

2.2 Minimal Supersymmetric Extension of the Standard Model

After a brief introduction to supersymmetry, this section presents the Minimal Supersymmetric Extension of the SM (MSSM).

2.2.1 Supersymmetry

Supersymmetry (SUSY) [23] is a symmetry which relates masses and couplings of bosons and fermions via spin-$\frac{1}{2}$ operators. In SUSY, particles are combined into superfields and an operator Q generates the transformation of converting fermions to bosons and vice versa:

$$Q|Boson\rangle = |Fermion\rangle \qquad Q^{\dagger}|Fermion\rangle = |Boson\rangle \tag{2.46}$$

Therefore Q is a complex anticommuting spinor and its hermitian conjugate, $Q^{\dagger}$, is also a symmetry generator. Both generators are fermionic in nature ($S = 1/2$) and form a Lie algebra [25], together with the four-momentum and the Lorentz transformation generators. In fact, SUSY is a generalization of the space-time symmetries of quantum field theory and seems to be the last possible extension of the Lorentz group [26].

In this situation, each chiral fermion $f_{L,R}$ has a scalar partner $\tilde{f}_{L,R}$ and for each massless gauge boson A_{μ}, with the helicity states ± 1, there is a massless spin $1/2$ gaugino partner, with helicity states $\pm\frac{1}{2}$.

2.2.2 Supersymmetry and the Hierarchy Problem

The SM hierarchy problem presented in section 2.1.6 is very elegantly solved when considering the supersymmetric theory [27]. The reason is that every fermion f has a scalar SUSY partner S that couples to the Higgs as well and contributes with a mass correction term of the form:

$$\Delta M_H^2 = \frac{\lambda_S^2}{16\pi^2}\left[2\Lambda^2 + \mathcal{O}\left(m_S^2 \ln\left(\frac{\Lambda}{m_S}\right)\right)\right] \tag{2.47}$$

Since now $\lambda_f = \lambda_S$ and Fermi statistics imply an opposite sign with respect to the contribution stated in equation 2.47, all the terms have a counter-term that naturally cancel all the huge corrections. The terms that do not cancel are of the form:

$$\Delta M_H^2 = \frac{\lambda^2}{16\pi^2}\left|m_S^2 - m_f^2\right| \tag{2.48}$$

where some smaller contributions have been omitted. This result leads us to the following "naturalness" argument [28, 29]: since these corrections must not be greater than $m_{h_{SM}}$ in order to avoid too much fine tuning, then

$$\left|m_S^2 - m_f^2\right| \lesssim 1\mathrm{TeV}^2 \,. \tag{2.49}$$

Hence, one associates $\Lambda \sim 1$ TeV as the scale where the SM is no longer valid and must be substituted by its supersymmetric extension. As a benefit, this new theory would be valid all the way up to the Planck scale. In any case, this is only a qualitative argument and does not help predicting exactly whether new particles should appear at 900 GeV or 2 TeV.

2.2.3 Other Benefits from the Introduction of SUSY

Besides making a small Higgs mass natural, SUSY has other interesting consequences. One of them is, when SUSY is locally realized, that it contains among its gauge fields a possible candidate to be the graviton. Thus SUSY seems to be a good candidate for a theory of all interactions, or at least to play an important rôle in any such theory. In addition, Great Unifications Theories (GUT) also provide good motivation for the existence of supersymmetry. One can use the running of the three couplings of the SM, measured at the electroweak scale, and find that, at a certain GUT scale of 10^{15} GeV, the couplings *almost* become the same value [30]. But if one considers SUSY then the couplings are modified in such a way that they become precisely the same value at the GUT scale. Therefore, it is a strong indication for the need of SUSY. However, some people claim that there is nothing special on that [31] provided that other models could do it if they introduce as many parameters as SUSY does.

In addition to gauge coupling unification, SUSY is also a key ingredient for GUT. These theories have interesting predictions such as a small neutrino mass of the order of $m_\nu \approx m_W^2/m_{GUT} \approx 10^{-2}\ \mathrm{eV/c^2}$ and it can lead to the understanding of the different quark and lepton quantum numbers. But without SUSY the lifetime of the proton would be too small and the prediction for $\sin^2\theta_W$ would differ from the experiment [32, 31, 33]. In addition, SUSY has been of greatest interest in string theories since it is the mechanism which provides a coherent and complete framework which avoids negative square masses in some vibrational modes (tachyons) [34].

Furthermore, some SUSY models predict the presence of a lightest supersymmetric particle, which is a candidate for dark matter in the universe, provided that it is neutral, weakly interacting and absolutely stable.

As a final remark, recent fits on the electroweak precision observables, such as the effective leptonic weak mixing angle, $\sin^2\theta_{eff}$, seem to favor supersymmetric models in front of the SM alone [35]. This can be seen in figure 2.5, where the SM predictions for the M_W as a function of m_t is being compared with the predictions from the unconstrained Minimal Supersymmetric Standard Model (MSSM), which will be described in the next subsection. The predictions within the two models give rise to two bands with only a relatively small overlap region. The allowed parameter region in the SM arises from varying the only free parameter of the model, the mass of the SM Higgs boson from $M_{h_{SM}} = \ \mathrm{GeV}/c^2\,114$ (upper edge of the band) to $\mathrm{GeV}/c^2\,400$ (lower edge of the band). For the MSSM area, SUSY masses close to their experimental limit are assumed for the upper edge, while the MSSM with large masses yields the lower edge of the blue area (dark-shaded). The 68% C.L. experimental results slightly favours the MSSM over the SM[2].

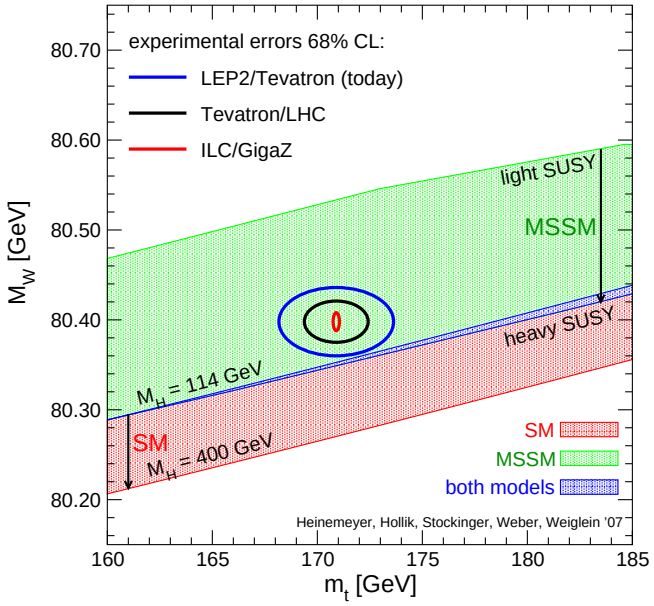

Figure 2.5: M_W as a function of m_t as predicted by the SM in red (medium-shaded) and blue (dark-shaded) bands and with the MSSM prediction in green (light-shaded) and blue (dark-shaded) bands. The perspectives for the present and future generation colliders, are also shown.

[2]Last top mass measurements from the Tevatron [6] indicate even a lower mass for the top: $m_t = 173.1 \pm 0.6(stat) \pm 1.1(syst)\ \mathrm{GeV}/c^2$.

2.2.4 The Minimal Supersymmetric Standard Model

Similarly to the SM construction, that was conceived to be the minimal group viable to explain the electroweak sector, the MSSM [36] is the minimal viable supersymmetric extension of the SM. The MSSM obeys the same $\mathrm{SU}(3)_C \otimes \mathrm{SU}(2)_L \otimes \mathrm{U}(1)_\mathrm{Y}$ gauge symmetries of the Standard Model but doubles the spectrum of new particles since for every particle in the SM, a superpartner is postulated which differs by half a unit of spin. The superpartners are conveniently described by a notation with close correspondence to the SM notation for bosons and fermions. Hence, the superpartners are written with the same letter of their partner but with a tilde over it and the superfields are written with a "tilde" superscript. In addition, the bosonic partners of the fermions are denoted starting with an extra "s" (e.g. selectron is the superpartner of the electron) and the fermionic partners of the bosons finish with the suffix "ino" (e.g. gluino is the superpartner of the gluon).

For simplicity and to avoid unnecessary repetitions, consider the case of one generation of quarks, leptons and their superpartners. One can define $\hat{Q}$ as the superfield containing an $\mathrm{SU}(2)_L$ doublet of quarks:

$$Q = \begin{pmatrix} u_L \\ d_L \end{pmatrix} \tag{2.50}$$

and their scalar partners which are also in an $\mathrm{SU}(2)_L$ doublet,

$$\tilde{Q} = \begin{pmatrix} \tilde{u}_L \\ \tilde{d}_L \end{pmatrix} \tag{2.51}$$

In an analogous form, the superfield $\hat{U}^c$ ($\hat{D}^c$) contains the right-handed up (down) anti-quark, $\bar{u}_R$ ($\bar{d}_R$), and its scalar partner, $\tilde{u}^*_R$ ($\tilde{d}^*_R$). Following the same pattern, leptons are contained in the $SU(2)_L$ doublet superfield $\hat{L}$ which contains the left-handed fermions,

$$L = \begin{pmatrix} \nu_L \\ e_L \end{pmatrix} \tag{2.52}$$

and their scalar partners,

$$\tilde{L} = \begin{pmatrix} \tilde{\nu}_L \\ \tilde{e}_L \end{pmatrix} \quad . \tag{2.53}$$

Finally, the superfield $\hat{E}^c$ contains the right-handed anti-electron, $\bar{e}_R$, and its scalar partner, $\tilde{e}^*_R$.

Similarly, for every gauge boson it exist a Majorana fermion (gaugino). $\hat{G}^a$ is defined as a superfield that contains all the gluons, g^a, and their fermion partners the gluinos, $\tilde{g}^a$; $\hat{W}_i$ contains the $SU(2)_L$ gauge bosons, W_i, and their fermion partners, $\tilde{\omega}_i$ (winos); and $\tilde{B}$ contains the $U(1)$ gauge field, B, and its fermion partner, $\tilde{b}$ (bino).

In addition, in the MSSM the Higgs sector is enlarged to avoid triangle gauge anomalies [37, 38, 39]. Anomalies are not allowed in gauge theories and this is simply achieved by requiring that the sum of all fermion charges vanishes. The Higgs scalar doublet acquires a SUSY partner which is an $\mathrm{SU}(2)_L$ doublet of Majorana fermion fields, $\tilde{h}_1$ (Higgsinos), which will contribute to the triangle $\mathrm{SU}(2)_L$ and $\mathrm{U}(1)_Y$ gauge anomalies. Since fermions in SM have exactly the right quantum numbers to cancel these anomalies, it follows that the contribution from the fermionic partner of the Higgs doublet remains uncanceled. The easiest solution is to require a second Higgs doublet with precisely the opposite $\mathrm{U}(1)_Y$ quantum number than the first Higgs doublet. Furthermore, in the SM the Higgs doublet (the complex conjugate of the doublet) can couple to the $T_3 = +\frac{1}{2}$ ($T_3 = -\frac{1}{2}$) fermions and give mass to all the spectrum of fermions. But, in a supersymmetric theory, any doublet can give mass either to a $T_3 = +\frac{1}{2}$ or a $T_3 = -\frac{1}{2}$ fermion but not both. Thus, two Higgs doublets are needed in order to generate both up-like and down-like quark masses. As result, one could think of the SM becoming a two Higgs doublet model (2HDM) [40] prior to introduce the supersymmetric sector. In Table 2.3 the spectrum of the MSSM fields is summarized.

With two SU(2) doublets, the theory has eight real scalar fields and three massless gauge bosons, which accounts for fourteen degrees of freedom. After SUSY breaking, the three gauge bosons acquire masses (nine degrees of freedom), which means that there should exist five spin-zero Higgs fields in the spectrum: three neutral scalars (h, H, A) and two charged pairs (H^+, H^-).

The parameters of the supersymmetry-conserving sector consist of:

- Gauge couplings: g_s, g and g', corresponding to the Standard Model gauge group $\mathrm{SU}(3)_C \otimes \mathrm{SU}(2)_L \otimes \mathrm{U}(1)_\mathrm{Y}$, respectively.
- Higgs mass parameter, μ.
- Higgs-fermion Yukawa coupling constants: λ_u, λ_d, and λ_e, corresponding to the coupling of quarks or leptons and their superpartners to the Higgs bosons and higgsinos.

The supersymmetry-breaking sector contains the following set of parameters:

Names		**2HDM particle**		**SUSY partner**		$\begin{pmatrix} SU(3)_C \\ SU(2)_L \\ U(1)_Y \end{pmatrix}$
squarks, quarks ($\times$ 3 families)	$\hat{Q}$	$(u_L\ d_L)$	$\frac{1}{2}$	$(\tilde{u}_L\ \tilde{d}_L)$	0	$(3, 2, \frac{1}{3})$
	$\hat{U}$	$u_R^\dagger$	$\frac{1}{2}$	$\tilde{u}_R^*$	0	$(\bar{3}, 1, -\frac{4}{3})$
	$\hat{D}$	$d_R^\dagger$	$\frac{1}{2}$	$\tilde{d}_R^*$	0	$(\bar{3}, 1, \frac{2}{3})$
sleptons, leptons ($\times$ 3 families)	$\hat{L}$	$(\nu\ e_L)$	$\frac{1}{2}$	$(\tilde{\nu}\ \tilde{e}_L)$	0	$(1, 2, -1)$
	$\hat{E}$	$e_R^\dagger$	$\frac{1}{2}$	$\tilde{e}_R^*$	0	$(1, 1, 2)$
EWK bosons	$\hat{W}$	$W^1\ W^2\ W^3$	1	$\tilde{W}^1\ \tilde{W}^2\ \tilde{W}^3$	$\frac{1}{2}$	(1, 3, 0)
	$\hat{B}$	B	1	$\tilde{B}$	$\frac{1}{2}$	(1, 1, 0)
Strong bosons	$\hat{G}_a$	g_a	1	$\tilde{g}_a$	$\frac{1}{2}$	(8, 1, 0)
Higgs, higgsinos	$\hat{H}_u$	$(H_u^+\ H_u^0)$	0	$(\tilde{H}_u^+\ \tilde{H}_u^0)$	$\frac{1}{2}$	$(1, 2, 1)$
	$\hat{H}_d$	$(H_d^0\ H_d^-)$	0	$(\tilde{H}_d^0\ \tilde{H}_d^-)$	$\frac{1}{2}$	$(1, 2, -1)$

Table 2.3: Superfields and particle content of the MSSM. Symbols for each of the chiral supermultiplets as a whole are indicated in the second column.

- Gaugino Majorana masses M_3, M_2 and M_1, associated with the $\mathrm{SU}(3)_C$, $\mathrm{SU}(2)_L$ and $\mathrm{U}(1)_\mathrm{Y}$ subgroups, respectively. These masses may be connected in some cases as will be seen later.

- Five scalar squared-mass parameters for the squarks and sleptons: $M_{\tilde{Q}}^2$, $M_{\tilde{U}}^2$, $M_{\tilde{D}}^2$, $M_{\tilde{L}}^2$ and $M_{\tilde{E}}^2$, corresponding to the five electroweak gauge multiplets.

- Three scalar Higgs squared-mass parameters, two of which (m_1^2 and m_2^2) contribute to the diagonal Higgs squared-masses and a third which corresponds to the off-diagonal terms $m_{12}^2 \equiv \mu B$. These three parameters can be re-expressed in terms of the two Higgs vacuum expectation values ($v_d = \langle H_d^0 \rangle$ and $v_u = \langle H_u^0 \rangle$)[3], usually taken through the ratio

$$\tan\beta \equiv \frac{v_u}{v_d}\ , \tag{2.54}$$

  and one physical Higgs mass[4].

[3]Notation v_u (v_d) is used to distinguish vacuum expectation values of the Higgs field which couples exclusively to up-type (down-type) quarks.

[4]Note that $v_d^2 + v_u^2 = 4M_W^2/g^2 = (246\ \ \mathrm{GeV}/c^2\ )^2$ is fixed by the W mass and the gauge coupling, but $\tan\beta$ is a free parameter of the model.

- Trilinear interaction terms of the form Higgs-squark-squark and Higgs-slepton-slepton, with coefficients A_u, A_d and A_e.

The gluino is the color octet Majorana (there is no distinct antigluon) fermion partner of the gluon. It has 16 degrees of freedom since there are 8 massless gluons (2 spin degrees of freedom, each). The supersymmetric partners of the electroweak gauge and Higgs bosons (gauginos and higgsinos) can mix. As a result, the physical mass eigenstates are model-dependent linear combinations of these states, called *charginos* and *neutralinos*, which are obtained by diagonalizing the corresponding mass matrices. There are two charginos ($\tilde{\chi}_i^{\pm}$) and four neutralinos ($\tilde{\chi}_i^0$), which are by convention ordered in masses ($\tilde{\chi}_1^{\pm}$ is the lowest chargino and $\tilde{\chi}_1^0$ is the lowest neutralino). Depending whether the chargino or neutralino eigenstate approximates a particular gaugino or higgsino state, they can become more photino-like, bino-like... and result in strikingly different phenomenology.

The supersymmetric partners of the quarks and leptons are spin-zero bosons and the resulting squarks and sleptons can also mix their left- and right-handed components yielding the mass eigenstates (denoted by the indices 1,2 instead of L, R). This mixing is proportional to the mass of the SM partner quark or lepton and to $\tan\beta$. Thus, the mixing can lead to an important splitting in the mass spectrum of heavy squarks, specially at large $\tan\beta$. In contrast, the first two families can be considered degenerate in mass. All physical particles of the MSSM are given in Table 2.4.

2HDM particle		**spin**	**SUSY particle**		**spin**
quarks:	q	$\frac{1}{2}$	squarks:	$\tilde{q}_1,\ \tilde{q}_2$	0
leptons:	l	$\frac{1}{2}$	sleptons:	$\tilde{l}_1,\ \tilde{l}_2$	0
gluons:	g_a	1	gluinos:	$\tilde{g}_a$	$\frac{1}{2}$
gauge bosons:	$W^{\pm}$, Z^0, γ	1	neutralinos:	$\tilde{\chi}_1^0,\ \tilde{\chi}_2^0,\ \tilde{\chi}_3^0,\ \tilde{\chi}_4^0$	$\frac{1}{2}$
Higgs bosons:	$h^0,\ H^0,\ A^0,\ H^{\pm}$	0	charginos:	$\tilde{\chi}_1^{\pm},\ \tilde{\chi}_2^{\pm}$	$\frac{1}{2}$

Table 2.4: The particle content of the MSSM.

2.2.5 MSSM Lagrangian and R-parity

The MSSM Lagrangian is constructed using the already defined particle content and following an analogy with the $\mathcal{L}_{\rm SM}$. Following a similar notation as in the SM, the kinetic term of the

Lagrangian can be written as:

$$\begin{aligned}\mathcal{L}_{KE} = & \sum_i \left\{ (D_\mu S_i)^\dagger (D^\mu S_i) + \frac{i}{2}\bar{\psi}_i \gamma^\mu D_\mu \psi_i \right\} \\ + & \sum_A \left\{ -\frac{1}{4} F^A_{\mu\nu} F^{\mu\nu A} + \frac{i}{2}\bar{\lambda}_A D \lambda_A \right\} .\end{aligned} \tag{2.55}$$

Here, S_i (ψ_i) is the scalar (fermion) component of the i^{th} chiral superfield, D is the $SU(3) \otimes SU(2)_L \otimes U(1)$ gauge invariant derivative, $F^A_{\mu\nu}$ is the Yang-Mills gauge field and λ_A is the gaugino superpartner of the corresponding gauge boson. It is worth noticing that the $\sum_i$ is a sum over all fermion fields of the SM, the scalar partners and the 2 Higgs doublets with their fermion partners. On the other hand, $\sum_A$ is over the $SU(3)_c$, $SU(2)_L$ and $U(1)_Y$ gauge fields with their fermion partners, the gauginos.

The interactions between bosons and fermions are completely determined by the gauge symmetries and by the supersymmetry:

$$\begin{aligned}\mathcal{L}_{int} = & -\sqrt{2}\sum_{i,A} g_A \left[S_i^* T^A \bar{\psi}_{iL} \lambda_A + \text{h.c.} \right] \\ & - \frac{1}{2}\sum_A \left(\sum_i g_A S_i^* T^A S_i \right)^2 ,\end{aligned} \tag{2.56}$$

where $\psi_L \equiv \frac{1}{2}(1-\gamma_5)\psi$, T^A is the matrix of the group generators and g_A the gauge coupling constants. It can be seen that there are no adjustable parameter, hence, all interaction strengths are completely fixed in terms of SM coupling constants.

Once the superfields and the gauge symmetries are chosen, the only freedom in constructing $\mathcal{L}_{MSSM}$ is contained in a function called *superpotential*, $\mathcal{W}$. This is an analytic form of the chiral superfields, $\hat{S}$, that has the form:

$$\mathcal{W} = \epsilon_{ij}\mu \hat{H}_u^i \hat{H}_d^j + \epsilon_{ij}\left[\lambda_L \hat{H}_d^i \bar{\hat{L}}^j \bar{\hat{E}} + \lambda_D \hat{H}_d^i \hat{Q} \bar{\hat{D}} + \lambda_U \hat{H}_u^j \hat{Q}^i \bar{\hat{U}} \right] + W_{RP} \tag{2.57}$$

where i and j are $SU(2)_L$ doublet indices and $\epsilon_{ij} = -\epsilon ji$ (with $\epsilon_{12} = 1$) contracts the $SU(2)_L$ doublet fields. No derivative interactions are allowed in order that $\mathcal{W}$ be an analytical function. The term $\mu \hat{H}_u^i \hat{H}_d^j$ gives mass terms for the Higgs bosons and so μ is often called the Higgs mass parameter. The terms in the square brackets proportional to λ_L, λ_D and λ_U give the usual Yukawa interactions of the fermions with the Higgs bosons. Hence, unlike the SM case, these coefficients are determined in terms of the fermion masses and the vacuum expectation values of the neutral members of the scalar components, and are not arbitrary couplings.

In the most general superpotential one can add more terms which are grouped under W_{RP} in equation 2.57. These terms are of the form:

$$W_{RP} = \lambda_{\alpha\beta\gamma}\hat{L}^{\alpha}\hat{L}^{\beta}\bar{\hat{E}}^{\gamma} + \lambda'_{\alpha\beta\gamma}\hat{L}^{\alpha}\hat{Q}^{\beta}\bar{\hat{D}}^{\gamma} + \lambda''_{\alpha\beta\gamma}\bar{\hat{U}}^{\alpha}\bar{\hat{D}}^{\beta}\bar{\hat{D}}^{\gamma} + \mu'\hat{L}\hat{H} \tag{2.58}$$

where the indices $\alpha,\ \beta$ and γ label the 3 generations of quarks and leptons. These terms constitute a problem in the sense that the first two contribute to lepton number violation interactions and the third one to baryon number violation interactions[5]. The combination of lepton and baryon violation terms can contribute to the proton decay at tree level through the exchange of the scalar partner of the down quark. Since this process is experimentally restricted [42, 43, 44, 45, 46, 47, 48, 49] it put into question the validity of the model. One solution is to assume that the parameters are small enough to avoid experimental limits. Even this is certainly allowed experimentally, this would imply the introduction of an artificial tuning. The other solution is to introduce a new symmetry called R-parity [50, 51, 52, 53, 54, 55, 56]. R-parity (R_p) is a multiplicative quantum number defined as:

$$R = (-1)^{3(B-L)+2s}\ , \tag{2.59}$$

where B and L are the baryon and lepton quantum numbers and s is the spin of the particle. Thus, all SM particles have $R_p = +1$ while their SUSY partners have $R_p = -1$.

The assumption of such a symmetry prevents lepton and baryon number violating terms but has also dramatic phenomenological consequences: exists no mixing between the sparticles and the $R_P = 1$ particles, SUSY particles can only be pair-produced in the collisions of SM particles and a SUSY particle would undergo a chain of decays until the lightest SUSY particle (LSP) is produced. Then, this LSP cannot decay further and constitutes a cold dark matter candidate[6].

2.2.6 SUSY Breaking

At this point, the MSSM Lagrangian does not provide mass terms for all the particles (fermions, scalars, gauge fields). If supersymmetry was an exact symmetry, squarks and quarks would have equal masses and gluinos would be massless. Since this is not the case in nature, at low energies supersymmetry must be a broken symmetry and new SUSY-breaking terms need to be introduced in the Lagrangian. To prevent dangerous quadratic divergences, only a certain subset

[5]The fourth term can be ignored since one can implement a rotation in the lepton field $\hat{L}$ such that this term vanishes [41].

[6]Due to cosmological constraints, a cold dark matter candidate need to be stable and neutral [57, 58].

of supersymmetry-breaking terms are allowed to be present in the theory and their couplings are denoted as *soft* parameters. Then, the so-called soft Lagrangian which break SUSY is (first generation only):

$$\begin{aligned}
-\mathcal{L}_{soft} = & \frac{1}{2}\left[M_3\hat{g}\hat{g} + M_2\hat{W}\hat{W} + M_1\hat{B}\hat{B}\right] \\
& + \epsilon_{\alpha\beta}\left[-bH_d^\alpha H_u^\beta - H_u^\alpha \hat{Q}_i^\beta \hat{A}_{u_{ij}}\bar{\hat{U}}_j + H_d^\alpha \hat{Q}_i^\beta \hat{A}_{d_{ij}}\bar{\hat{D}}_j + H_d^\alpha \hat{L}_i^\beta \hat{A}_{e_{ij}}\bar{\hat{E}}_j + \mathrm{h}.c.\right] \\
& + m_{H_d}^2|H_d|^2 + m_{H_u}^2|H_u|^2 + \hat{Q}_i^\alpha m_{Q_{ij}}^2 \hat{Q}_j^{\alpha *} \\
& + \hat{L}_i^\alpha m_{L_{ij}}^2 \hat{L}_j^{\alpha *} + \bar{\hat{U}}_i^* m_{U_{ij}}^2 \bar{\hat{U}}_j + \bar{\hat{D}}_i^* m_{D_{ij}}^2 \bar{\hat{D}}_j + \bar{\hat{E}}_i^* m_{E_{ij}}^2 \bar{\hat{E}}_j \ ,
\end{aligned} \tag{2.60}$$

where i and j are the $SU(2)_L$ doublet indices. This Lagrangian has arbitrary masses for the scalars and gauginos and also arbitrary bi-linear and tri-linear mixing terms. The scalar and gaugino mass terms have the desired effect of breaking the mass degeneracy between the particles and their SUSY partners. The tri-linear A terms affect primarily the particles of the third generation. The μB term mixes the scalar components of the two Higgs doublets. In the most general case, all of the mass and interaction terms of equation 2.60 are matrices involving all three generators. However, the origin of all these terms is left unspecified. How supersymmetry breaking is transmitted to the superpartners is encoded in the parameters of $\mathcal{L}_{soft}$. All of the quantities in $\mathcal{L}_{soft}$ receive radiative corrections and thus are scale-dependent, satisfying known Renormalisation Group Equations (RGEs).

For phenomenological purposes, the described Lagrangian is simply a low energy effective Lagrangian with a number of input parameters. The fact that except for the assumption of the presence of supersymmetric particles, R_p, and gauge and Poincaré invariance, nothing else has been assumed, makes the MSSM a very simple framework but one needs to introduce plenty of free input parameters. MSSM includes at least 105 new parameters that added to the 19 parameters of the SM, the model has 124 parameters to be determined[7]. While often only subsets of these parameters are relevant for particular experimental processes and there exist some phenomenological constraints in these parameters, the number is too large for practical purposes to carry out phenomenological analyses in full generality.

However, unlike in the SM case, now there is the possibility to stablish a top-down approach by which the MSSM parameters are predicted within the context of an underlying theory, often as functions of fewer basic parameters. The basic question to be addressed is how to understand the explicit soft supersymmetry breaking encoded in the $\mathcal{L}_{soft}$ parameters as the result of spontaneous supersymmetry breaking in a more fundamental theory. Since this is not known,

[7]For this particular reason, sometimes it is referred to as MSSM-124.

different models have been constructed as an attempt to find an answer for this question. Since TeV-scale supersymmetry-breaking models have reported negative results [59], other models which assume that the theory can be splitted into at least two sectors have been considered. These two sectors have no direct renormalizable couplings between them and they are divided into *observable* or *visible* sector, which contains the SM fields and their superpartners, and the *hidden* sector, in which supersymmetry is spontaneously broken by a dynamical mechanism.

Within this framework, SUSY breaking is communicated from the hidden sector where it originates to the observable sector via suppressed interactions involving a third set of fields, the *mediator* or *messenger* fields. This hidden sector implies that the fundamental scale of supersymmetry breaking μ_s is hierarchically larger than the TeV scale. Depending on the model this μ_s can be postulated to be at the GUT scale, Majorana neutrino mass scale or in extra-dimensional braneworlds. Therefore, different models account for specific mechanisms for how supersymmetry breaking is mediated between the hidden and observable sectors and involve specific energy scales at which the soft terms are generated. These values are then used to compute the corresponding values at observable energy scales, all predicted at the TeV scale by the models, using the scale dependence of the $\mathcal{L}_{soft}$ parameters as dictated by their RGEs.

2.3 Third Generation Squarks

In the MSSM, the SM quark helicity states q_L and q_R have scalar MSSM super-partners, which are also the mass eigenstates (in good approximation) for the first two generations. However, for the third generation, strong mixing of these states may appear depending on the theoretical parameters: $\tan\beta$ and $\mathrm{A}_{t,b}$ (the Higgs-sbottom trilinear coupling).

This thesis presents two searches for third generation squarks at CDF Run II. The following sections discuss the motivation for the particular final states selected in these analyses.

2.3.1 Scalar Bottom from Gluino Decay

Several models [60], assuming large $\tan\beta$, predict that the mixing in the mass eigenstates might be substantial for the scalar bottom, yielding a $\tilde{b}$ mass eigenstate significantly lighter than other squarks:

$$m^2_{\tilde{b}_{1,2}} = \frac{1}{2}[m^2_{\tilde{b}_L} + m^2_{\tilde{b}_R} \pm \sqrt{(m^2_{\tilde{b}_L} - m^2_{\tilde{b}_R})^2 + 4m^2_b(A_b - \mu tan\beta)^2}] \tag{2.61}$$

Moreover, the gluino pair production cross section is almost an order of magnitude larger than a sbottom of similar mass [61]. At the Tevatron energies, gluinos are produced mainly through quark-antiquark annihilation and gluon fusion, figure 2.6, with the former dominating for high x. If the sbottom is light enough, then the two body decay $\tilde{g} \rightarrow b\tilde{b}$ would be kinematically allowed.

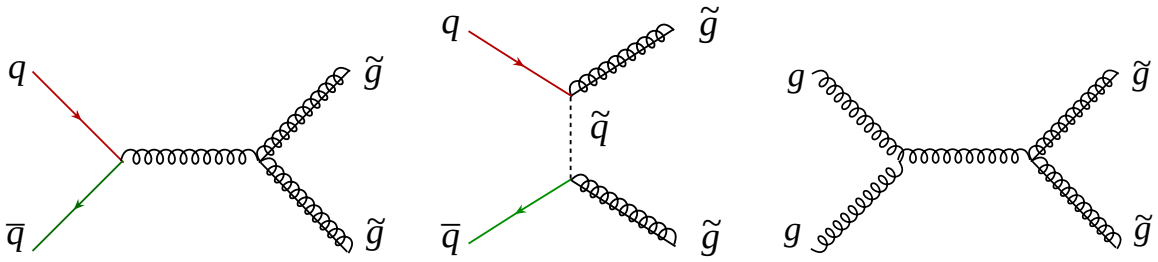

Figure 2.6: Leading order gluino pair production mechanisms at the Tevatron center of mass energies.

In the region of interest for this analysis ($m_t, m_{\tilde{\chi}^+} > m_{\tilde{b}} > m_{\tilde{\chi}^0}$), the dominant decay channel is sbottom into bottom quark and neutralino $\tilde{b} \rightarrow b\tilde{\chi}^0$, with no other available decays channels, since we require $m_{\tilde{b}} < m_t, m_{\tilde{\chi}^+}$. Hence, we assume a Branching Ratio of 100% for the $\tilde{b} \rightarrow b\tilde{\chi}^0$ decay, and the fully gluino decay chain will be as shown in figure 2.7.

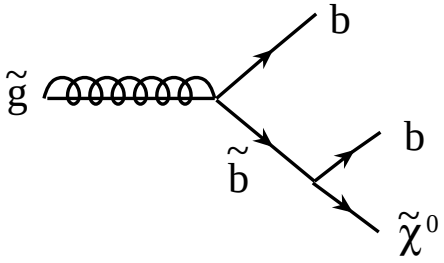

Figure 2.7: Gluino decay into bottom quark and sbottom.

One could also think a scenario where the second neutralino $\tilde{\chi}_2^0$ is lighter than the sbottom quark. In this case $\tilde{b} \rightarrow b\tilde{\chi}_2^0$, with the second lightest neutralino decaying into leptons and LSP ($\tilde{\chi}_2^0 \rightarrow ll\tilde{\chi}_1^0$). Such a signature could be observed by multileptons search and is not considered here.

In order to get the predictions for our signal, we use the program PROSPINO [61] to compute the total production cross section and PYTHIA [62] to estimate the event acceptance in the

detector and in the application of our selection cuts.

For the NLO cross sections of gluino pairs, the calculation does not depend on the sbottom mass or the neutralino mass. However, there is a dependence on the mass of the first squarks due to their presence in the diagrams. The main dominant contribution is coming from those squarks associated to the lightest quarks, specifically $\tilde{u}$ and $\tilde{d}$ due to their presence as valence quarks in the proton and antiproton. Figure 2.8 shows the cross section of gluino-pair production for $m(\tilde{g}) = 250 \ \ \mathrm{GeV}/c^2$ and $m(\tilde{g}) = 350 \ \ \mathrm{GeV}/c^2$ as a function of the squark masses[8]. We observe a strong dependence for the Leading-order and Next-to-leading cross sections on the mass of the squarks.

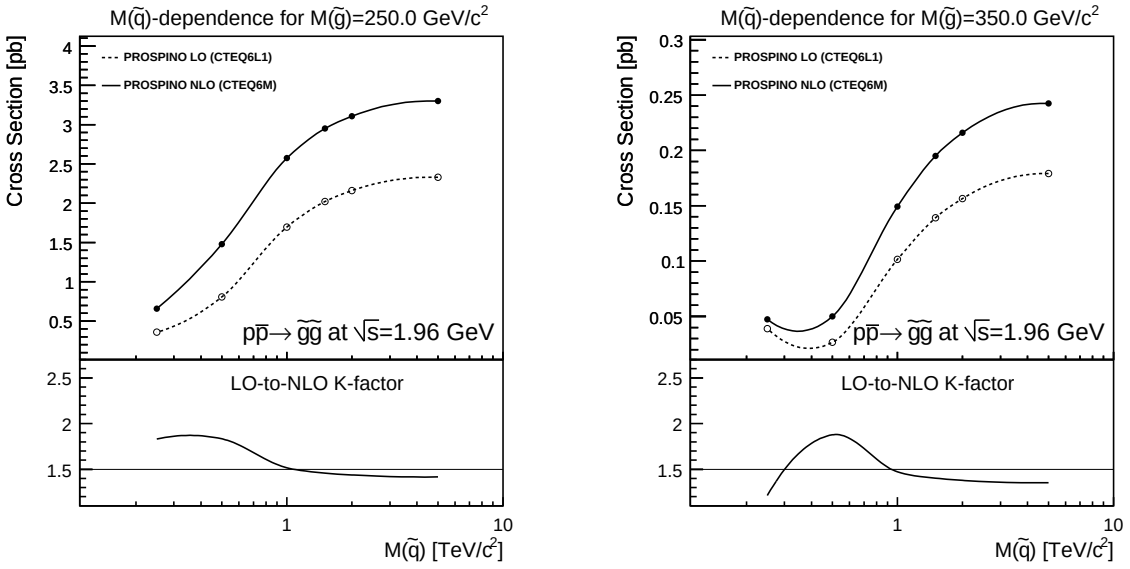

Figure 2.8: LO and NLO cross section of gluino-pair production at the Tevatron Run II as predicted by PROSPINO as a function of the mass of the squarks of the first two families. The predictions are shown for values of the gluino mass of 250 GeV/c^2 (left) and 350 GeV/c^2 (right).

Due to this dependence, the analysis needs to be performed with a clear assumption on the mass of the squarks. We decided to use the value of 500 GeV/c^2 as it was done in previous analyses [63]. This value leads to a reasonably conservative estimate of the cross section since the larger the mass of the squark, the larger the cross section. Using a value much smaller than 500 GeV/c^2 may break the assumption that the decay of the gluino is dominated by $\tilde{g} \rightarrow b\tilde{b}_1$.

Under this assumption, we compute the cross section of the gluino-pair production process

[8] As this is done in PROSPINO, the masses of the squarks associated to the light quarks are degenerated, and we always assume that.

for the range of masses we are interested in. This is shown in figure 2.9 using the CTEQ6M set of Parton Distribution Functions [64, 65]. The cross section falls very rapidly when increasing the mass of the gluino, but the absolute values are reasonable for the analysis to reach unexcluded regions of the parameter space.

As a comparison, figure 2.9 also shows the equivalent cross section for sbottom-pair production. It should be noticed that for similar masses of the gluino and sbottom, the production of gluino has a much larger cross section, leading to the fact that even for smaller mass of the sbottom, the channel we are considering here provides larger sensitivity than the direct search of sbottom-pair production due to a larger cross section and a signature that is much cleaner than that of the sbottom-pair production. This makes specially interesting the degeneration mass region for which, we perform an specific optimization in the analysis.

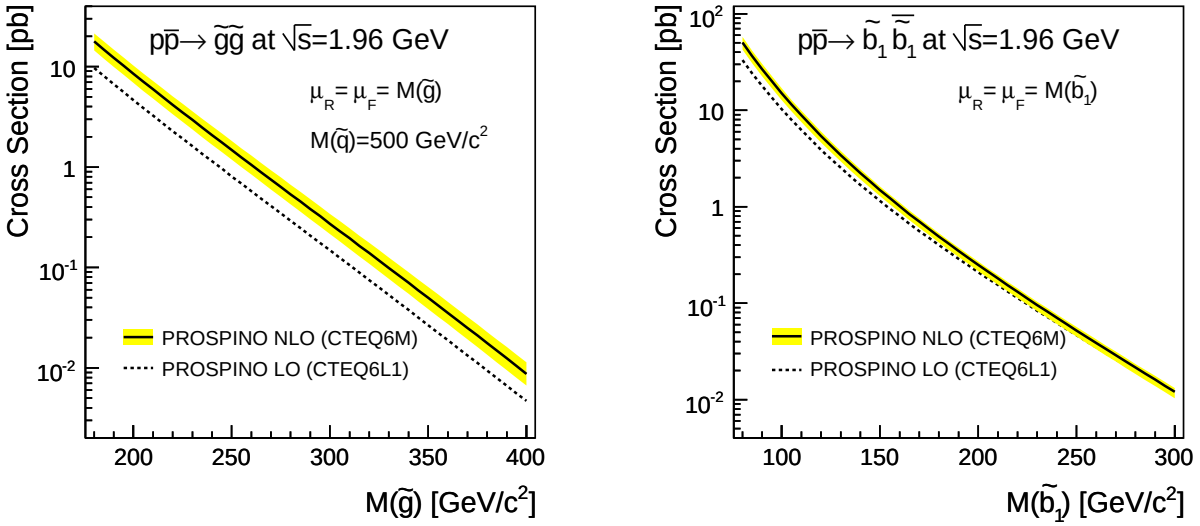

Figure 2.9: LO and NLO cross sections of gluino-pair production (left), and sbottom-pair production (right) at the Tevatron Run II as predicted by PROSPINO as a function of their masses. A mass of 500 GeV$/c^2$ has been assumed, for the squarks of the first two families, in the gluino-pair production calculation.

We also have studied the dependence of the acceptance with the mass of the squarks, using samples generated with different values of that parameter. It should be remarked that the assumed masses for the squarks of the first two families are degenerated. The result of this study is shown in figure 2.10 where we observe that such a dependence is really marginal. This imply that the analysis may be performed independently of the assumed mass of the squarks. However, due to the large dependence of the gluino-pair production cross section on this parameter,

the interpretation of the final result can only be done with the assumption of a specific value of that mass, being that 500 GeV/c^2, as motivated above.

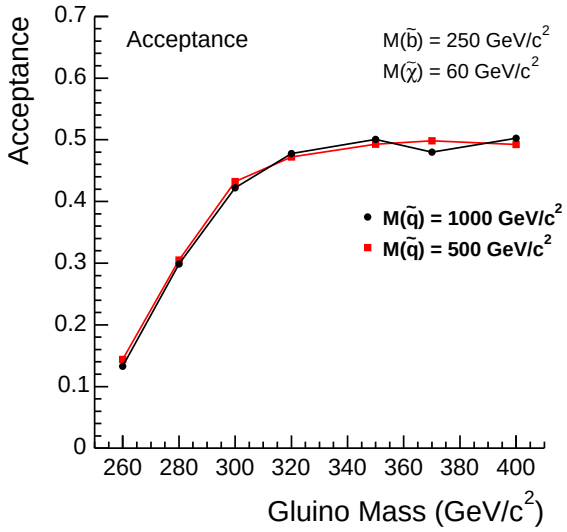

Figure 2.10: Acceptance efficiency as a function of the gluino mass for two different assumptions of the squark mass for fixed values of the other parameters.

2.3.2 Scalar Top Decaying into Charm and Neutralino

Due to the large mass of the top quark, the mass splitting between the two stop quarks states ($\tilde{t}_1, \tilde{t}_2$) may be large, allowing $\tilde{t}_1$ to likely be the lightest squark, and possibly even lighter than the top quark:

$$m^2_{\tilde{t}_{1,2}} = \frac{1}{2}[m^2_{\tilde{t}_L} + m^2_{\tilde{t}_R} \pm \sqrt{(m^2_{\tilde{t}_L} - m^2_{\tilde{t}_R})^2 + 4m^2_t(A_t - \mu cot\beta)^2}] \tag{2.62}$$

Assuming R-parity conservation, scalar top quarks are pair produced, as is shown in figure 2.11, and the Lightest Supersymetric Particle (LSP) must be stable. If it is colorless and neutral, then it will escape from the detector undetected yielding large missing transverse energy ($\not{E}_T$).

This scenario is accessible in the range $m_{\tilde{t}_1} < m_b + m_{\tilde{\chi}^+}$ and $m_{\tilde{t}_1} < m_W + m_b + m_{\tilde{\chi}^0}$ in which the dominant $\tilde{t}_1$ decay mode is the flavor changing process $\tilde{t}_1 \rightarrow c\tilde{\chi}^0$ which is typically assumed to occur with 100% branching fraction, as shown in figure 2.12. The $\tilde{t}_1 \rightarrow t\tilde{\chi}^0$ decay

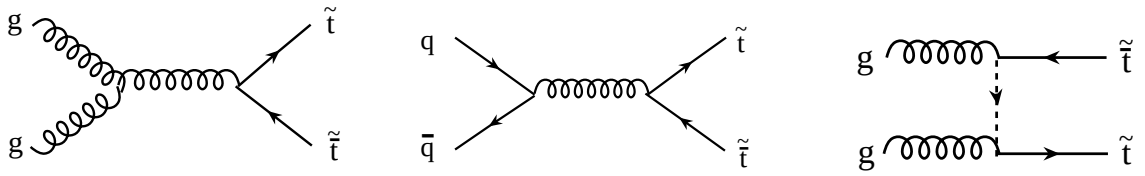

Figure 2.11: Leading order stop pair production diagrams at the Tevatron center of mass energies.

is kinematically forbidden over the $\tilde{t}_1$ mass range currently accessible at Tevatron, and the tree level four-body decays $\tilde{t}_1 \rightarrow bff'\tilde{\chi}^0$ is negligible. In this particular case the experimental signature consists of two c jets and $\not\!\!E_T$ from the undetected $\tilde{\chi}^0$.

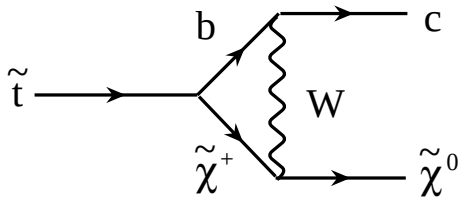

Figure 2.12: Stop decay into charm and neutralino.

In order to get the predictions for our signal, similarly to the gluino-sbottom analysis, we use the program PROSPINO to compute the total production cross section and PYTHIA to estimate the event acceptance in the detector and in the application of our selection cuts.

We compute the cross section of the stop-pair production process for the range of masses we are interested in. This is shown in figure 2.13 using the CTEQ6M set of PDFs. The cross section falls very rapidly when increasing the mass of the stop, but the absolute values are reasonable for the analysis to reach unexcluded regions of the parameter space.

For the NLO cross sections of stop pairs, the calculation does not depend on the neutralino mass, and the dependence on masses of other sparticles is very small, since it appears as part of the NLO corrections.

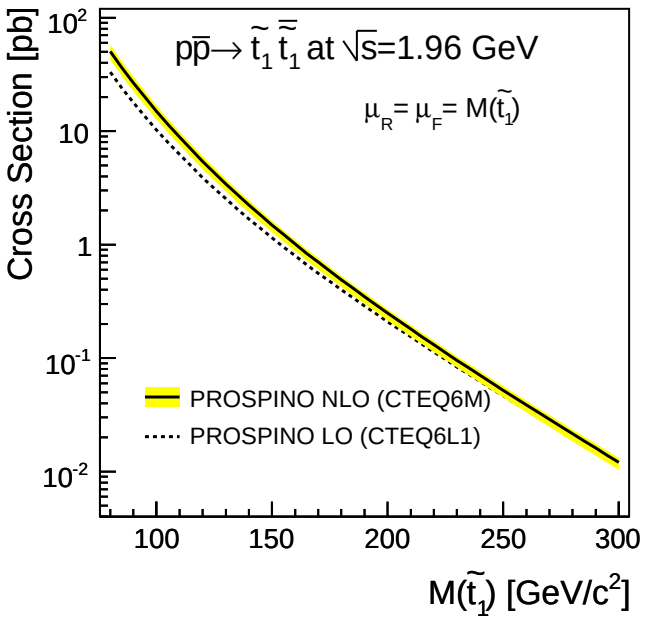

Figure 2.13: LO and NLO cross sections of stop-pair production at the Tevatron Run II as computed using PROSPINO as a function of the stop mass.

Chapter 3

Experimental Setup

The Fermilab Tevatron is the highest energy hadron collider in operation, until the completion of the Large Hadron Collider (LHC) at CERN. After a major upgrade, the Tevatron Run II provides proton-antiproton ($p\bar{p}$) collisions with a center of mass energy of 1.96 TeV and a bunch crossing period of 396 ns. Two detectors were designed to extract the full scientific potential of these collisions: CDF, the Collider Detector at Fermilab and DØ . Both of them follow the usual structure of high energy physics experiments with a tracker, inside a solenoidal magnetic field, a calorimeter and a muon spectrometer, arranged in concentrical layers and two plugs.

The results presented in the thesis make use of approximately 2.6 fb^{-1} amount good-quality of data collected by CDF. A brief description of the accelerator chain and the detector is presented in the following sections.

3.1 The Tevatron Collider

The Tevatron Collider [66] located at the Fermi National Accelerator Laboratory (Fermilab) in Batavia (Illinois, USA) is a proton-antiproton ($p\bar{p}$) collider with a center-of-mass energy of 1.96 TeV. As shown in figure 3.1, this complex has five major accelerators and storage rings used in successive steps, as is explained in detail below, to produce, store, and accelerate the particles up to 980 GeV.

The acceleration cycle starts with the production of protons from ionized hydrogen atoms H^-, which are accelerated to 750 KeV by a Cockroft-Walton electrostatic accelerator. Pre-accelerated hydrogen ions are then injected into the Linac where they are accelerated up to 400 MeV by passing through a 150 m long chain of radio-frequency (RF) accelerator cavities. A

carbon foil strips off the electrons of the H^- ions, thus producing protons. Inside the Booster the protons are merged into bunches and accelerated up to an energy of 8 GeV prior to entering the Main Injector. In the Main Injector, a synchrotron with a circumference of 3 km, the proton bunches are accelerated further to an energy of 150 GeV and coalesced[1] together before injection into the Tevatron.

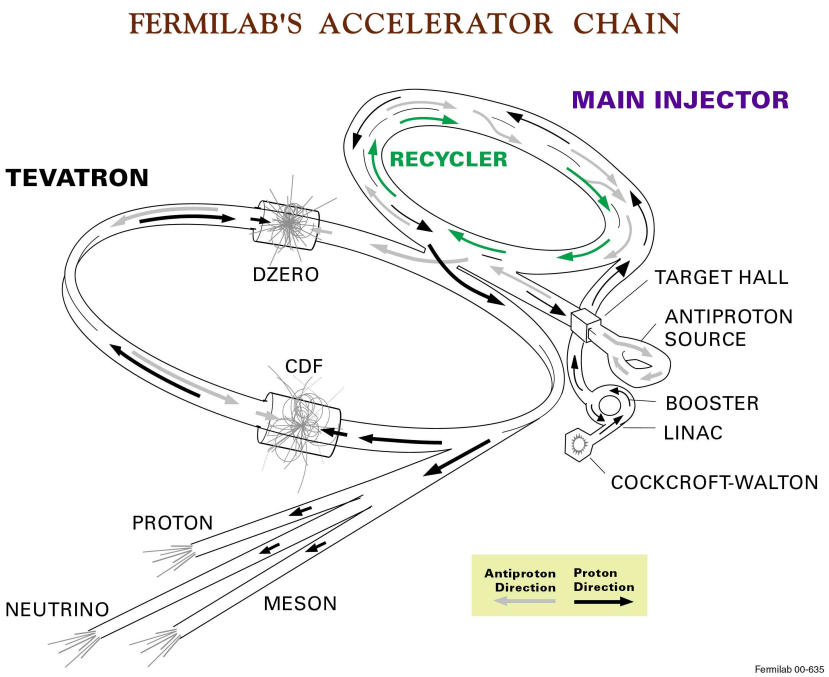

Figure 3.1: The Tevatron Collider Chain at Fermilab.

The production of the antiproton beam is significantly more complicated. The cycle starts with extracting a 120 GeV proton beam from the Main Injector onto a stainless steel target. This process produces a variety of different particles, among which antiprotons appear[2]. The particles come off the target at many different angles and they are focused into a beam line with a Lithium lens. In order to select only the antiprotons, the beam is sent through a pulsed magnet which acts as a charge-mass spectrometer. The produced antiprotons are then injected into the Debuncher, an 8 GeV synchrotron, which reduces the spread in the energy distribution of the antiprotons. After that, the antiproton beam is directed into the Accumulator, a storage ring in the Antiproton Source, where the antiprotons are stored at an energy of 8 GeV and stacked to 10^{12} particles per bunch. The antiproton bunches are then injected into the Main Injector and accelerated to 150 GeV.

[1] Coalescing is the process of merging proton bunches into one dense, high density beam

[2] The production rate, for 8 GeV antiprotons, is about $18\ \bar{p}$ per $10^6\ p$

Finally, 36 proton and antiproton bunches are inserted into the Tevatron, a double acceleration ring of 1 km of radius, where their energy is increased up to 980 GeV. Proton and antiproton bunches circulate around the Tevatron in opposite directions guided by superconducting magnets and where their orbits cross at the two collision points to produce the $p\bar{p}$ interaction that are observed. These interactions are observed by the CDF and DØ detectors.

In the absence of a crossing angle or position offset, the luminosity at the interaction points is given by the expression:

$$L = \frac{f_{bc} N_b N_p N_{\bar{p}}}{2\pi(\sigma_p^2 + \sigma_{\bar{p}}^2)} F\left(\frac{\sigma_l}{\beta^*}\right), \tag{3.1}$$

where f_{bc} is the revolution frequency, N_b is the number of bunches, $N_{p(\bar{p})}$ is the number of protons (antiprotons) per bunch, and $\sigma_{p(\bar{p})}$ is the transverse and longitudinal rms proton (antiproton) beam size at the interaction point. F is a form factor with a complicated dependence on the so-called beta function, β^*, and the bunch length, σ_l. The beta function is a measure of the beam width, and it is proportional to the beam's x and y extent in phase space. Table 3.1 shows the design Run II accelerator parameters [67].

Parameter	Run II
number of bunches (N_b)	36
revolution frequency [MHz] (f_{bc})	1.7
bunch rms [m] σ_l	0.37
bunch spacing [ns]	396
protons/bunch (N_p)	2.7×10^{11}
antiprotons/bunch ($N_{\bar{p}}$)	3.0×10^{10}
total antiprotons	1.1×10^{12}
β^* [cm]	35

Table 3.1: Accelerator parameters for Run II configuration.

Figure 3.2 and figure 3.3 show, respectively, the evolution in the integrated luminosity, defined as $\mathcal{L} = \int L\, dt$, and the instantaneous luminosity delivered by Tevatron since the machine was turned on up to July 2009. The progressive increase in the integrated luminosity and the continuous records in the instantaneous luminosity [3] prove the good performance of the accelerator.

[3] As of July 2009, the record in the instantaneous luminosity was close to $3.5 \times 10^{32} cm^{-2} s^{-1}$.

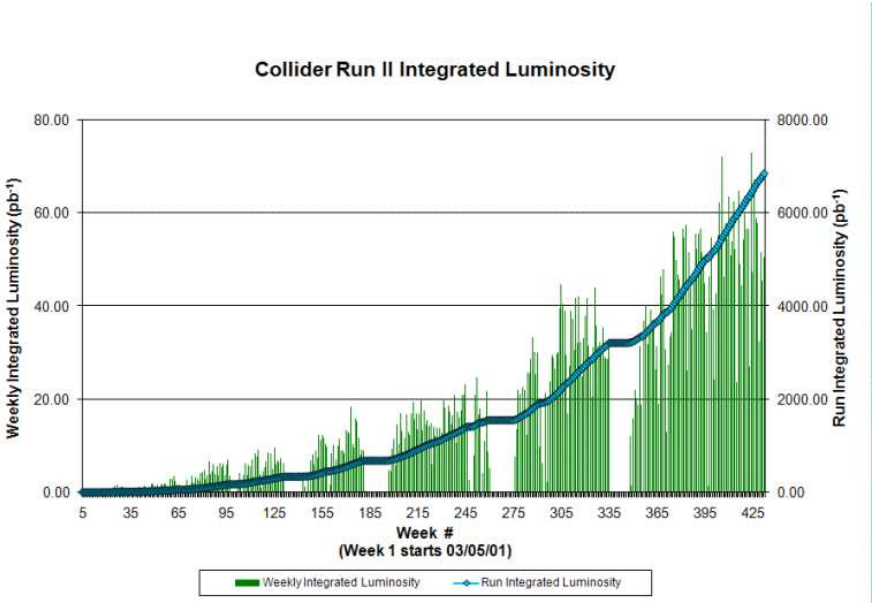

Figure 3.2: Tevatron Collider Run II Integrated Luminosity. The vertical green bar shows each week's total luminosity as measured in pb^{-1}. The diamond connected line displays the integrated luminosity.

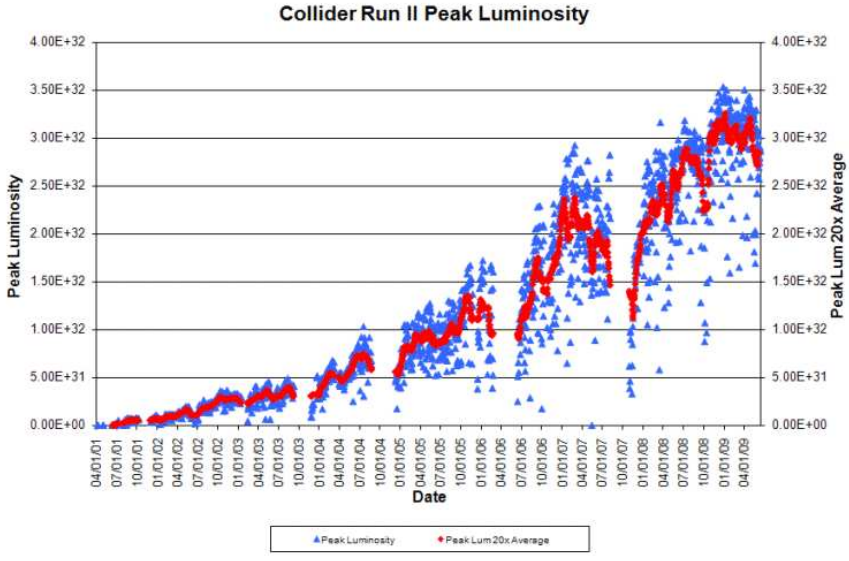

Figure 3.3: Tevatron Collider Run II Peak Luminosity. The blue squares show the peak luminosity at the beginning of each store and the red triangle displays a point representing the last 20 peak values averaged together.

3.2 CDF Run II Detector

The CDF Run II detector [68], in operation since 2001, is an azimuthally and forward-backward symmetric apparatus designed to study $p\bar{p}$ collisions at the Tevatron. It is a general purpose, cylindrical-shaped detector which combines:

- A tracking system, that provides a measurement of the charged particle momenta, event z vertex position and allows the reconstruction of secondary vertices.
- A non-compensated calorimeter system, with the purpose of measuring the energy of charged and neutral particles produced in the interaction.
- Drift chambers and scintillators for muon detection.

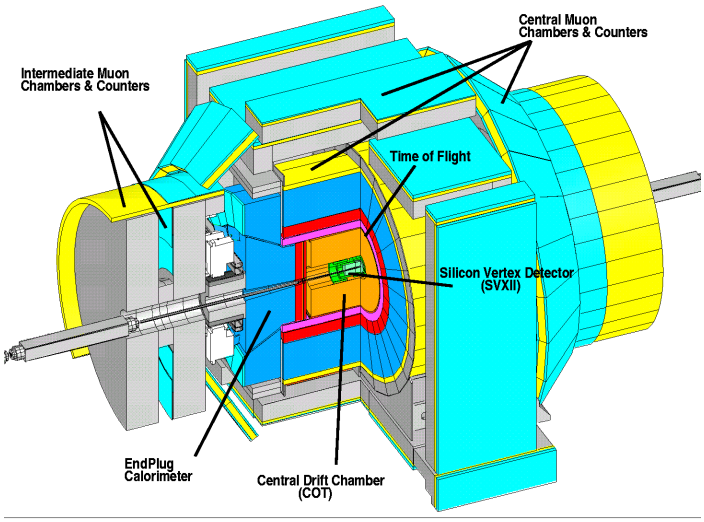

Figure 3.4: Isometric view of the CDF Run II detector with human-size references. Only half of the detector is shown.

The detector is shown in figure 3.4 and figure 3.5. CDF uses a cylindrical coordinate system where the positive z-axis lies along the direction of the incident proton beam, θ and ϕ are the polar and azimuthal angles, respectively, and pseudorapidity is $\eta = -\ln(\tan(\frac{\theta}{2}))$. The p_T and E_T are the components of momentum and energy, in the transverse plane. The missing E_T ($\vec{\not\!\!E}_T$) is defined by $\vec{\not\!\!E}_T = -\sum_i E_T^i \hat{\mathbf{n}}_\mathbf{i}$, i = calorimeter tower number, where $\hat{\mathbf{n}}_\mathbf{i}$ is a unit vector perpendicular to the beam axis and pointing at the i^{th} calorimeter tower. $\vec{\not\!\!E}_T$ is corrected for high-energy muons and jet energy. A description of all the systems starting from the devices closest to the beam and moving outward is presented in the next sections, where the detectors most relevant in the analysis are explained in more detail.

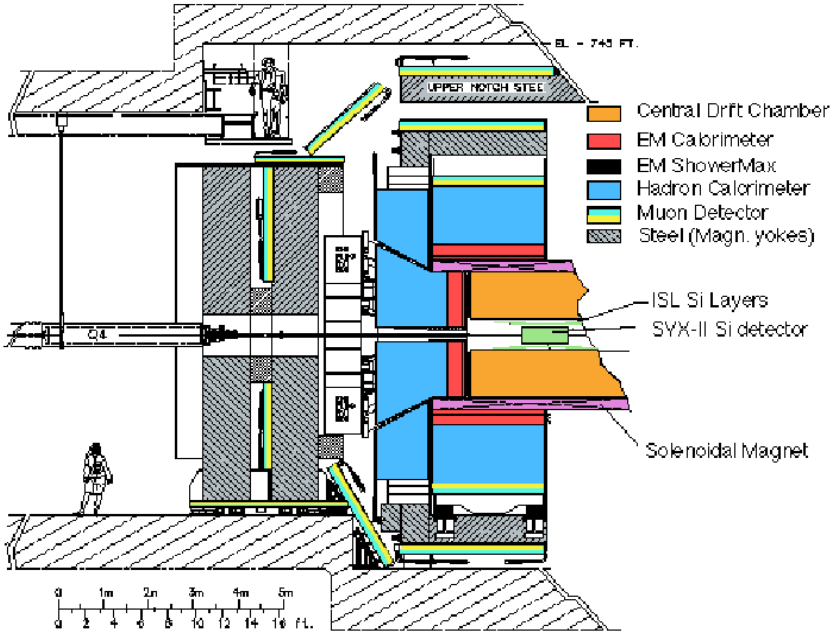

Figure 3.5: $r \times \eta$ side view of the CDF Run II detector.

3.2.1 Tracking and Time of Flight Systems

The tracking and time of flight systems are contained in a superconducting solenoid, 1.5 m in radius and 4.8 m in length, which generates a 1.4 T magnetic field parallel to the beam axis.

The part of the tracking system closest to the beam pipe is a silicon microstrip detector [69], which is radiation-hard due its proximity to the beam. It extends from a radius of 1.2 cm, the beam pipe, to 28 cm, covering $|\eta| < 2$ and has eight layers in a barrel geometry. The innermost layer is a single-sided silicon microstrip detector called Layer 00 (L00) which provides a $r \times \phi$ position measurement. The first five layers after the L00 constitute the Silicon Vertex Detector (SVXII) and the two outer layers comprise the Intermediate Silicon Layers system (ISL). These seven layers are made of double-sided silicon sensors, giving $r \times \phi$ and z position information. The best position resolution achieved is 9 μm in SVXII and the impact parameter resolution, including L00, reaches 40 μm for tracks with $p_T > 3$ GeV/c.

Surrounding the silicon detector is the Central Outer Tracker (COT) [70], the anchor of the CDF Run II tracking system. It is a 3.1 m long cylindrical drift chamber that covers the radial range from 40 to 137 cm and full coverage up to $|\eta| \sim 1$. The COT contains 96 sense wire layers, which are radially grouped into eight "superlayers", as inferred from the end plate

section shown in figure 3.6.

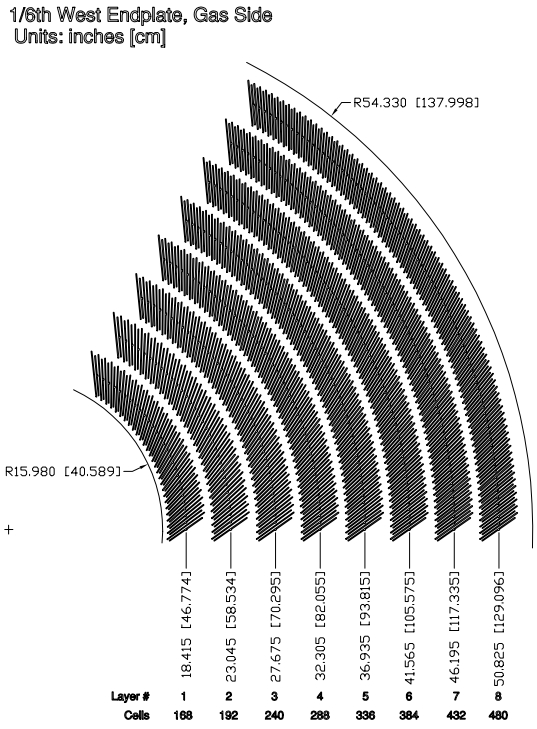

Figure 3.6: Layout of wire planes on a COT endplate.

Each superlayer is divided in ϕ into "supercells", and each supercell has 12 sense wires and a maximum drift distance that is approximately the same for all superlayers. Therefore, the number of supercells in a given superlayer scales approximately with the radius of the superlayer. The entire COT contains 30,240 sense wires. Approximately half the wires run along the z direction ("axial"). The other half are strung at a small angle ($\pm 2^{\circ}$) with respect to the z direction ("stereo"). The combination of the axial and stereo information allows the measurement the z positions. Particles originated from the interaction point, having $|\eta| < 1$, pass through all 8 superlayers of the COT.

The supercell layout, shown in figure 3.7 for superlayer 2, consists of a wire plane containing sense and potential wires, for field shaping and a field (or cathode) sheet on either side. Both the sense and potential wires are 40 μm diameter gold plated tungsten. The field sheet is 6.35 μm thick Mylar with vapor-deposited gold on both sides. Each field sheet is shared with the neighboring supercell.

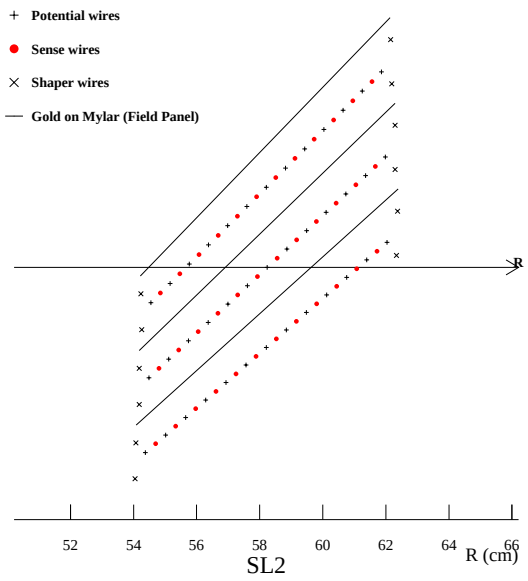

Figure 3.7: Layout of wires in a COT supercell.

The COT is filled with an Argon-Ethane gas mixture and Isopropyl alcohol $(49.5 : 49.5 : 1)$. The mixture is chosen to have a constant drift velocity, approximately 50 μm/ns across the cell width and the small content of isopropyl alcohol is intended to reduce the aging and build up of debris on the wires. When a charged particle passes through, the gas is ionized. Electrons drift toward the sense wires. Due to the magnetic field that the COT is immersed in, electrons drift at a Lorentz angle of $35°$. The supercell is tilted by $35°$ with respect to the radial direction to compensate for this effect. The momentum resolution of the tracks in the COT chamber depends on the p_T and is measured to be approximately 0.15%, with corresponding hit resolution of about 140 μm [71]. In addition to the measurement of the charged particle momenta, the COT is used to identify particles, with $p_T > 2$ GeV, based on dE/dx measurements.

Just outside the tracking system, CDF II has a Time of Flight (TOF) detector [72, 73, 74]. It consist on a barrel of scintillator, almost 3 m long, located at 140 cm from the beam line with a total of 216 bars, each covering 1.7^o in ϕ and pseudorapidity range $|\eta| < 1$. Particle identification is achieved by measuring the time of arrival of a particle at the scintillators with respect to the collision time. Thus, combining the measured time-of-flight and the momentum and path length, measured by the tracking system, the mass of the particle can then determined. The resolution in the time-of-flight measurement has achieved $\approx$ 100 ps and it provides at least two standard deviation separation between $K^{\pm}$ and $\pi^{\pm}$ for momenta p < 1.6 GeV$/c$.

As a summary, figure 3.8 illustrates the Tracking and Time of Flight systems.

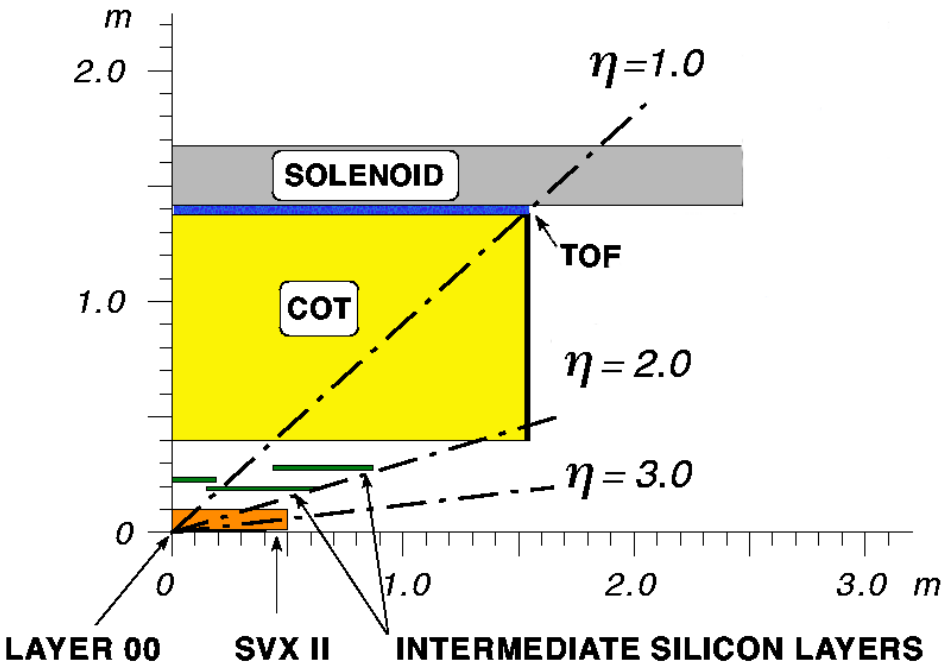

Figure 3.8: The CDF II tracker layout showing the different subdetector systems.

3.2.2 Calorimeter System

The calorimeter system is located surrounding the CDF tracking volume, outside of the solenoid coil. The different calorimeters that compose the system are scintillator-based detectors, segmented in projective towers (or wedges), in $\eta \times \phi$ space, that point to the interaction region. The total coverage of the system is 2π in ϕ and about $|\eta| < 3.64$ units in pseudorapidity.

The calorimeter system is divided in two regions: central and plug. The central calorimeter covers the region $|\eta| < 1.1$ and is split into two halves at $|\eta| = 0$. It conceived as a hybrid system of sampling scitilators and strip wire proportional chambers. The forward plug calorimeters cover the angular range corresponding to $1.1 < |\eta| < 3.64$, as it is shown in figure 3.9. Due to this structure, two "gap" regions are found at $|\eta| = 0$ and $|\eta| \sim 1.1$.

3.2.3 Central Calorimeters

The central calorimeters consist of 478 towers, each one is 15^o in azimuth times approximately 0.11 in pseudorapidity. Each wedge consists of an electromagnetic component backed by a hadronic section. In the central electromagnetic calorimeter (CEM) [75], the scintillators are

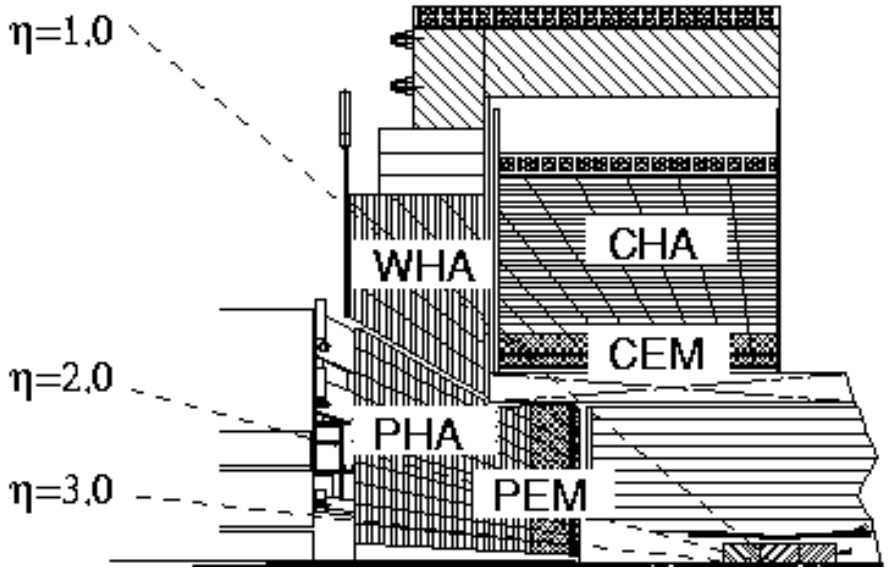

Figure 3.9: Elevation view of 1/4 of the CDF detector showering the components of the CDF calorimeter: CEM, CHA, WHA, PEM and PHA.

interleaved with lead layers. The total material has a depth of 18 radiation lengths [4](X_0). The central hadronic section (CHA) [76] has alternative layers of steel and scintillator and is 4.7 interaction length deep [5](λ_0). The endwall hadron calorimeter (WHA), with similar construction to CHA, is located with half of the detector behind the CEM/CHA and the other half behind the plug calorimeter. The function of the WHA detector is to provide a hadronic coverage in the region $0.9 < |\eta| < 1.3$. In the central calorimeter the light from the scintillator is redirected by two wavelength shifting (WLS) fibers, which are located on the ϕ surface between wedges covering the same pseudorapidity region, up through the light-guides into two photo-tubes (PMTs) per tower.

The energy resolution for each section was measured in the testbeam and, for a perpendicular incident beam, and it is parameterized as:

$$(\sigma/E)^2 = (\sigma_1/\sqrt{E})^2 + (\sigma_2)^2, \tag{3.2}$$

[4]The radiation length X_0 describes the characteristic amount of matter transversed, for high-energy electrons to lose all but $1/e$ of its energy by bremsstrahlung, which is equivalent to $\frac{7}{9}$ of the length of the mean free path for pair e^+e^- production of high-energy photons. The average energy loss due to bremsstrahlung for an electron of energy E is related to the radiation length by $\left(\frac{dE}{dx}\right)_{brems} = -\frac{E}{X_0}$ and the probability for an electron pair to be created by a high-energy photon is $\frac{7}{9}X_0$.

[5]An interaction length is the average distance a particle will travel before interacting with a nucleus: $\lambda = \frac{A}{\rho\sigma N_A}$, where A is the atomic weight, ρ is the material density, σ is the cross section and N_A is the Avogadro's number.

where the first term comes from sampling fluctuations and the photostatistics of PMTs, and the second term comes from the non-uniform response of the calorimeter. In the CEM, the energy resolution for high energy electrons and photons is $\frac{\sigma(E_T)}{E_T} = \frac{13.5\%}{\sqrt{E_T}} \oplus 1.5\%$, where E_T=$Esin\theta$, being θ the beam incident angle. Charge pions were used to obtain the energy resolution in the CHA and WHA detectors that are $\frac{\sigma(E_T)}{E_T} = \frac{50\%}{\sqrt{E_T}} \oplus 3\%$ and $\frac{\sigma(E_T)}{E_T} = \frac{75\%}{\sqrt{E_T}} \oplus 4\%$, respectively.

3.2.4 Plug Calorimeters

One of the major upgrades for the Run II was the plug calorimeter [77]. The new plug calorimeters are built with the same technology as the central components and replace the previous Run I gas calorimeters in the forward region. The $\eta \times \phi$ segmentation depends on the tower pseudorapidity coverage. For towers in the region $|\eta| < 2.1$, the segmentation is 7.5^o in ϕ and from 0.1 to 0.16 in the pseudorapidity direction. For more forward wedges, the segmentation changes to 15^o in ϕ and about 0.2 to 0.6 in η.

As in the central calorimeters, each wedge consists of an electromagnetic (PEM) and a hadronic section (PHA). The PEM, with 23 layers composed of lead and scintillator, has a total thickness of about 21 X_0 . The PHA is a steel/scintillator device with a depth of about 7 λ_0. In both sections the scintillator tiles are read out by WLS fibers embedded in the scintillator. The WLS fibers carry the light out to PMTs tubes located on the back plane of each endplug. Unlike the central calorimeters, each tower is only read out by one PMT.

Testbeam measurements determined that the energy resolution of the PEM for electrons and photons is $\frac{\sigma}{E} = \frac{16\%}{\sqrt{E}} \oplus 1\%$. The PHA energy resolution is $\frac{\sigma}{E} = \frac{80\%}{\sqrt{E}} \oplus 5\%$ for charged pions that do not interact in the electromagnetic component. Table 3.2 summarizes the calorimeter subsystems and their characteristics.

Calorimeter	Coverage	Thickness	Energy resolution (E in GeV)
CEM	$\|\eta\| < 1.1$	18 X_0	$\frac{13.5\%}{\sqrt{E_T}} \oplus 2\%$
CHA	$\|\eta\| < 0.9$	4.7 λ_0	$\frac{50\%}{\sqrt{E_T}} \oplus 3\%$
WHA	$0.9 < \|\eta\| < 1.3$	4.7 λ_0	$\frac{75\%}{\sqrt{E_T}} \oplus 4\%$
PEM	$1.1 < \|\eta\| < 3.6$	21 X_0, 1 λ_0	$\frac{16\%}{\sqrt{E}} \oplus 1\%$
PHA	$1.2 < \|\eta\| < 3.6$	7 λ_0	$\frac{80\%}{\sqrt{E}} \oplus 5\%$

Table 3.2: CDF II Calorimeter subsystems and characteristics. The energy resolution for the EM calorimeter is given for a single incident electron and that for the hadronic calorimeter for a single incident pion.

The central and forward parts of the calorimeter have their own shower profile detectors: shower maximum and preshower detectors. The Central Shower Maximum (CES) and the Plug Shower Maximum (PES) are positioned at about $6\ X_0$, while the Central Preradiator (CPR) and the Plug Preradiator (PPR) are located at the inner face of the calorimeters. These detectors help on particle identification, separating $e^{\pm}$, γs and $\pi^0 s$.

3.2.5 Muons System

The muon system, which consists of sets of drift chambers and scintillators, is installed beyond the calorimetry system as the radially outermost component of CDF Run II detector (r$\sim$3.5 m). The muon system [78] is divided into different subsystems: the Central Muon Detector, CMU, the Central Muon Upgrade Detector, CMP, the Central Muon Extension Detector, CMX, and the Intermediate Muon Detector, IMU.

The coverage of the muon systems is almost complete in phi, except some gaps, and spans in polar angle up to $|\eta| \approx 1.5$, figure 3.10. Attached to the calorimeter modules, the CMU consists of a stack of 4 layers of drift chambers. The different layers are slightly shifted in phi for better performance. These chambers are single-wired and the read-out is equipped with a TDC and an ADC at each end of the wire. The ϕ-position is then calculated from the drift time, measured with the TDC, while the hit z-position is found through harge division with the ADC.

The CMP forms a box around the detector of stacked drift chambers. A layer of 60 cm of steel, partially used for the magnetic field return, provides the needed shielding to absorb particles, other than muons, leaking the calorimeter. This system overlaps with the CMU, and covers the central part.

The CMX detector, located forward than CMU and CMP, consists of stacked cells of drift tubes conforming a conical section. The chambers are stacked at a small angle, allowing for polar angle measurement. Given the space constraints in the collision hall, the coverage is not complete in ϕ.

The main component of the IMU are the Barrel Chambers (BMU). This detector is shaped as two contiguous barrels of drift chambers located on the outer radius of the toroids. These chambers expand the muon coverage of CDF up to $|\eta| \approx 1.5$, but only cover the upper 270° in azimuth.

Sets of scintillators were also installed for trigger confirmation and spurious signal rejection. The central muon scintillator upgrade, CSP, are counters installed on the outer surface of the

CMP chambers. Two layers of scintillators are mounted on the internal and external sides of the CMX, the so-called central muon extension scintillator, CSX. Finally, the IMU incorporates two scintillator systems: the barrel scintillator upgrade, BSU, and the Toroid Scintillator Upgrade, TSU. The BSU detector is made of rectangular scintillators mounted on the outside of the BMU chambers and with the same azimuthal coverage. The TSU detector is made of trapezoidal scintillators mounted on the inner face of the toroid and covering 2π in azimuth.

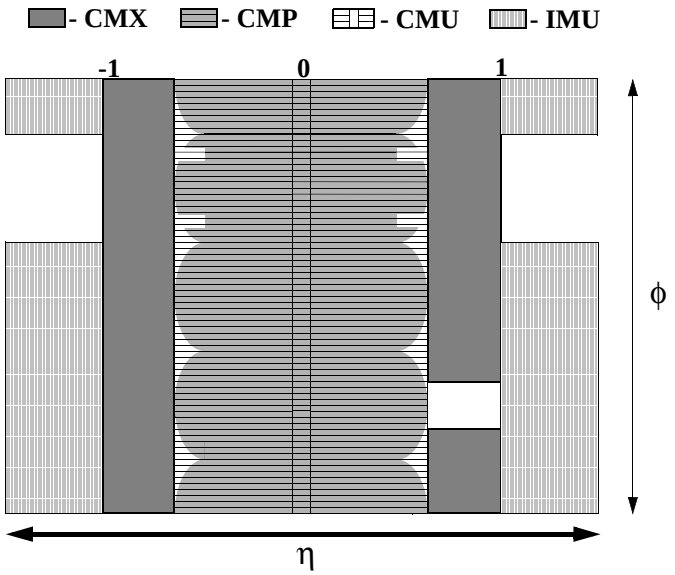

Figure 3.10: η-ϕ coverage of the different muon subsystems: central muon detector (CMU), central muon upgrade detector (CMP), central muon extension (CMX), and the intermediate muon detector (IMU). The IMU includes the barrel chambers (BMU) and some scintillator detectors.

3.3 Luminosity Measurement

The Cherenkov Luminosity Counter (CLC) [79] was designed for the Tevatron Run II in order to achieve a precision measurement of the instantaneous luminosity up to $\approx 4{\cdot}10^{32}\ \mathrm{cm}^{-2}\mathrm{s}^{-1}$ and to cope with the 132 ns bunch-spacing that was originally envisioned.

3.3.1 CLC detector

In CDF, the beam luminosity is determined using gas Čerenkov counters located in the pseudorapidity region $3.7 < |\eta| < 4.7$, which measure the average number of inelastic interaction

per bunch crossing. Each module consists of 48 thin, gas-filled, Čerenkov counters. The counters are arranged around the beam pipe in three concentric layers, with 16 counters each, and pointing to the center of the interaction region. The cones in the two outer layers are about 180 cm long and the inner layer counters, closer to the beam pipe, have a length of 110 cm. The Čerenkov light is detected with photomultiplier tubes located at the end of the tubes, figure 3.11.

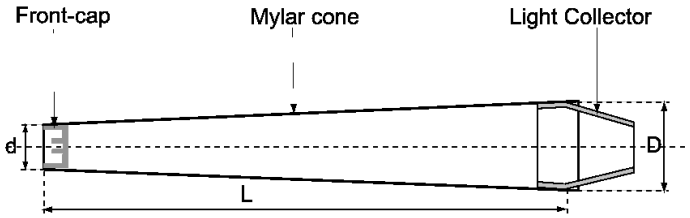

Figure 3.11: Schematic drawing of a cone of the Čerenkov luminosity counters, CLC. An aluminum light collector directs the light reflected in the mylar cone to the photomultiplier, PMT, attached at the end of the tube.

3.3.2 Measurement of the Luminosity

The average number of primary interactions, μ, is related to the instantaneous luminosity, $\mathcal{L}$, by the expression:

$$\mu \cdot f_{bc} = \sigma_{tot} \cdot \mathcal{L} \, , \tag{3.3}$$

where f_{bc} is the bunch crossings frequency at Tevatron, on average 1.7 MHz for 36×36 bunch operations, and σ_{tot} is the total $p\bar{p}$ cross section.

Since the CLC is not sensitive at all to the elastic component of the $p\bar{p}$ scattering, the equation 3.3 can be rewritten using the inelastic cross section, σ_{in}, as

$$\mathcal{L} = \frac{\mu \cdot f_{bc}}{\sigma_{in}}, \tag{3.4}$$

where now μ is the average number of inelastic $p\bar{p}$ interactions. The method used in CDF for the luminosity measurement is based on the counting of empty crossings [80]. This method determines μ by measuring the first bin of the distribution which corresponds to the probability of having zero inelastic interactions, P_0, through the relation:

$$P_0(\mu) = e^{-\mu}, \tag{3.5}$$

which is correct if the acceptance of the detector and its efficiency were 100%. Given the limited extent of this statement, there are some selection criteria, α, to define an "interaction". An "interaction" is defined as a $p\bar{p}$ crossing with hits above a fixed threshold on both sides of the CLC detector. Following this, an empty crossing is defined as a $p\bar{p}$ crossing with no interactions. Given these selection criteria, the experimental quantity P_0, called $P_0^{exp}\{\alpha\}$, is related to μ as:

$$P_0^{exp}\{\mu;\alpha\} = (e^{\epsilon_\omega \cdot \mu} + e^{-\epsilon_e \cdot \mu} - 1) \cdot e^{-(1-\epsilon_0)\cdot\mu}, \tag{3.6}$$

where the acceptances ϵ_0 and $\epsilon_{\omega/e}$ are, respectively, the probability to have no hits in the combined east and west CLC modules and the probability to have at least one hit exclusively in west/east CLC module. The evaluation of these parameters is based on Monte Carlo simulations, and typical values are $\epsilon_0 = 0.07$ and $\epsilon_{\omega/e} = 0.12$.

To obtain the luminosity measurement using the equation 3.4, the value of σ_{in} is still needed. At the beginning of Run II, an extrapolation to 2 TeV of the value measured at $\sqrt{s} = 1.8$ TeV by CDF [81] was used. The cross section would be $\sigma_{in} = 60.4$ mb. To facilitate the comparison of CDF and DØ cross section measurements in Run II, the collaborations agreed to use a common inelastic cross section [82], $\sigma_{in} = 59.3$ mb that is about 1.9% smaller than previous value. Since CDF never modified the actual luminosity value used internally within the collaboration, the CDF quoted luminosity is multiplied offline by a factor of 1.019.

Different sources of uncertainties have been taken into account to evaluate the systematic uncertainties on the luminosity measurement [83]. The dominated contributions are related to the detector simulation and the event generator used, and have been evaluated to be about 3%. The total systematic uncertainty in the CLC luminosity measurements is 5.8%, which includes uncertainties on the measurement, 4.2%, and on the inelastic cross section value, 4%.

3.4 Trigger and Data Acquisition

The average interaction rate at the Tevatron is 1.7 MHz for 36×36 bunches. In fact, the actual interaction rate is higher because the bunches circulate in three trains of 12 bunches in each group spaced 396 ns which leads to a crossing rate of 2.53 MHz. The interaction rate is orders of magnitude higher than the maximum rate that the data acquisition system can handle. Furthermore, the majority of collisions are not of interest. This leads to implementation of a trigger system that preselects events online and decides if the corresponding event information is written to tape or discarded.

The CDF trigger system consists of three trigger levels, see figure 3.12 and figure 3.13. The first two levels are hardware based, while the third one consists on a processor farm. The decisions taken by the system are based on increasingly more complex event information. The two hardware levels are monitored and controlled by the Trigger Supervisor Interface, TSI, which distributes signals from the different sections of the trigger and DAQ system, a global clock and bunch crossing signal.

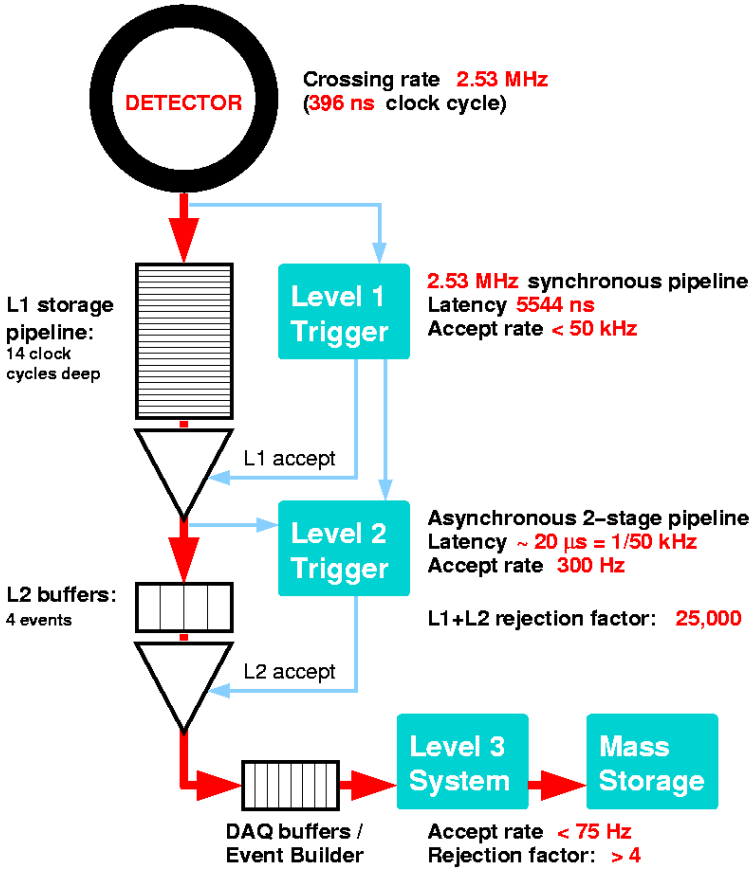

Figure 3.12: Block diagram showing the global trigger and DAQ systems at CDF II.

3.4.1 Level 1 Trigger

The Level 1 trigger is a synchronous system that reads events and takes a decision every beam crossing. The depth of the Level 1 decision pipeline is approximately 4 μs, L1 latency. The L1 buffer must be at least as deep as this processing pipeline or the data associated with a particular Level 1 decision would be lost before the decision is made. The L1 buffer is 14 crossings deep (5544 ns at 396 ns bunch spacing) to provide a margin for unanticipated increases in L1 latency. The Level 1 reduces the event rates from 2.53 MHz to less than 50 kHz.

The Level 1 hardware consists of three parallel processing streams which feed inputs of the Global Level 1 decision unit. One stream finds calorimeter based objects, L1 CAL, another finds muons, L1 MUON, while the third one finds tracks in the COT, L1 TRACK. Since the muons and the electrons (calorimeter-based) require the presence of a track pointing at the corresponding outer detector element, the tracks must be sent to the calorimeter and muon streams as well as the track only stream.

- The L1 CAL calorimeter trigger is employed to detect electrons, photons, jets, total transverse energy and missing transverse energy, $\not\!\!E_T$. The calorimeter triggers are divided into two types: object triggers (electron, photons and jets) and global triggers ($\sum E_T$ and $\not\!\!E_T$). The calorimeter towers are summed into trigger towers of 15^o in ϕ and by approximately 0.2 in η. Therefore, the calorimeter is divided in 24 x 24 towers in $\eta \times \phi$ space [84]. The object triggers are formed by applying thresholds to individual calorimeter trigger towers, while thresholds for the global triggers are applied after summing energies from all towers.

- The L1 TRACK trigger is designed to reconstruct tracks on the COT. An eXtremely Fast Tracker, XFT, [85] uses hits from 4 axial layers of the COT to find tracks with a p_T greater than some threshold, $\sim$ 2 GeV/c. The resulting track list is sent to the extrapolation box, XTRP,[86] that distributes the tracks to the Level 1 and Level 2 trigger subsystems.

- L1 MUON system uses muon primitives, generated from various muon detector elements, and XFT tracks extrapolated to the muon chambers by the XTRP to form muon trigger objects. For the scintillators of the muon system, the primitives are derived from single hits or coincidences of hits. In the case of the wire chambers, the primitives are obtained from patterns of hits on projective wire with the requirement that the difference in the arrival times of signals be less than a given threshold. This maximum allowed time difference imposes a minimum p_T requirement for hits from single tracks.

Finally, the Global Level 1 makes the L1 trigger decision based on the objects of interest found by the different Level 1 processes. Different sets of Level 1 conditions are assigned to the L1 trigger bits. If these conditions are met, the bit is set to true. All this information is later handled by the TSI and transfered to the other trigger levels, and eventually, to tape.

3.4.2 Level 2 Trigger

The Level 2 trigger is an asynchronous system which processes events that have received a L1 accept in FIFO (First In - First Out) manner. It is structured as a two-stage pipeline with data buffering at the input of each stage. The first stage is based on a dedicated hardware processor which assembles information from a particular section of the detector. The second stage consists of a programmable processors operating on lists of objects generated by the first stage. Each of the L2 stages is expected to take approximately 10 μs giving a latency of approximately 20 μs. The L2 buffers provide a storage of four events. After the Level 2, the event rate is reduced to about 400-1000 Hz.

In addition of the trigger primitives generated for Level 1, data for the Level 2 come from the shower maximum strip chambers in the central calorimeter and the $r \times \phi$ strips of the SVX II. There are three hardware systems generating primitives at Level 2: Level 2 cluster finder, L2CAL, shower maximum strip chambers in the central calorimeter, XCES, and the Silicon Vertex Tracker (SVT).

- The L2CAL hardware carries out the hardware cluster finder functions. It receives trigger tower energies from the L1 CAL and applies seed and "shoulder" thresholds for cluster finding. It is basically designed for triggering on jets, but specific reconstruction of clusters for triggering on electrons, taus, and photons is also performed.

- The shower maximum detector provides a much better spacial resolution than a calorimeter tower. The XCES boards perform sum of the energy on groups of four adjacent CES wires and compare them to a threshold (around 4 GeV). This information is matched to XFT tracks to generate a Level 2 trigger. This trigger hardware provides a significant reduction in combinatorial background for electrons and photons.

- Silicon Vertex Tracker, SVT, [87] uses hits from the $r \times \phi$ strips of the SVX II and tracks from the XFT to find tracks in SVX II. SVT improves on the XFT resolution for ϕ and p_T and adds a measurement of the track impact parameter, d_0. Hereby the efficiency and

resolution are comparable to those of the offline track reconstruction. The SVT enables triggering on displaced tracks, that have a large d_0.

When the objects reconstructed by the Level 2 processors meet the conditions stated in the trigger table for the Level 2, the event is assigned the corresponding Level 2 trigger bit, provided that the corresponding Level 1 bit is already set. At that moment, the TSI sends the event to the Level 3 farm.

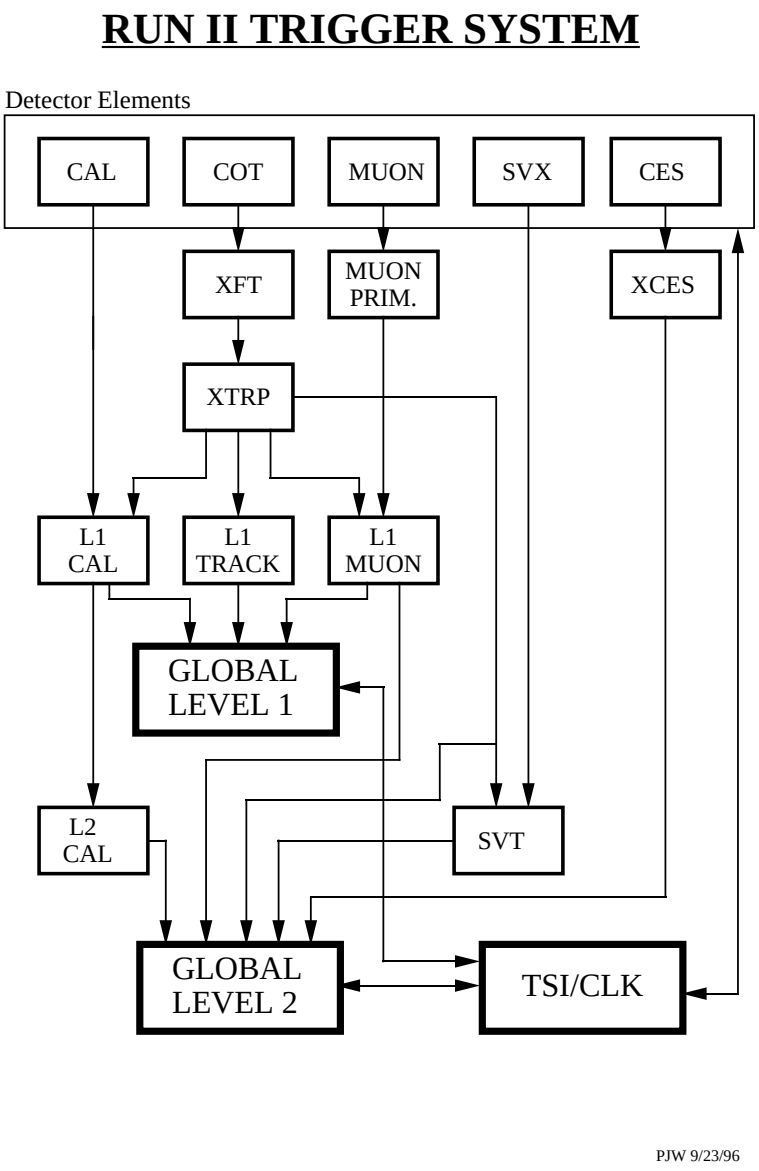

Figure 3.13: Block diagram showing the Level 1 and Level 2 trigger systems.

3.4.3 Level 3 Trigger

After an event is accepted at Level 2, it has to be read out completely. This operation involves collecting data from over a couple of hundreds of VME Readout Buffers (VRBs). The Event Builder assembles the event from pieces of data from the L2 system into complete events. It is divided into 16 sub-farms, each consisting of 12 to 16 processor nodes. Once the event is built, it is sent to one node in the Level 3 farm. The Level 3 trigger reconstructs the event following given algorithms. These algorithms take advantage of the full detector information and improved resolution not available to the lower trigger levels. This includes a full 3-dimensional track reconstruction and tight matching of tracks to calorimeter and muon-system information. Events that satisfy the Level 3 trigger requirements are then transfered onward to the Consumer Server/Data Logger (CSL) system for storage first on disk and later on tape. The average processing time per event in Level 3 is on the order of a few seconds. The Level 3 leads to a further reduction in the output rate, roughly 50 Hz.

A set of requirements that an event has to fulfill at Level 1, Level 2 and Level 3 constitutes a trigger path. The CDF II trigger system implements about 200 trigger paths. An event will be accepted if it passes the requirements of any one of these paths and, depending of the trigger path, it will be stored in a trigger dataset. A complete description of the different datasets at CDF Run II can be found in [88].

Another important feature of the trigger system of CDF is that Level 1 and Level 2 accepts can be pre-scaled. This means that only a fraction of the events that fulfill the trigger requirements are actually accepted. Even if this implies loosing potentially useful events, it becomes necessary at high luminosity. Given the continuous improving performance of the Tevatron, pre-scaling trigger has become common practice in the last years. Moreover, the trigger system allows for dynamic pre-scaling of trigger accepts, meaning that the scaling factor varies with the instantaneous luminosity, so the output bandwidth is maximally utilized.

3.5 Level 2 Trigger Upgrade for High Luminosity

The Level 2 trigger has worked well for Run II at low luminosity. However, as the Tevatron instantaneous luminosity increases, the limitation due to the simple algorithms used, starts to become clear. As a result, some of the most important jet and $\not\!\!E_T$ related triggers have large growth terms in cross section and completely dominate the Level 2 accept bandwidth at the high luminosity regimes ($\sim 300 \cdot 10^{30}\ \mathrm{cm}^{-2}\mathrm{s}^{-1}$).

For this reason, two major trigger upgrades were implemented during 2007, the Level 2 XFT stereo upgrade and the Level 2 calorimer upgrade.

3.5.1 Level 2 XFT Stereo Upgrade

The XFT Stereo upgrade provides many benefits over the purely axial triggering system used previously. One of the achievements of this project is to reduce the rate of fake tracks in many triggers. Fake rates increase very rapidly with luminosity, much faster than the real track rates. By removing as many of the fake tracks as possible at trigger level, it is possible to keep these triggers, without a pre-scale, up to much higher instantaneous luminosities. The Level 1 path is used to confirm the existing XFT track, reconstructed with the axial COT layers only, goes through the stereo layers at the expected locations. At Level 2 the segmentation is much finer than at Level 1 allowing a better fake rejection rate and also providing information about the position of the track. In particular it is possible to measure the angle of the track with respect to the beam axis as well as the distance z from the center of the detector along the beam axis and use this information to point the track to other detectors. This 3D tracking opens up several additional capabilities such as trigger level multi-track mass calculations or isolation requirements and z-vertex reconstruction at Level 2.

3.5.2 Level 2 Calorimeter Upgrade

The new Level 2 calorimeter system makes the full calorimeter trigger tower information directly available to the Level 2 decision CPU. The upgraded system allows more sophisticated algorithms to be implemented in software; both Level 2 jets and $\not\!\!E_T$ can be made nearly equivalent to offline quality, thus significantly improving the purity as well as the efficiency of the jet and $\not\!\!E_T$ related triggers. The jet triggers are improved by using a cone algorithm in the Level 2 CPU for jet cluster finding. The jet algorithm is similar to JetClu (which is used to reconstruct Level 3 and offline jets) except that the clustering is done in a single iteration, in order to save processing time.

Chapter 4

Event Reconstruction

To perform a data analysis, the information obtained from the detector have to be process in order to reconstruct observables. This reconstruction implies mathematical algorithms and definitions hardly related with the detector itself.

The analyses described in this thesis are based on jets, $\not\!\!E_T$, and in an indirect way, electrons and muons. All these objects are briefly explained in this Chapter.

4.1 Track and Primary Vertex Reconstruction

The trajectories of charged particles are found (in a first approximation) as a series of segments in the axial superlayers of the COT. Two complementary algorithms associate the segments lying on a common circle to define an axial track. Segments in the stereo layers are associated with the axial tracks to reconstruct 3D tracks. For muons and electrons used in this analysis, COT tracks are required to have at least 3 axial and 2 stereo segments with at least 5 hits per superlayer. The efficiency for finding isolated high momentum COT tracks in the COT fiducial volume with $p_T > 10$ GeV/c is measured using electrons from $W^{\pm} \rightarrow e^{\pm}\nu$ events and is found to be (98.3 $\pm$ 0.1)%. Silicon hit information is added to reconstructed COT tracks using an "outside-in" tracking algorithm. The COT tracks are extrapolated to the silicon detector and the track is refit using the information from the silicon measurements. The initial track parameters provide a width for a search region in a given layer. For each candidate hit in that layer, the track is refit and used to define the search region into the next layer. The search uses the two best candidate hits in each layer to generate a small tree of final track candidates, and the one with the best fit χ^2 is selected. The efficiency to associate at least three silicon hits with

an isolated COT track is found to be (91 $\pm$ 1)%.

The primary vertex location for a given event is found by fitting well-measured tracks to a common point of origin. At high luminosities, more than one collision can occur on a given bunch crossing. For a luminosity of $\sim 10^{32}$ cm $^{-2}$s^{-1}, there are $\sim$2.3 interactions per bunch crossing. The luminous region is long, with σ_z = 29 cm; therefore the primary vertices of each collision are typically separate in z. The first estimate of the primary vertices (x_V, y_V, z_V) is binned in the z coordinate, and the z position of each vertex is then calculated from the weighted average of the z coordinate of all tracks within 1 cm of the first iteration vertex, with a typical resolution of 100 μm. The primary vertex is determined event by event by an iterative algorithm which uses tracks around a seed vertex, defined as above, to form a new vertex. The χ^2 for all tracks relative to the new vertex is calculated, tracks with bad χ^2 are removed, and the cycle is repeated until all tracks have a good χ^2. The locus of all primary vertices defines the beamline, the position of the luminous region of the beam-beam collisions through the detector. A linear fit to (x_V, y_V) vs. z_V yields the beamline for each stable running period. The beamline is used as a constraint to refine the knowledge of the primary vertex in a given event. The transverse beam cross section is circular, with a rms width of $\approx$ 30 μm at $z = 0$, rising to $\approx$ 50 - 60 μm at $|z|$ = 40 cm. The beam is not necessarily parallel nor centered in the detector.

4.2 Lepton Identification

No leptons are expected in none of the signals under study in this thesis. Therefore, we reject leptons during the optimization process. We however require leptons in one control region to define orthogonal conditions to the signal region.

The leptons required in the analyses are electrons reconstructed in the central calorimeter and muons identified as isolated high-p_T tracks.

4.2.1 Electron Reconstruction

Electrons are measured in the Electromagnetic Calorimeters. Incident electrons induce showers across multiple calorimeter towers. The energy of the showers appears in clusters in the $\eta - \phi$ coordinate system. The clustering algorithm looks for EM-objects in the CEM. It starts by creating an E_T-ordered list of possible seed towers that are in the fiducial region and have $E_T^{em} > 2$ GeV. Then towers within the fiducial regions (including seeds) adjacent to the available

highest E_T seed are checked. They may belong to the cluster if they are in the same detector as the seed, and have not been already used. Clusters in CEM can grow only away by 1 physical tower from the seed. A cluster is found if the total EM-energy passes $E_T^{em} > 2$ GeV (default), and $E_T^{had}/E_T^{em} < 0.125$, where E_T^{had} is the hadronic energy within the seed tower in CEM. After all clusters are found, tracks from the default collection are matched with them computing the cluster center with the energy weighted average of the CES coordinates of the cluster towers. The central electron candidates must have a matching COT track.

In our selection, we apply additional cuts listed in Table 4.1 for discriminating electrons with at least 10 GeV transverse energy from electron faking objects such as photons, isolated charged hadrons, and jets.

CEM Electron selection	Cut
Transverse energy	$E_T \geqslant 10$ GeV/c
COT axial segments	Three or more (with 5 hits each)
COT stereo segments	Two or more (with 5 hits each)
Corrected d_0	$\lvert d_{0,corr}\rvert \leqslant 0.02$ cm (with Si hits)
	$\lvert d_{0,corr}\rvert \leqslant 0.2$ cm (without Si hits)
Corrected z_0	< 3 cm
E over P	$E/p \leqslant 2$ (or track $p_T \geqslant 50$ GeV/c)
CES fiducial	Yes
HAD over EM energy ratio	$E_{HAD}/E_{EM} \leqslant 0.055 + 0.00045 * E_{TOT}$
Track L_{shr}	$L_{shr} \leqslant 0.2$ (if valid value)
CES Dz	$\lvert Dz\rvert \leqslant 3$ cm
CES Dx	$-3 \leqslant Q \times Dx \leqslant 1.5$ (cm)
CES χ^2 (strip)	$\chi^2 \leqslant 10$
Isolation	Iso(0.4)$\leqslant 0.1 \times p_T$ (for $p_T \geqslant 20$ GeV/c)
	Iso(0.4)$\leqslant 2$ GeV/c (for $p_T < 20$ GeV/c)

Table 4.1: Central electrons identification cuts.

The ratios between the hadronic and the electromagnetic cluster energies E_{HAD}/E_{EM} and between the cluster energy and the track momentum E/p are required to be consistent with an electron's energy deposition in the calorimeters. The cluster is further required to be isolated,

the isolation being defined as the ratio of the additional transverse energy in a cone of radius $R = \sqrt{(\Delta\phi)^2 + (\Delta\eta)^2} = 0.4$ around the cluster to the transverse energy of the cluster itself.

The position of the electromagnetic shower measured by the CES detector is used to define matching requirements between the extrapolated track and the cluster in the CES x and z local coordinates. In particular, a charge dependent cut in the x position is applied to take into account the different flow of energy deposited by bremsstrahlung photons emitted by an electron or a positron. In addition, the CES provides electron identification through the observed shower shape. The CES shower shape is fitted in the z view to the distribution expected for an electron, and the chisquare probability for the fit, χ^2_{strip}, is used as a cut on the shower profile. Finally, the sharing of energy between adjacent calorimeter towers is quantified by the lateral shower profile L_{shr}, which measures how close the energy distribution in the CEM towers adjacent to the cluster seed is to the electron hypothesis.

4.2.2 Isolated Tracks

Muons are detected by the muon-system placed in the outermost layer of the CDF detector because of the highly penetrating nature of muons. Hits in the muon detectors are linked together to form track segments called stubs. These track segments are matched to extrapolated COT tracks with at least $p_T > 15$ GeV and energy deposition in the calorimeter that is consistent with minimum ionizing particles. Isolated tracks with $p_T > 15$ GeV that do not have associated stubs are also considered muon candidates (called *stubless muons*).

Since all muons reconstructed at CDF have associated isolated tracks, it makes sense to loosen up the muon selection to the level of *stubless muons* for the analyses purposes. An isolated track veto will also reject events with hadronically decaying high-p_T tau leptons. The isolated track identification cuts are listed in Table 4.2.

The COT track must have $p_T \geq 10\ \ \mathrm{GeV}/c$, and at least 3 axial and 2 stereo segments with a minimum of 5 hits per segment. The distance of closest approach of the track to the beamline in the transverse plane, d_0, must be small in order to select prompt muons (coming from the interaction primary vertex) and reject cosmics and in-flight decays. The energy deposition in the EM and HAD calorimeters, E_{EM} and E_{HAD}, must be small as expected for the passage of a minimum ionizing particle. Isolation is defined as the ratio between any additional transverse energy in a cone of radius $R = 0.4$ around the track direction and the muon p_T, and it is required to be smaller than 0.1.

Loose Muon selection	Cut
Transverse momentum	$p_T \geqslant 10$ GeV/c
COT axial segments	Two or more (with 5 hits each)
COT stereo segments	One or more (with 5 hits each)
COT χ^2	χ^2/ndof$\leqslant 3$
Corrected d_0	$\lvert d_{0,corr}\rvert \leqslant 0.02$ cm (with Si hits)
	$\lvert d_{0,corr}\rvert \leqslant 0.2$ cm (without Si hits)
Corrected z_0	< 3 cm
EM energy	$E_{EM} \leqslant 2$ GeV/c
HAD energy	$E_{HAD} \leqslant 6$ GeV/c
Total CAL Energy	$E_{EM} + E_{HAD} \geqslant 0.1$ GeV/c
Isolation	Iso(0.4)$\leqslant 0.1 \times p_T$ (for $p_T \geqslant 20$ GeV/c)
	Iso(0.4)$\leqslant 2$ GeV/c (for $p_T < 20$ GeV/c)

Table 4.2: Stubless muons identification cuts.

4.3 Jet Reconstruction

Collision events that trigger the detector contain one or more hard scattering processes from parton interactions. We are interested in detecting the products of these hard interactions. Light particles such as electrons and muons are stable or have long lifetime and reach the subdetectors designed for their identification. Quarks and gluons, however, participate in more complex processes. First, they undergo a process called fragmentation where they create partons via a cascade of gluon emissions and decays. The fragmentation continues until the momentum square of the partons is at the order of the infrared cut-off scale. Partons then form colorless hadrons in a process called hadronization. The non-stable hadrons decay to stable particles which reach the detector material. The showers of particles appear as clusters of energy deposited in localized areas of the calorimeter, called jets.

There are several algorithms developed for calorimeter jets. Some algorithms may also incorporate tracking information in searching for charged jets or in measuring their transverse momenta. The jet identification algorithm used in these searches is called JETCLU [89] which relies only on calorimetry. The jets are defined as towers in circular regions of the $\eta - \phi$ plane,

called cones, with radius:

$$R = \sqrt{(\Delta\eta_i)^2 - (\Delta\phi_i)^2} \tag{4.1}$$

where $\Delta\eta_i = \eta_{cent} - \eta_i$ and $\Delta\phi_i = \phi_{cent} - \phi_i$ are differences between the E_T-weighted average of the tower locations (centroid) and the i^{th} tower location in pseudo-rapidity and azimuthal angle. The algorithm starts searching for towers with $E_T > 1$ GeV, where

$$E_T = E_{em} \sin\theta_{em} + E_{had} \sin\theta_{had} \tag{4.2}$$

$\theta_{em}(\theta_{had})$ is the polar angle of the EM(HAD) cell of the tower in the detector coordinate system with origin placed at the highest p_T vertex in the event. Then preclusters are created by grouping adjacent towers within the cone radius proceeding from the highest energy tower to the lowest one. One tower is assigned to only one precluster. In the next step, the centroids of the preclusters are calculated, and new cones are defined including towers with at least 100 MeV. If the centroid of a new cluster changes, the cone is redefined and new towers are added iteratively (but not taken away). When a stable solution is found, overlaps between clusters are removed by either combining or separating contiguous clusters, and jets are defined.

The energy of the jets is corrected [90] for the pseudo-rapidity dependence of the calorimeter response, the calorimeter time dependence, and extra E_T from any multiple interactions.

4.4 Missing Transverse Energy Reconstruction

The presence of undetectable particles in an event is inferred by an imbalance of transverse energy in the detector. The missing transverse energy, $\not\!\!E_T$, is reconstructed entirely based on calorimeter information and defined as the magnitude:

$$\not\!\!E_{Tx} = -\sum_{i=0}^{N_{towers}} E_{T,i} \cos(\phi_i) \tag{4.3}$$

$$\not\!\!E_{Ty} = -\sum_{i=0}^{N_{towers}} E_{T,i} \sin(\phi_i) \tag{4.4}$$

and

$$\not\!\!E_T = \sqrt{\not\!\!E_{T_x}^2 + \not\!\!E_{T_y}^2} \tag{4.5}$$

where $E_{T,i}$ is the transverse energy of the calorimeter tower i calculated with respect to the z coordinate of the event, ϕ_i is its azimuthal angle, and the sum is over all calorimeter towers.

The $\not\!\!E_T$ is corrected by objet participating in the event, in our case jets, in following way:

$$\not\!\!E_{T_x}^{corr} = \not\!\!E_{T_x}^{raw} - \sum_{i=1}^{N_{jets}} (E_x^{corr,i} - E_x^{raw,i}) \tag{4.6}$$

$$\not\!\!E_{T_y}^{corr} = \not\!\!E_{T_y}^{raw} - \sum_{i=1}^{N_{jets}} (E_y^{corr,i} - E_y^{raw,i}) \tag{4.7}$$

since leptons are not expected in the final state, corrections are not applied for electrons or muons.

4.5 Quality Selection Cuts in $\not\!\!E_T$ Analysis

All the CDF II analyses based on the $\not\!\!E_T$ data sample apply a set of quality cuts on the data ("clean-up cuts"). Here is a summary of these cuts organized in three passes:

- Pass 1 requirements
  - At least one central jet ($|\eta| < 0.9$) with $E_T > 10$ GeV ,
  - Event Electromagnetic Fraction (EEMF):

    $$EEMF = \frac{\sum_{j=1}^{N_{jets}} E_T^j \cdot EMF_j}{\sum_{j=1}^{N_{jets}} E_T^j} > 0.1$$

    where EMF_j is the fraction of the jet energy deposited in the electromagnetic calorimeter. Only jets with $E_T^{raw} > 10$ GeV are considered,
  - At least one COT track with $p_T > 0.5$ GeV/c and an axial super layer with six or more hits.

- Pass 2 requirements
  - Event Charge Fraction (ECHF):

$$ECHF = \frac{\sum_{j=1}^{N_{jets}} CHF_j}{N_{jets}} > 0.1$$

    where CHF_j is the jet charge fraction defined as the sum of the p_T of the tracks matched to the jet over the jet ET :

$$CHF_j = \frac{\sum_{j=1}^{N_{tracks}} p_T^{ji}}{E_T^j} > 0.1$$

  - At least one good primary vertex in the event
- Pass 3 requirements
  - The chimney is a hole in the calorimeter at $\phi = (60°; 100°)$ and $\eta = (0.5; 1.0)$ that hosts cryogenic and instrumental connections to the inner detector. Jets that fall into the chimney region are almost certainly mismeasured, therefore we discard any event that has such a jet with $E_T > 10$ GeV .
  - Event primary vertex falls within $z < 60$ cm of the nominal interaction point at the detector center.
  - The beam halo energy usually appears in a row of towers at $\phi = 0$. It was found that the previous selection criteria are suficient to eliminate events with beam halo muons, therefore no further treatment is required.
  - Total calorimeter energy less than 2 TeV.

Chapter 5

Heavy Flavor Tagging

The fact that the majority of background events contain only light quarks in their final states, makes the heavy flavor tagging one of the most powerful tools removing backgrounds. Different algorithms and flavor separators are extensively used in high energy physics analysis.

The specific tagging tools used during the analyses signal optimization processes are explained in this Chapter.

5.1 Secondary Vertex algorithm

The B hadrons in jets coming from b quark fragmentation have an average flight path of about 500 microns, yielding secondary vertices relative to the interaction point. These hadrons travel away from the primary vertex and subsequently decay to hadrons through a cascade of particles. The charged decay products are often reconstructed as displaced tracks. The intersections of these tracks form secondary vertices at the points where the hadrons decay.

The SecVtx algorithm [91] searches for displaced secondary vertices by combining tracks within "taggable" jets (figure 5.1). Jets are taggable if E_T^{raw} >10 GeV, η <2.4, and have at least two *good tracks* [91]. It first combines three or more tracks with looser selection requirements. If that fails, pairs of tracks that pass tighter quality requirements are tested. The displacement of the secondary vertex with respect to the primary vertex in the transverse plane is given by

$$L_{xy} = \vec{d} \cdot \hat{p}_T \tag{5.1}$$

where $\vec{d}$ is the displacement of the secondary vertex and $\hat{p}_T$ is the unit vector of the jet mo-

mentum. Thus L_{xy} is positive if the displacement points along the jet momentum, and negative if it points to the opposite direction. Jets are tagged positively if $L_{xy}/\sigma_{L_{xy}} > 3$ and negatively if $L_{xy}/\sigma_{L_{xy}} < -3$. Negative tags are due to resolution effects in the tagging, and are usually high-p_T light flavor (uds) jets. Similar phenomena are observed in the simulation of positive tags. The positively tagged light flavor jets are called mistags (section 5.2).

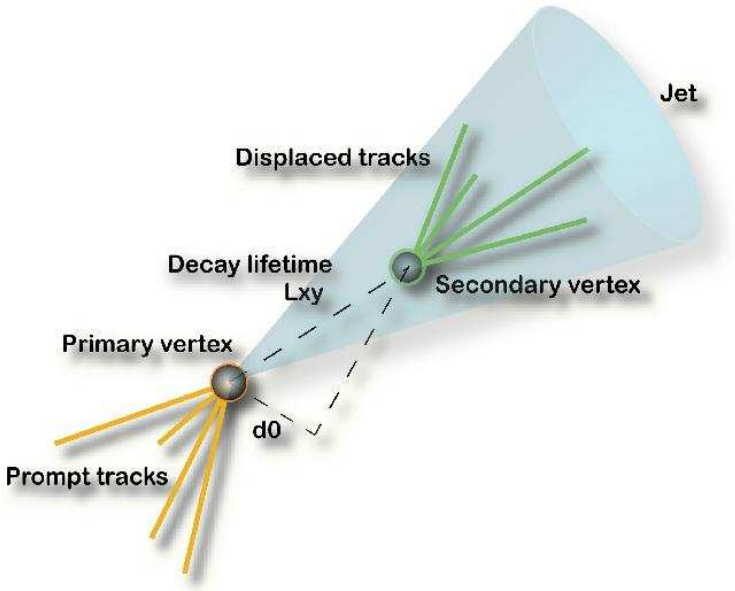

Figure 5.1: Schematic diagram of the secondary vertex heavy flavor tagging.

There are two settings for SecVtx, one with looser and one with tighter track requirements. The loose tagger has higher efficiency for b-jets than the tight, but it also suffers a higher mistag rate. The efficiency for the two settings are shown in figure 5.2 and figure 5.3 as functions of the jet E_T and η. A degradation of track reconstruction efficiency is observed at $|\eta| > 1.1$ outside the COT coverage. The efficiency is defined with respect to taggable jets.

The detector simulation is reported to overestimate the tracking resolution. As a consequence, the tagging efficiency is higher in Monte Carlo than in data. We apply a weighting factor to Monte Carlo events to compensate for this effect.

5.2 Mistag Estimation

The mistags, light-flavor jets falsely tagged as heavy flavor jets, are inseparable companions of any tagging algorithms. The mistag rate is only few per cent depending on the SecVtx's settings

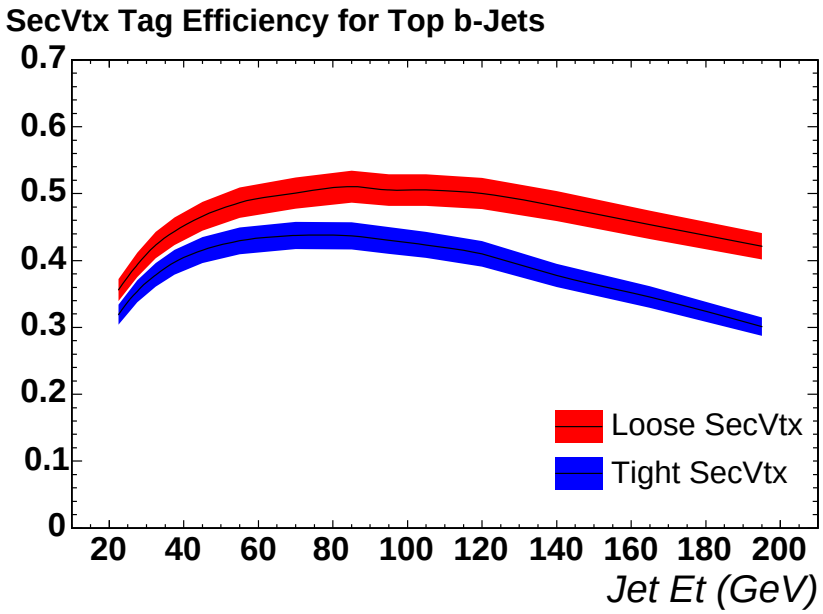

Figure 5.2: Tagging efficiency of the tight and loose SecVtx algorithm as function of the tagged jet E_T in top quark Monte Carlo samples.

(figures 5.4 and 5.5). Although the mistag efficiency is more than an order of magnitude smaller than the heavy flavor tagging efficiency, the large cross section of processes that produce light flavor jets make the mistag background one of the largest in the single-tag data sample.

Mistags are estimated from inclusive jet-sample data by computing a mistag rate [91] ($R^+_{mistags}$). This $R^+_{mistags}$ is a six-dimensional matrix which is parametrized by the jet E_T, $|\eta|$, secondary-vertex track-multiplicity, the number of primary vertices in the event, primary vertex z-position, and the scalar sum of E_T of all jets in the event.

The single mistag is estimated by running on a pre-tag sample with total light and heavy flavor events $N^{pre}_{light} + N^{pre}_{heavy}$. The pre-tag data consists of events that pass all relevant selection cuts without any tag requirements. Double mistags are estimated from the same data after requiring one observed positive tag. This predicts the rate at which the non-tagged jet produces a second tag that is a mistag.

It is generally not known if a positive tag is real or a mistag; therefore, it is not possible to construct a mistag matrix directly from data. Since negative tags are mostly fakes, the construction of the mistag matrix starts by creating a negative tag matrix R^- defined as in equation 5.2 where $N^-_{light} + N^-_{heavy}$ is the number of negative tags in the data.

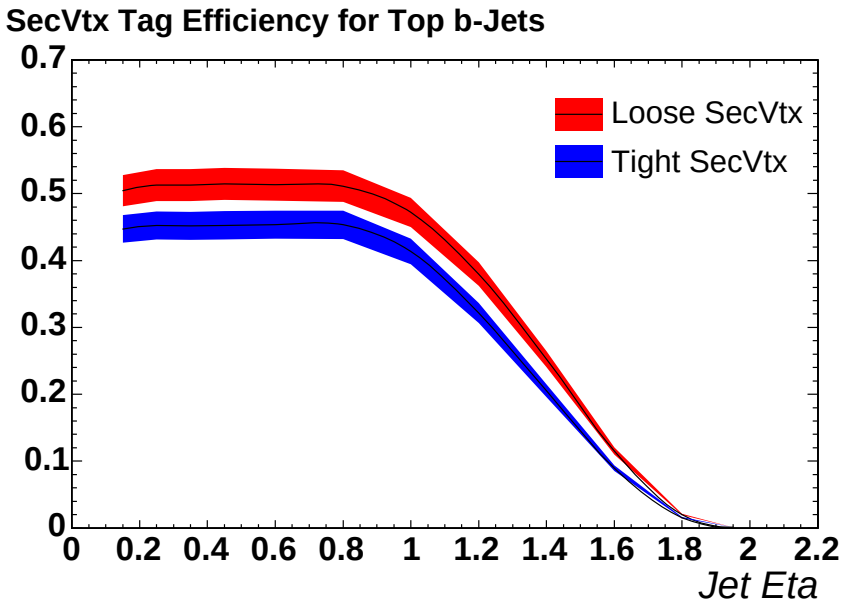

Figure 5.3: Tagging efficiency of the tight and loose SecVtx algorithm as function of the tagged jet η in top quark Monte Carlo samples.

$$R^{-} = \frac{N^{-}_{light} + N^{-}_{heavy}}{N^{pre}_{light} + N^{pre}_{heavy}} \tag{5.2}$$

Negative tags are mainly due to resolution effects in the tracking. The majority of the mistags (light flavor positive tags) are produced similarly. The rest comes from physical sources, for example long-lived particle decays (K_s or Λ) and interactions in the beam-pipe or with the detector material. These processes enhance the mistag rate with respect to the the negative tag rate. We correct for these effects by multiplying the negative tags with an asymmetry factor. Templates of signed tag mass distributions obtained from Monte Carlo simulations of light and heavy flavor jets are fitted to the tag mass observed in the data. The fit provides normalization for the various light and heavy flavor jet productions and fixes the heavy flavor fraction in the simulation. It is not possible to fit both, the negative and the positive tag mass distributions simultaneously, because the Monte Carlo underestimates the fraction of negative tags with respect to the positive ones. In other words, it provides a too optimistic description of the detector resolution. The positive tag excess over the negative tags, however, is physically motivated and expected to be better reproduced by the simulation. It is reasonable to assume that the simulation underestimates the part of the mistag rate which is due to resolution effects as much as the negative tag rate; therefore, the fit is done in two steps. In the first step, the negative templates

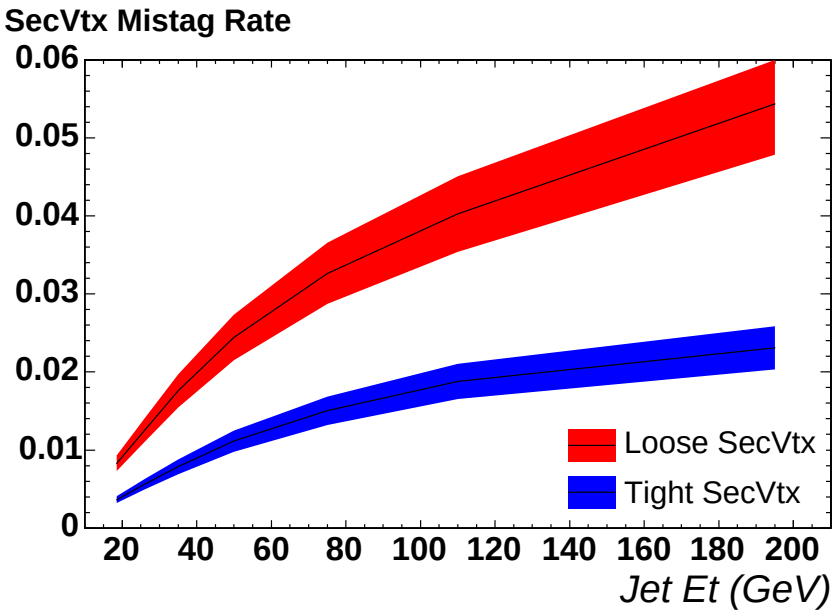

Figure 5.4: Mistag rate of the tight and loose SecVtx algorithm as function of the tagged jet E_T in top quark Monte Carlo samples.

are subtracted from the positive ones in order to get templates for the positive tag excess. The sum of these Monte Carlo templates is fitted to the data, and the correct normalization for the simulations is computed. In the second step, the negative templates are fitted to the data such that the relative fractions of the various flavors are kept the same as measured in the first step. The resulting overall scale factor is called the Negative Scale Factor, and it is assumed to be the same in all Monte Carlo processes regardless of the flavor. The second fit is required to obtain the number of mistags that were subtracted in the first step. The mistag asymmetry is defined as the ratio between the number of positively tagged light flavor jets in the simulation and the sum of all the negative tags:

$$\alpha = \frac{N^{+}_{light}}{N^{-}_{light} + N^{-}_{heavy}} \tag{5.3}$$

where N^{+}_{light} is the number of mistag jets. This definition still contains the heavy flavor contribution to the negative tags. By scaling the negative tags only with this asymmetry factor in order to estimate the actual mistag contribution, one introduces an uncertainty due to possible differences in the flavor compositions between the generic jet sample from which the matrix was produced and the analysis sample in which the matrix is applied. This uncertainty is small for single mistags. However, the first real tag requirement in the double mistag estimation en-

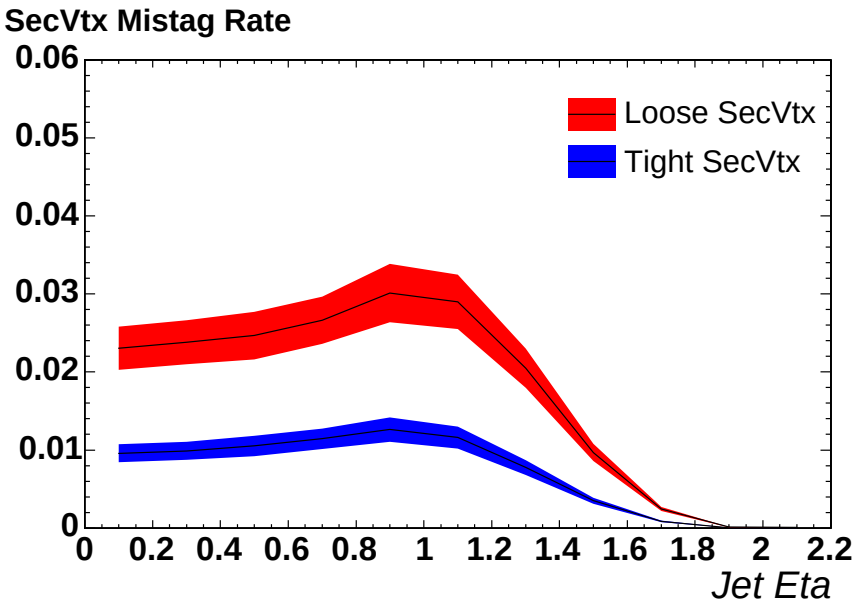

Figure 5.5: Mistag rate of the tight and loose SecVtx algorithm as function of the tagged jet η in top quark Monte Carlo samples.

hances the heavy flavor fraction. In order to get the right prediction in both single and double tags, another scale factor is applied on the top of the asymmetry factor that cancels the heavy flavor contribution in the sample where the mistag matrix was produced:

$$\beta = \frac{N^{pre}_{light} + N^{pre}_{heavy}}{N^{pre}_{light}} \tag{5.4}$$

Thus the elements of the mistag matrix product $\alpha\beta R^{-}$

$$R^{+} = \alpha \times \beta \times R^{-} = \frac{N^{+}_{light}}{N^{pre}_{light}} \tag{5.5}$$

Consequently, this operator is no longer applicable on the entire pre-tag sample. The heavy flavor contribution should be removed from the pre-tag data before applying the matrix. This is done indirectly by applying the matrix on the heavy flavor simulation and subtracting the result from the total prediction obtained in the data. This correction is often not significant with respect to the systematic uncertainties that are generally considered in this analysis. The $t\bar{t}$ process, for example, is corrected by 5% in the single tagged and 8% in the double tagged events.

5.3 Charm Hadron Analysis Oriented Separator

The **C**harm **H**adron **A**nalysis **O**riented **S**eparator (CHAOS) is used to determine whether a tagged jet has been produced from the hadronization process of a light quark, falsely tagged as a heavy flavor jet, a b quark, or a c quark. Depending on the flavor of the original parton, the tagged jet and its secondary vertex have different characteristics, mainly related to the tracking. Using properties of the tracks forming the secondary vertex and the tracks of the jets within a neural network, CHAOS allows to enhance the jet selection with a desired flavor, in particular c jets.

CHAOS is a neural network based on SNNS v4.3 [92]. The structure includes three layers. One input layer with 22 nodes plus one bias node, one hidden layer with 22 nodes, and one output layer with two nodes producing a two-dimensional output. The neural network makes use of 22 variables, mainly related to tagging properties of the jets. These variables, listed in Table 5.1, were carefully chosen to be well reproduced by the simulation, and to have a stable behavior in different samples avoiding dependences with the jet kinematics. All of them are intrinsically related to the applied tagging algorithm, in this case the SecVtx algorithm.

CHAOS input variables	
Mass of the vertex	Average $\|d_0\|$ of good tracks
Charge of the vertex	Average $\|d_0$ significance$\|$ of good tracks
L_{xy} significance	Fraction of good tracks with $\|d_0$ significance$\|$ >1
$\frac{Number\ of\ pass{-}1\ tracks}{Number\ of\ good\ tracks}$	Fraction of good tracks with $\|d_0$ significance$\|$ >3
$\frac{Number\ of\ vertex's\ tracks}{Number\ of\ good\ tracks}$	Fraction of good tracks with $\|d_0$ significance$\|$ >5
$\frac{\sum p_T(good\ tracks)}{E_T}$, where E_T is the jet E_T	$\frac{P_T}{E_T}$, where P_T is the P_T of the secondary vertex
$z_t = \frac{\sum p_T(pass{-}1\ tracks)}{\sum p_T(good\ tracks)}$	Fraction of vertex p_T in the leading track
$r_{vtx} = \frac{p_T\ of\ the\ vertex}{\sum p_T(good\ tracks)}$	Fraction of vertex p_T in the second leading track
Signed d_0 of the leading vertex track	Signed d_0 significance of the leading vertex track
Signed d_0 of the second leading vertex track	Signed d_0 significance of the second leading vertex track
ϕ_{jet}	η_{jet}

Table 5.1: List of input variables used in CHAOS.

The neural network is trained with three pure flavor samples extracted from a $W+$ jet inclusive sample generated with PYTHIA [62] event generator. The samples are extracted by selecting events with at least one tagged jet, requiring loose SecVtx, where the tagged jet comes from a b quark, c quark, $light$ quark, or a τ lepton falsely tagged as heavy flavor jet.

The two-dimensional output structure permits to separate tree different targets during the same training process. The output is distributed in a plane within intervals between 0 and 1. Events with tagged jets from b quarks are targeted to (1,0), jets from c quarks to (1,1), and jets from $light$ quarks or τ leptons to (0,1). The two-dimensional output is shown in figure 5.6 when CHAOS is applied to the three flavor samples used for the training. In an analysis context, the CHAOS application has as purpose the event selection, enhancing the sample with a defined jet flavor, in particular c jets. An easy way to select c jets is to apply a cut on the sum of the one-dimensional outputs. The sum of outputs is a discriminant that separates c jets from the rest of the tagged jets. Figure 5.7 shows the two CHAOS outputs and their sum.

The cut applied in the search for scalar top (Chapter 7) to select c jets, cutting on 1.65 in sum of the CHAOS outputs, is shown as an arrow in figure 5.8. This cut is used to compute the flavor efficiency and the scale factor discussed in the next section 5.4.

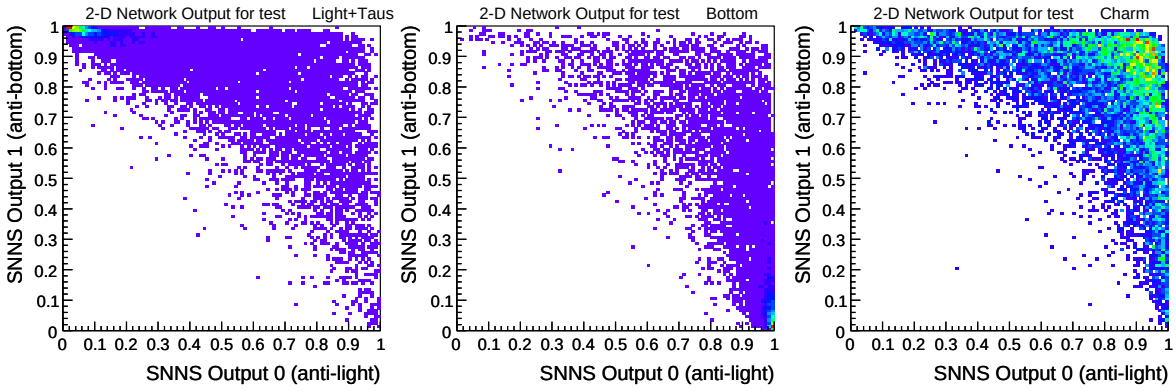

Figure 5.6: Chaos output in 2-D for $light + \tau$ jets (left), b jets (center), and c jets (right) applying the NN to the samples used for training.

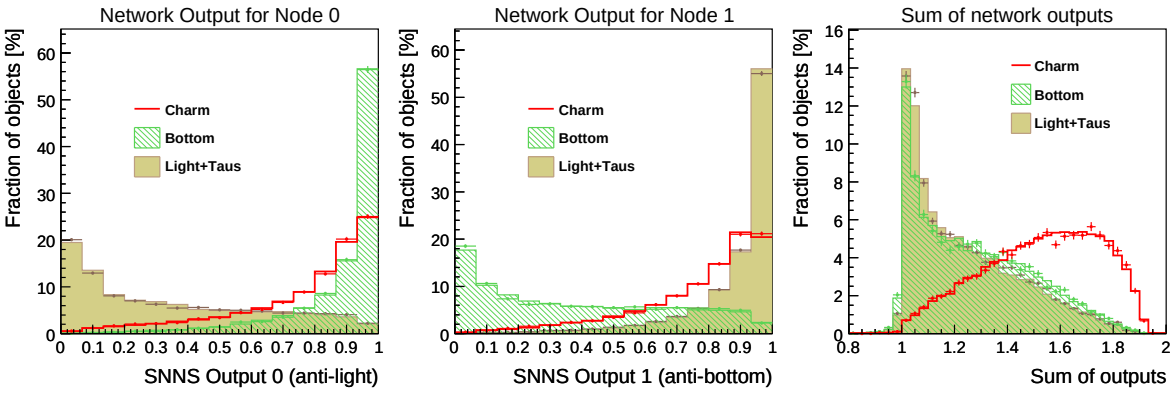

Figure 5.7: Chaos outputs in 1-D. Output-0 distinguishing $light + \tau$ from b and c jets (left), output-1 distinguishing b from $light + \tau$ and c jets (center), and the sum of both (right) applying the NN to the samples used for training including test events (dots).

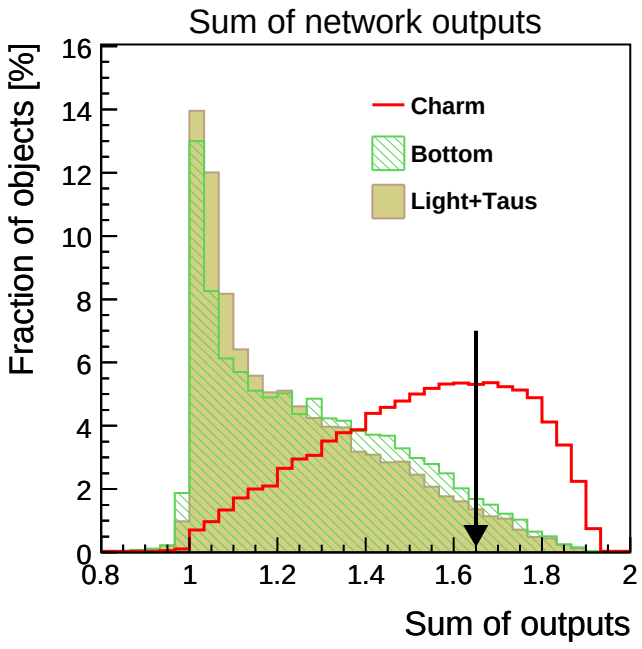

Figure 5.8: Sum of the CHAOS outputs in 1D applying the neural network to the samples used for training. The arrow indicates the cut on 1.65, used in the analysis described in Chapter 7.

5.4 CHAOS Efficiency and Scale Factors

The method used to measure the CHAOS flavor selection efficiency for heavy flavor jets is described in this section. The events used to study this efficiency are dijet events enriched in heavy flavor. A sample triggered on medium p_T inclusive muons which is enriched in semileptonic decays of bottom and charm hadrons is used. The efficiency is also measured for simulated jets by using a Monte Carlo sample. Muons are identified using a selection similar to that described in section 4.2.2, except that they are not required to be isolated and have a lower energy threshold (track $p_T > 8\ \ \mathrm{GeV}/c$). The heavy flavor content of the sample is further enhanced by requiring two jets in the event, a "muon jet", presumed to contain the decay products of a heavy flavor hadron, and an "away jet". The muon requirements are summarized in Table 5.2. The muon jet must have $E_T > 25$ GeV and be within 0.4 of the muon direction in η-ϕ space. The away jet is required to have $E_T > 25$ GeV, and it must be approximately back-to-back with the muon jet ($\Delta\phi_{\mu-j} > 2$ rad).

Muon selection	Cut
CMU stub	$\lvert dx\rvert \leqslant 7\mathrm{cm}$ or ($\mathrm{p_T} < 20\ \mathrm{GeV/c}$ and $\chi^2 \leqslant 9$)
CMP stub	$\lvert dx\rvert \leqslant 5\mathrm{cm}$ or ($\mathrm{p_T} < 20\ \mathrm{GeV/c}$ and $\chi^2 \leqslant 9$)
Transverse momentum	$p_T \geqslant 8\ \mathrm{GeV}/c$
Corrected z_0	$\leqslant 3\mathrm{cm}$
COT axial segments	Two or more (with 5 hits each)
COT stereo segments	One or more (with 5 hits each)
COT χ^2	χ^2/ndof$\leqslant 3$

Table 5.2: Required muon cuts to define a "muon jet".

The fraction of b and c away jets is obtained fitting flavor templates, extracted from a HF multijet MC sample, to the mass of the vertex distribution. The efficiency of the CHAOS cut on 1.65 (as shows figure 5.8) is computed fitting the flavor templates to the data distribution, before and after the cut, as shown in figure 5.9. The efficiency obtained in this way is defined as the central value. The error on this estimation is computed repeating the procedure using flavor templates extracted from a W+jet MC sample.

The efficiencies to select a c or b tagged jet in data are summarized in Table 5.3 for a CHAOS cut on 1.65. The ratio of data efficiency to Monte Carlo simulation efficiency provides the scale

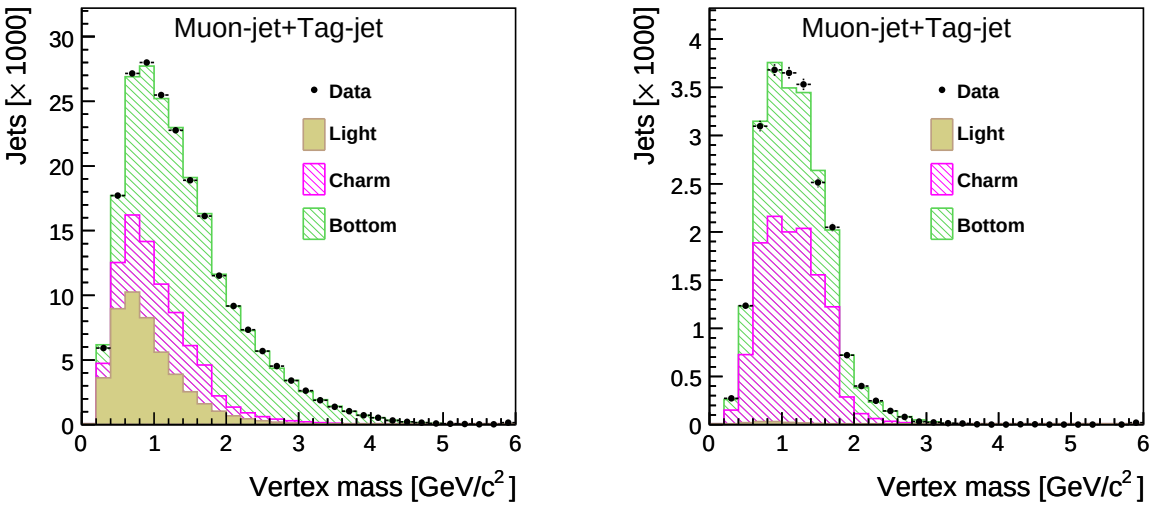

Figure 5.9: Vertex mass distributions in the medium-P_T muon sample with fitted flavour templates from a HF multijet sample, before (left) and after (right) the cut on CHAOS output at 1.65.

factor (SF_{CHAOS}), that is used to correct the MC-based predictions to match the efficiency as measured in data.

	c jets	b jets
Eff. (Data)	0.346 ± 0.052	0.073 ± 0.014
SF_{CHAOS}	1.01 ± 0.15	1.14 ± 0.22

Table 5.3: Efficiency selecting c and b tagged jets and scale factor (SF_{CHAOS}) for sum of the outputs CHAOS cut of 1.65.

In the particular case of $light$ jets falsely tagged as heavy flavor, the scale factor is not needed, since their contribution is estimated directly from data. However, the efficiency for the CHAOS cut is computed from MC, being 4.9%.

Chapter 6

Search for Gluino-mediated Bottom Squark

This chapter describes the search for bottom squarks ($\tilde{b}$) produced though gluino ($\tilde{g}$) decay [93]. We look for gluino pair production $p\bar{p} \rightarrow \tilde{g}\tilde{g}$, where the gluino decays to $\tilde{g} \rightarrow b\tilde{b}$, with the subsequent sbottom decay to a b quark and the lightest neutralino ($\tilde{\chi^0}$), $\tilde{b} \rightarrow b\tilde{\chi^0}$. The neutralino is taken to be the Lightest Supersymetric particle and R-parity conservation is assumed. Therefore, the gluino signature is 4 b-jets and large missing transverse energy.

The theoretical motivation is described in chapter 2, section 2.3.1. In the following sections, the analysis procedure, techniques, and result are discussed.

6.1 Dataset and Basic Selection

The described analysis is based on 2.5 fb^{-1} of CDF Run II data collected between March 2003 and April 2008.

The data were collected with the three-level logic trigger MET45. A sequence of cuts on the $\not\!\!E_T$ is required at each level. At Level 1 it requires $\not\!\!E_T$ above 25 GeV, at Level 2 it requires $\not\!\!E_T$ above 35 GeV and at Level 3 it requires $\not\!\!E_T$ above 45 GeV.

Events computed in the present analysis are required to have a reconstructed vertex with z-position within 60 cm of the nominal interaction point, $\not\!\!E_T \geq 70$ GeV and tracking activity consistent with the energy measured in the calorimeter to reject cosmics and beam-halo background. Two or more jets are required to accept the event. Jets are defined using a cone-based

algorithm [89] with radius 0.4 and required to have a transverse energy above 25 GeV and a pseudorapidity $|\eta| \leq 2.4$. At least one of the jets is required to be central ($|\eta| \leq 0.9$) and the jet with the highest transverse energy must satisfy $E_T \geq 35$ GeV. Table 6.1 shows the list of basic cuts applied in the analysis.

Basic cuts
$\not\!\!E_T$ quality cuts (section 4.5)
At least 2 jets
$E_{T,jets} > 25$ GeV
$\|\eta_{jets}\| \leq 2.4$
$E_{T,j1} \geq 35$ GeV
$\not\!\!E_T > 70$ GeV

Table 6.1: Basic selection applied in the analysis.

Since it is expected a 4 b-jets final state, two categories are made by requiring only one of the jets or at least two jets to be tagged as originating from a heavy-flavour quark. In order to identify jets originating from a b-quark, the SecVtx tagging algorithm (section 5.1) is used. The double tag category provides much more sensitivity than the single tag, therefore the former is used to extract the limits and the latter is used to provide an additional control sample.

6.2 Trigger Efficiency

This section describes the trigger efficiency of the MET45 path computed for the analysis. The efficiency is obtained using data and applied to the Monte Carlo predictions for signal and backgrounds.

A sequence of cuts on $\not\!\!E_T$ are required at each trigger level in the path under study. The resolution of the computed $\not\!\!E_T$ increases with the trigger decision level:

- Level 1: $\not\!\!E_T > 25$ GeV
- Level 2: $\not\!\!E_T > 35$ GeV
- Level 3: $\not\!\!E_T > 45$ GeV

To compute the final trigger efficiency we parametrize the trigger turn-on at each level using four different samples, shown in Table 6.2.

Sample description	CDF name
Muon sample with $p_T > 18$ GeV requirement	HIGH_PT_MUON
Jet sample requiring at least one jet with $E_T > 50$ GeV	JET50
Jet sample requiring at least one jet with $E_T > 20$ GeV	JET20
$\not\!\!E_T$ requiring 25 GeV and prescaled	*MET Back-up*

Table 6.2: Samples used for trigger studies.

Using the parameterization of all the considered levels and samples, we compute the total efficiency of the path by multiplying the fitted functions, at the different levels, for each sample. We consider that the muon sample is the one closest to the selection of signal events containing real $\not\!\!E_T$. Therefore, it is taken as the central prediction for the efficiency.

The other predictions are used to estimate the uncertainty in the turn-on parameterization. It should be noted that the precision in the fit is larger than the differences among the results obtained by using the different samples. We quote the following uncertainty as a parameterization of the relative uncertainty.

$$\Delta\epsilon/\epsilon(\not\!\!E_T) = \begin{cases} 0.07 \cdot \left[\frac{90-\not\!\!E_T}{30}\right]^3 & \text{if } \not\!\!E_T < 90 \text{ GeV}, \\ 0.00 & \text{if } \not\!\!E_T \geqslant 90 \text{ GeV}. \end{cases}$$

Due to the large growing term, motivated by the differences with the jet samples, the use of the sample for $\not\!\!E_T < 50 - 60$ GeV is clearly discouraged. In that region a more sophisticated multi-variable parameterization is needed to reduce the systematic uncertainty due to the possible influence of the topology in the selection. For this purpose, more suitable triggers are available.

Figure. 6.1 shows the trigger turn-on efficiency as a function of $\not\!\!E_T$. The turn-on efficiency is obtained multiplying the fitted functions computed at each trigger level. Four different trigger turn-on functions are shown and the ratio of this functions to the central one (extracted from the muon sample). In the ratio, we compare the measured differences with the estimated uncertainty and confirm that the uncertainty covers the difference among the samples.

It should be noted that the parameterization from the *MET Back-up* sample has a small bias due to the fact that no function at Level 1 was fitted. However, since the main effect in the region

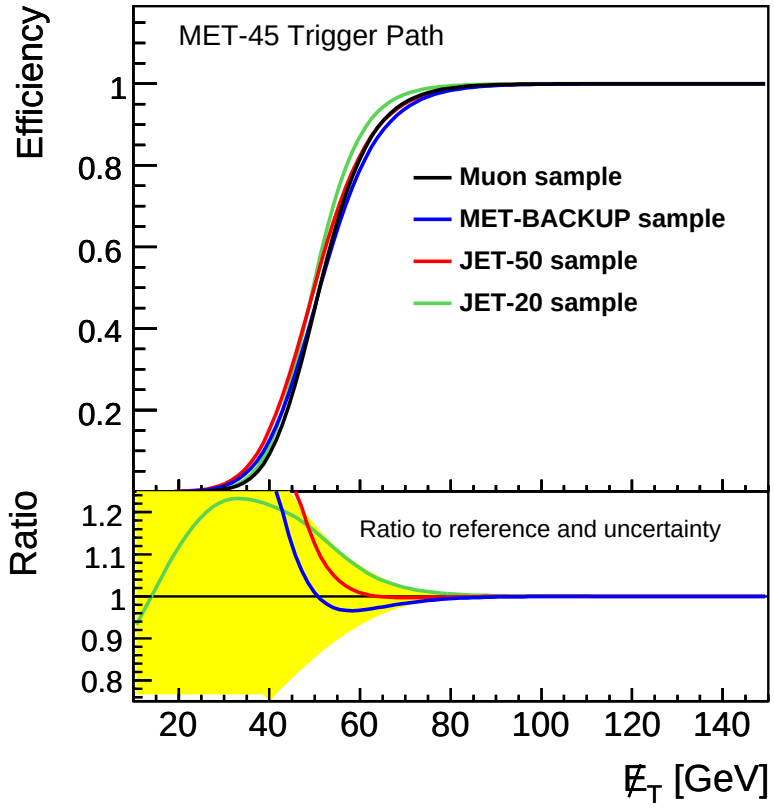

Figure 6.1: Total efficiency for the MET45 Trigger Path as obtained from the several samples we are using in this study. The plot below shows the ratio to the efficiency obtained with the HIGH_PT_MUON sample, which we consider our central reference. The yellow area displays the size of the uncertainty we quote on the trigger efficiency.

of interest is coming from the Level 2 and Level 3 turn-on functions, the effect is negligible.

We use the parameterization obtained from the HIGH_PT_MUON sample and the quoted uncertainty, to weight the MC events in the several regions under study.

6.3 Monte Carlo Signal Samples

The signal predictions are obtained by computing the acceptance using the PYTHIA [62] event generator normalized to the NLO production cross section determined with PROSPINO event generator [61] and the CTEQ6M [64, 65] parton distribution functions.

Several signal Monte Carlo samples are generated and passed through the detector simu-

lation in order to cover the phase space under study as a function of the sbottom and gluino masses. These samples are generated setting explicitly the SUSY parameters of the model, which only affects the masses of the involved particles since the production process is via the strong interaction and all the decay branching ratio are set to 100%. The gluino mass is varied between 240 GeV/c^2 and 400 GeV/c^2 and the sbottom masses from 150 GeV/c^2 to 350 GeV/c^2. The neutralino mass is fixed to 60 GeV/c^2, while the squark mass is fixed to 500 GeV/c^2.

The points generated are shown in the figure 6.2 along with the previous limit by a similar analysis [63], the excluded region by the sbottom-pair production analysis made by DØ [94], and the region excluded by CDF Run I [95].

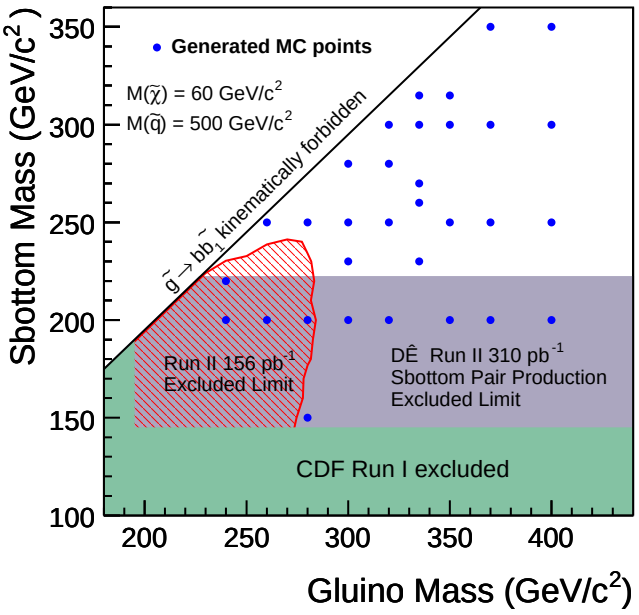

Figure 6.2: SUSY points (blue squares) generated with PYTHIA showed in the $m(\tilde{g})$-$m(\tilde{b})$ plane. Previous limit, the excluded region by the sbottom-pair production analysis made by DØ , and the region excluded by CDF Run I are shown.

6.4 Background Processes

Several SM processes, produced at Tevatron, have a final state that mimic the signal under study. Events selected in the analysis have as main characteristics: large $\not\!\!E_T$, large jet multiplicity, heavy flavor jets, and no leptons.

Dominant SM backgrounds are top-quark pair-production and single top-quark production, electroweak boson and diboson production, heavy-flavor multijet production, and light-flavor jets falsely tagged as b jets (mistags). The latter two background contributions are estimated from data. The PYTHIA event generator is used to estimate the remaining backgrounds. For the event generation the CTEQ5L [96] parton distribution functions were used. Events are passed through the GEANT3-based [97] CDF II detector simulation and weighted by the probability that they would pass the trigger as determined in independent data samples.

In order to test the ability to model the backgrounds, and also to compute the data-driven ones, several control regions are define as described in section 6.5.

6.4.1 Top Production

Top-quark pair-production and single top-quark production are considered as backgrounds in this analysis. Both contributions are measurable in the signal region. The top-quark production is not only most significant because of its larger cross section, but rather, become one of the largest backgrounds because of its high jet multiplicity and the presence of two b quarks in the final state.

The single top-quark event yields are normalized to the theoretical cross sections [98]. We use the top-quark pair production cross section of $\sigma_{t\bar{t}} = 7.3 \pm 0.8$ pb [99], as measured by CDF II in 2006.

6.4.2 W/Z and Diboson Production

W/Z and diboson events are negligible in the signal region after the requirement of high jet multiplicity (3 or more jets). However, without this requirement, as it happens in one of the signal regions, these processes become important and comparable with all the other sources of background.

The event yields for the electroweak boson samples are normalized to the leading order cross section provided by PYTHIA, scaled by 1.4 to account for higher order (NLO) corrections. Due to the limited ability of PYTHIA to simulate multijet environments, a 40% uncertainty [100] is assigned for the extracted yields of events with a W or Z boson and jets.

The diboson event yields are normalized to the theoretical NLO cross sections [101, 102].

6.4.3 Mistags

The mistags are light-flavor jets falsely tagged as heavy flavor jets. Although the mistag efficiency is two orders of magnitude smaller than the heavy flavor tagging efficiency, the large cross section of processes producing light flavor jets makes the mistag background one of the largest in the single-tag data sample, and even in the double-tag data sample, for some kinematic selections.

The way in which the mistag matrix is computed and applied, is explained in detail in section 5.2.

6.4.4 Heavy-Flavor Multijet Production

Heavy-flavor multijet events have a cross section which is several orders of magnitude larger than any other background. These processes produce $\not\!\!E_T$ if a heavy-flavor quark (b or c) produces a semi-leptonic decay. Mismeasured jets also produce imbalance in the total transverse energy, causing the inclusion of these events in the signal region. While the probability of a mismeasurement is small, the large cross section of HF multijet events makes them the main background.

Due to the large cross section of the HF multijet production, the amount of MC simulated events needed to model the background is huge. To generate such a sample, a large amount of informatic resources should be used during months. For this reason, a data driven method becomes mandatory to estimate this background.

To estimate the HF multijet background from data, we have developed a multijet tag rate estimator (MUTARE) which is fully described in the next section 6.4.5.

6.4.5 MUTARE Method

The **MU**ltijet **TA**g-**R**ate **E**stimator (MUTARE) is a method to estimate the HF multijet background from data, explicitly created for this analysis but with a broad spectrum of usage.

The method baseline is well known in experimental physics. Based on the idea of a object-rate being constant among different samples, the key of the method is to select the appropriates objects (numerator) and proto-objects (denominator). The objects are, obviously a subsample of the proto-objects. In the particular case of MUTARE the rate is define as:

$$R = \frac{HF\ tagged\ jets}{Taggable\ jets} \tag{6.1}$$

where HF tagged jets are the objects we want to estimated from a proto-object population, taggable jets. The sample used to compute the rate has to pure enough in the desired events to compute the rate with precision. As a sophistication of the simplest object-rate method, if the rate is parametrized on several variables, the rate becomes a matrix instead of a single factor.

In summary, MUTARE parametrizes the probability of a taggable jet to become tagged. This probability is computed in high purity multijet sample (section 6.5) and applied in other samples assuming that the ratio, R_{mutare}, does not change within the samples.

The practical implementation of MUTARE in the analysis is based on a three-dimensional tag-rate matrix applied to each jet in an event following a parametrization on E_T, $|\eta|$ and the scalar sum of E_T of all jets in the event. Each element of the matrix is computed in a multijet enhanced sample as:

$$R_{MUTARE} = \frac{N_{tags} - N_{mistags} - N_{tags}^{MC}}{N_{taggable} - N_{taggable}^{MC}} \tag{6.2}$$

where N_{tags} is the number of tagged jets, $N_{mistags}$ is the number of mistags, N_{tags}^{MC} is the number of tagged jets from non-multijet production computed from MC, $N_{taggable}$ is the number of taggable jets, and $N_{taggable}^{MC}$ is the number of taggable jets from non-multijet production computed from MC. Jets are defined as taggable if E_T^{raw} >10 GeV, η <2.4, and have at least two good tracks (as described in section 5.1).

The final prediction is obtained after subtracting the HF contribution coming from non-multijet production processes.

$$N_{events}^{HF\ multijet} = R(N_{taggable}^{data} - N_{taggable}^{MC}) \tag{6.3}$$

The amount of non-multijet contribution to the taggable jets ($N_{taggable}^{MC}$) is computed by applying the MUTARE matrix to each non-multijet MC sample mentioned before.

In principle, MUTARE does not provide the absolute normalization but the shape. However, in this analysis normalization is not required since the agreement between data and prediction is quite good, and the quoted error cover any possible small discrepancy.

6.5 Control Regions

To avoid potential biases when searching for new physics we perfom a "blind search". To be sure about our predictions' reliability, we test the various background contributions in distinct control regions that are defined *a priori*, and in which the expectation for signal is negligible when compared to the background and to the signal sample. The three control regions used to check the SM prediction are denoted as HF multijet, lepton, and pre-optimization regions. All the basic selection cuts showed in Table 6.1 are required. In addiction, SecVtx algorithm is applied requiring single and double b-tagged events in each region.

The pre-optimization control region is defined as a signal-like region without optimization cuts. Hence, this region is the benchmark for the optimization process. The other two regions are defined to be orthogonal to the pre-optimization one. The HF multijet region is a multijet-enriched region, requiring the second leading jet to be aligned with the $\not\!\!E_T$. In this region, the MUTARE matrix is computed. The lepton region, in which at least one isolated lepton is required, is used to test the electroweak W/Z boson and top backgrounds, where they are important contributions. The explicit cuts defining each region are:

- **HF multijet control region:** second leading E_T jet ($\vec{j}_2$) aligned with the $\vec{\not\!\!E}_T$, where aligned means $\Delta\phi(\vec{\not\!\!E}_T, \vec{j}_2) \leq 0.4$ rad.
- **Lepton control region:** second leading E_T jet not aligned with the $\vec{\not\!\!E}_T$ ($\Delta\phi(\vec{\not\!\!E}_T, \vec{j}_2) \geq 0.7$ rad) and at least one isolated lepton (as defined in section 4.2).
- **Pre-optimization control region:** leading and second-leading E_T jets not aligned with the $\vec{\not\!\!E}_T$, required leading jet $E_T > 50$ GeV, and to have no identified leptons.

Predicted total numbers of events and distributions of kinematic variables such as jet E_T, the track multiplicity, and the $\not\!\!E_T$ have been studied and found to be in agreement with observations in the three control regions. As an example, the $\not\!\!E_T$ and the first jet E_T distributions in the three control regions are shown in figure 6.3 for the single b-tag analysis, and in figure 6.4 for the double b-tag analysis.

The background contributions to the number of expected exclusive single b-tagged and inclusive double b-tagged events and the observed events in the control regions are summarized in Table 6.3 and Table 6.4.

Regions	Multijet	Lepton	Pre-optimization
Electroweak bosons	88 ± 37	152 ± 57	417 ± 162
Top-quark	65 ± 16	405 ± 93	523 ± 119
Light-flavor jets	5430 ± 2226	190 ± 78	919 ± 377
HF Multijets	9741 ± 4870	195 ± 97	1660 ± 830
Total expected	15325 ± 5355	943 ± 166	3520 ± 934
Observed	15390	890	3525

Table 6.3: Comparison of the total number of expected events with total uncertainties and observed single b-tagged events in the control regions.

Regions	Multijet	Lepton	Pre-optimization
Electroweak bosons	10 ± 7	21 ± 14	33 ± 22
Top-quark	19 ± 6	111 ± 34	146 ± 45
Light-flavor jets	225 ± 49	8 ± 2	57 ± 12
HF Multijets	839 ± 419	25 ± 12	270 ± 135
Total expected	1093 ± 422	165 ± 39	506 ± 144
Observed	1069	159	451

Table 6.4: Comparison of the total number of expected events with total uncertainties and observed double b-tagged events in the control regions.

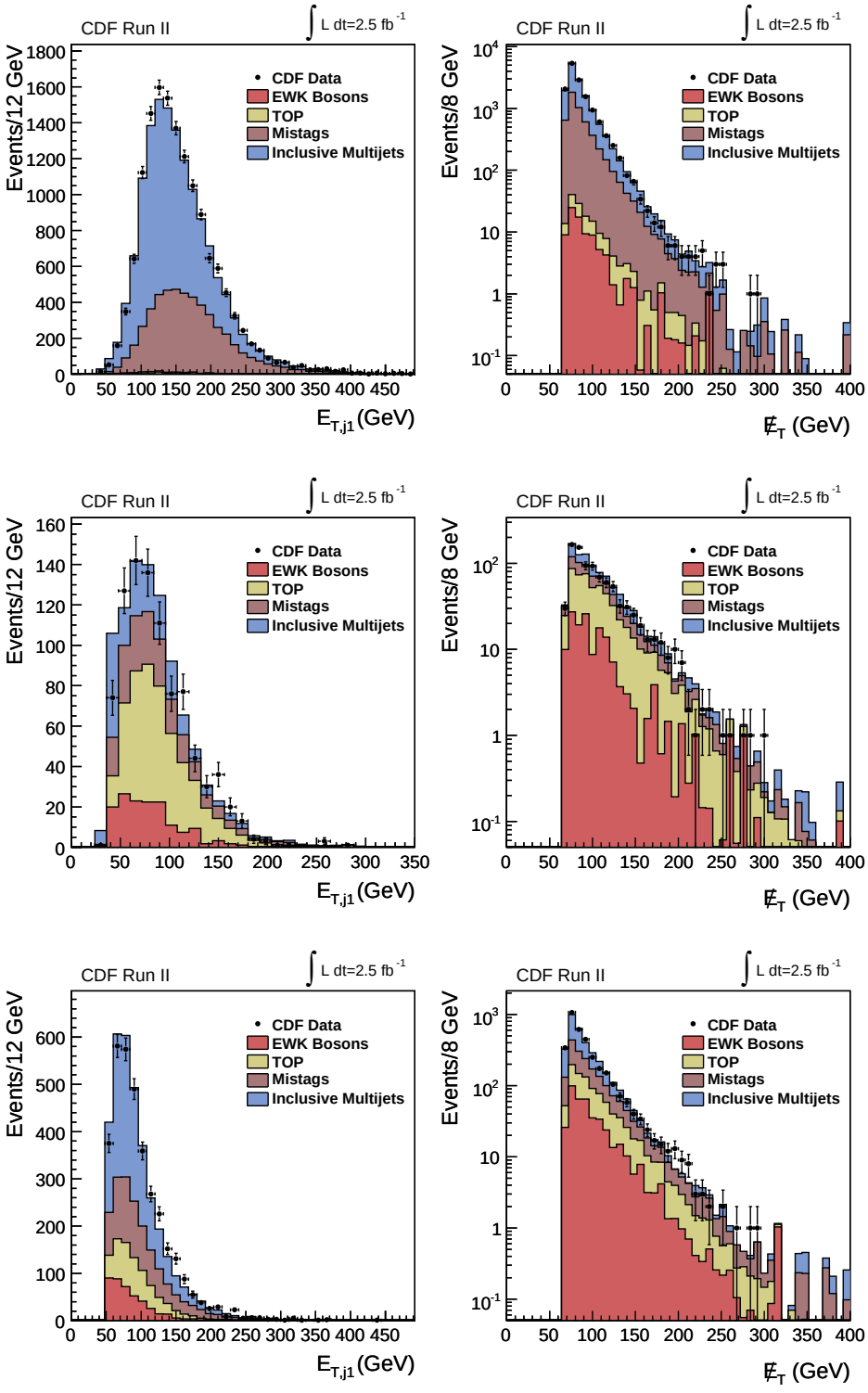

Figure 6.3: Leading jet E_T, and $\not\!\!E_T$ in the HF multijet (top), lepton (middle) and pre-optimization (bottom) control regions with single b-tagged events.

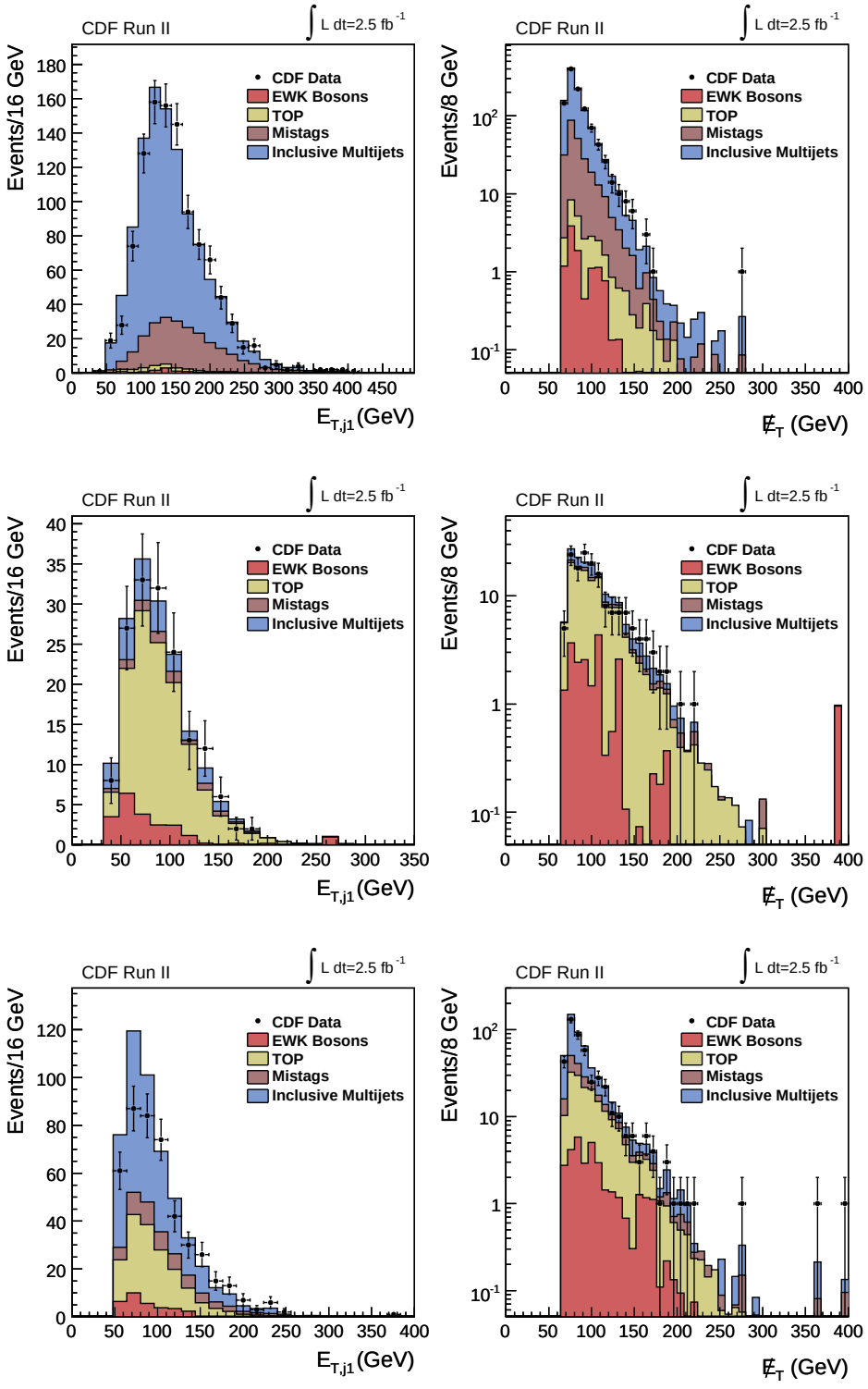

Figure 6.4: Leading jet E_T and $\not\!\!E_T$ in the HF multijet (top), lepton (middle) and pre-optimization (bottom) control regions with double b-tagged events.

6.6 Signal Optimization

An optimization process via two neural networks (NN) is made in order to reduce the background contribution and enhance the sensitivity to the signal. We choose two reference signal points based on values of $\Delta\, m \equiv m(\tilde{g}) - m(\tilde{b})$ and perform the same optimization procedure. The two points are chosen in a region not excluded by previous analyses and representing two different kinematic behaviors:

- Large Δm optimization $\Rightarrow$ M($\tilde{g}$) = 335 GeV/c^2, M($\tilde{b}$) = 260 GeV/c^2
- Small Δm optimization $\Rightarrow$ M($\tilde{g}$) = 335 GeV/c^2, M($\tilde{b}$) = 315 GeV/c^2

The optimization process takes as benchmark the pre-optimization selection. In addiction to the cuts required in the pre-optimization region, for the large Δm optimization a cut on the number of jets greater than two is applied. For the small Δm optimization this cut is not applied because of the small amount of momentum available in the gluino decay, which translates into a lower jet multiplicity in the final estate.

Over this selection, two consecutive Neural Networks are applied and an event selection is made by cutting on its outputs:

- First Neural Network: called multijet-NN, is applied to distinguish between gluino signal and HF multijets background. This Neural Network is trained with signal MC versus taggable jets (QCD-like) in the pre-optimization region with one exclusive tag in order to have enough statistics.
- Second Neural Network: called top-NN, is applied to remove the remaining backgrounds, mainly top-pair production, and it is trained with signal MC versus top pair MC also over the pre-optimization region with one exclusive tag after applying the cut on the previous multijet-NN.

The previous optimization process is applied over the two chosen signal points requiring one exclusive and two inclusive b-tagged events.

The architecture used in both QCD multijet-NN and top-NN, the performace, and the results of each neural network is described in the following sections. The output of each Neural Network, used as a dicriminant, is distributed within an interval of -1 to 1, where the background peaks at -1 and the signal peaks at 1.

6.6.1 Neural Networks Architecture

The Neural Networks used in the present analysis are trained and tested using the TMVA package [103]. The same structure is used for all the Neural Networks, consisting in two layers with N+1 and N nodes respectively, where N is the number of variables, and one output node. As an architecture example, figure 6.5 shows the multijet-NN in the large Δm optimization.

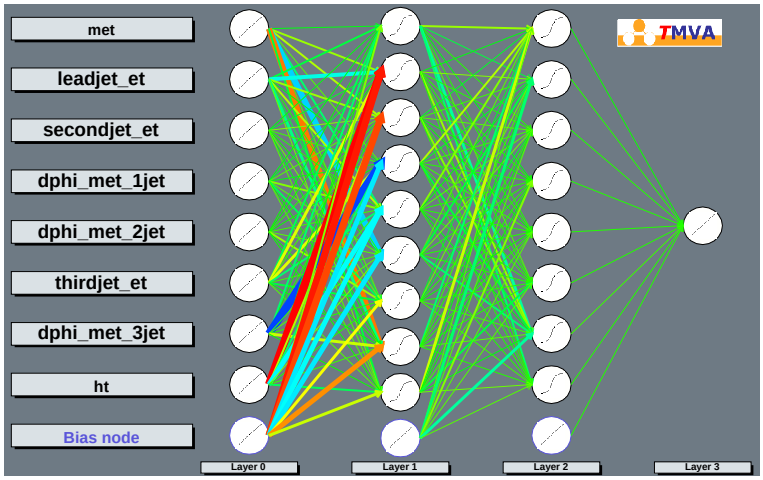

Figure 6.5: neural network's architecture used for training. In particular for the multijet-NN in the large Δm optimization.

The same set of variables, all of them related to the jet and $\not{E}_T$ kinematics, are used in the multijet-NN and top-NN. Depending on the optimization, large or small Δm, the set of variables is different due to the cut on number of jets applied in each selection. Table 6.5 shows the variables used in each optimization. All the variables are well modeled and are found as the ones providing the best separation power as is shown in appendix A.

6.6.2 Multijet Neural Network

Applying to the pre-optimization region the multijet-NN we obtain the outputs showed in figure 6.6 for the large Δm optimization and for the small Δm optimization (one exclusive tag and two inclusive tags).

For all the cases showed in figure 6.6 we find 0.8 as an optimal value for the selection cut. This cut optimizes the sensitivity keeping a reasonable amount of signal.

Large Δm optimization	Small Δm optimization
$\vec{\not\!\!E}_T$	$\vec{\not\!\!E}_T$
$E_{T,j1}$	$E_{T,j1}$
$E_{T,j2}$	$E_{T,j2}$
$E_{T,j3}$	$\Delta\phi(\vec{\not\!\!E}_T, \vec{j}_1)$
$\Delta\phi(\vec{\not\!\!E}_T, \vec{j}_1)$	$\Delta\phi(\vec{\not\!\!E}_T, \vec{j}_2)$
$\Delta\phi(\vec{\not\!\!E}_T, \vec{j}_2)$	$Min\ \Delta\phi(\vec{\not\!\!E}_T, \vec{j}_i)$
$\Delta\phi(\vec{\not\!\!E}_T, \vec{j}_3)$	summed E_T of all the jets in the event
summed E_T of all the jets in the event	

Table 6.5: List of input variables used in both multijet-NN and top-NN.

6.6.3 Top Neural Network

At this stage of the optimization we apply the second neural network, based on top pair discrimination, to the events obtained after the cut on 0.8 on the multijet-NN output. The result of applying the top-NN to this events is shown in figure 6.7 for the large Δm optimization as well as for the small Δm optimization (one exclusive tag and two inclusive tags).

We find 0.6 as an optimal selection cut in the large Δm optimization and 0.8 in the small Δm optimization.

Performing the whole optimization process we obtain four final regions, depending on the tagging requirements, and the signal point used in the optimization. However, only the final regions requiring two b-tagged jets are used as a final results due to their sensitivity. The one b-tagged events regions are treated as additional control regions.

As expected from a "blind search", the optimization procedure is made over the predictions. CDF II data, as shown in the figures, is plotted once the process is finished.

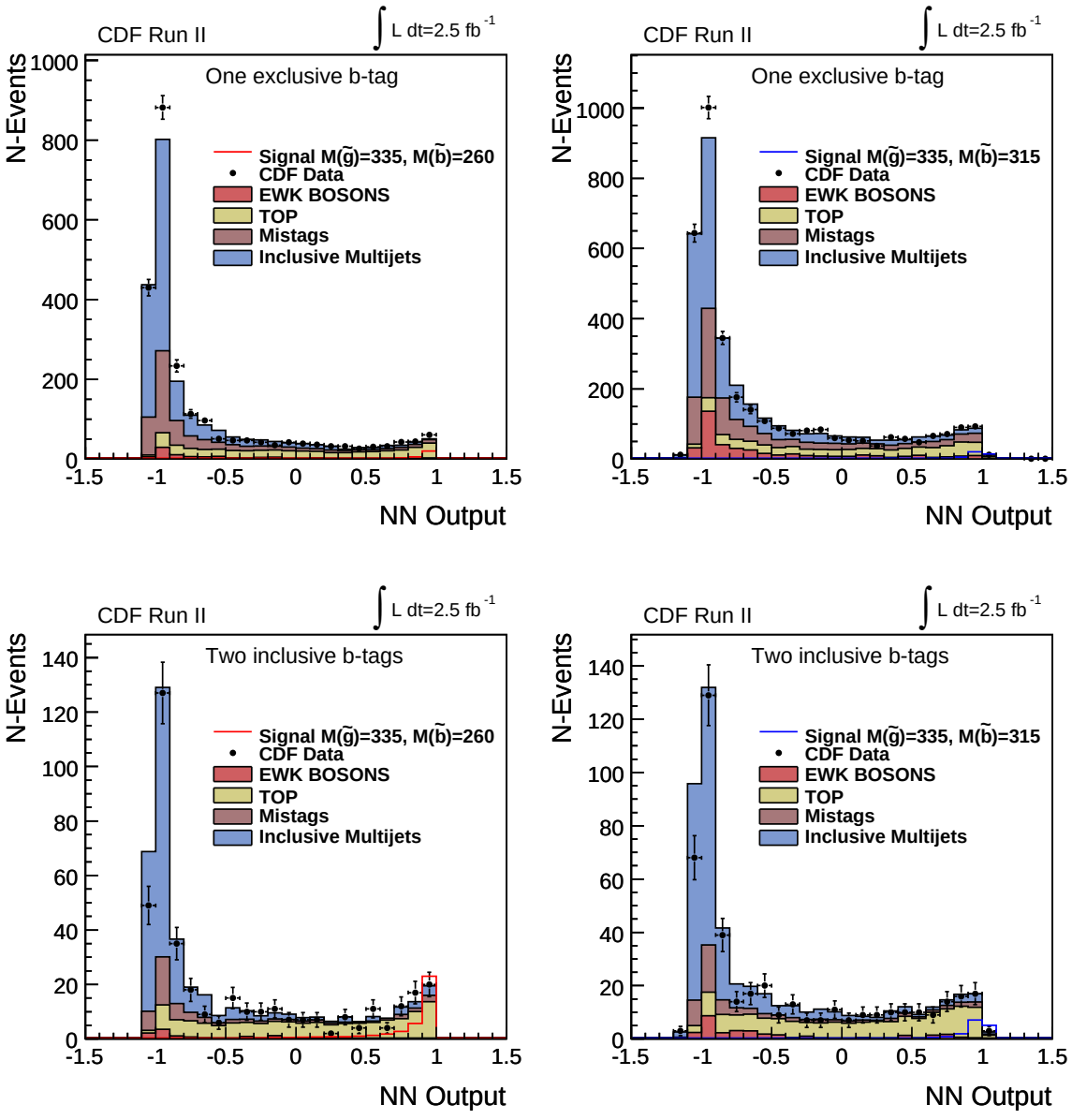

Figure 6.6: Multijet-NN output plots for the large Δm (left) and small Δm (right) optimizations, requiring one b-tagged (top) or two b-tagged (bottom) events.

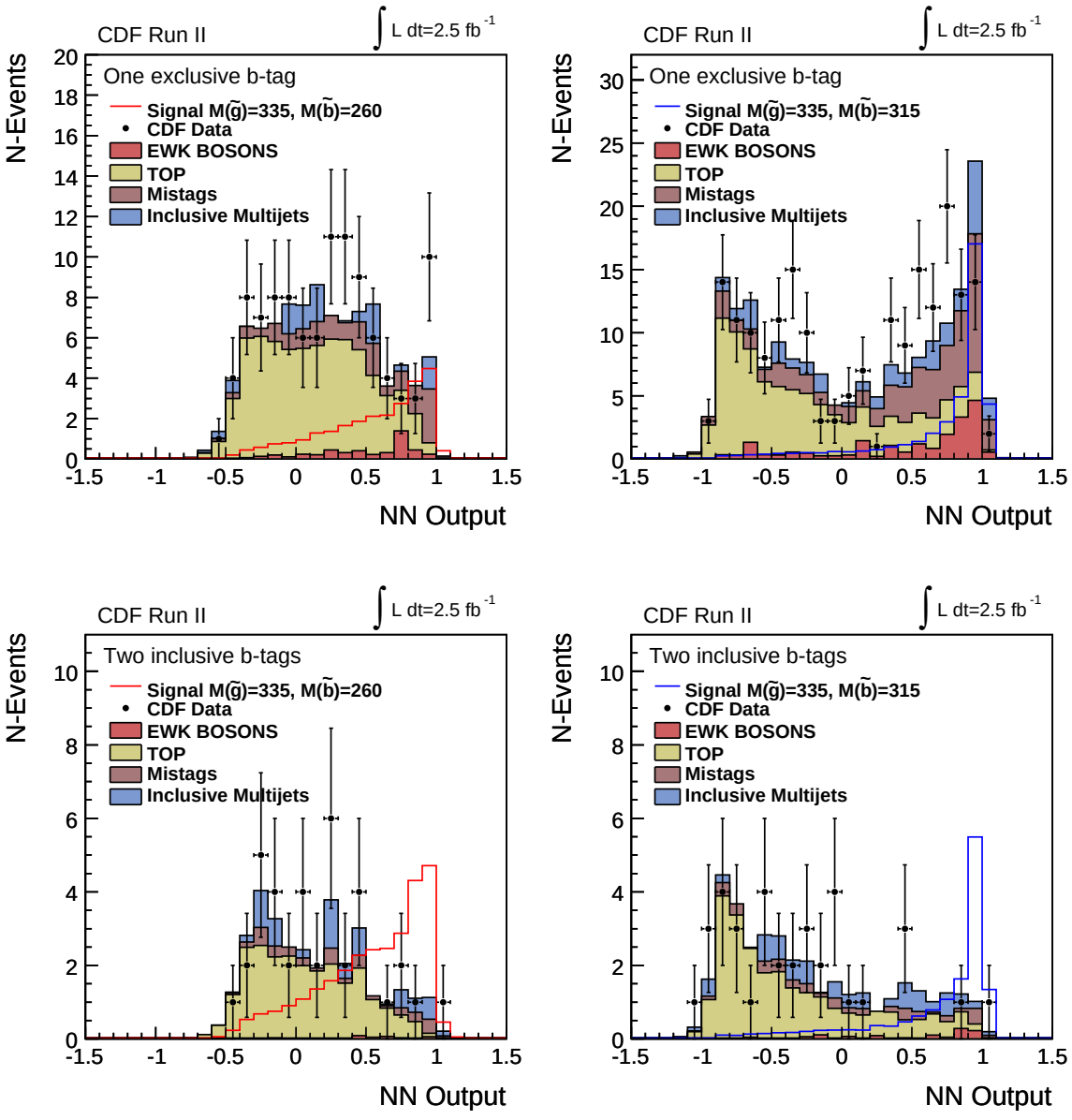

Figure 6.7: Top-NN output plots for the large Δm (left) and small Δm (right) optimizations, requiring one b-tagged (top) or two b-tagged (bottom) events.

6.7 Systematic Uncertainties

Systematic errors are the main source of uncertainty in this search. Some of these errors affect the overall normalization of the signal or background templates. This kind of systematic errors, so-called rate systematics, summarize effects that impact the number of events in the signal and background templates. However, the shapes of these templates are not affected by these sources of uncertainty.

Contrarily, some other systematic uncertainties make the shapes of the templates to vary. This second kind of systematic errors, named shape systematics, could also affect the overall number of events. These differences in shape are accounted for by producing sets of shifted templates in parallel to the nominal ones.

The systematic uncertainties on the signal and the background predictions, taking into account correlated and uncorrelated uncertainties, are studied.

- Jet Energy Scale [90]: A systematic error in the calorimeter energy scale affect the total transverse energy on the jets. The effect in the final regions varies in a range between 5% and 25% depending on the optimization.

- b-tagging Scale Factor: The difference between data and MC in b-tagging efficiency (5%) is taken as systematic uncertainty. The resulting uncertainty in the final regions varies between 1.5% and 5% depending on the optimization.

- Mistag estimation: The systematic error assigned to the tag rate matrix is 4.8%.

- Luminosity: The systematic uncertainty in the luminosity is taken to be 6%, affecting to the normalization of all the MC estimated backgrounds.

- ISR/FSR: The uncertainty associated with the initial and final state radiation was evaluated by generating sample with more/less ISR/FSR. The effect in the final regions varies in a range between 2% and 5% depending on the optimization.

- PDF: The PDF uncertainty has been determined to be 2% on the acceptance.

- QCD Multijet Background: We assign a conservative 50% uncertainty in the prediction based on the variation observed when matrix definition is changed.

- Top-Pair Production cross section: We quote the uncertainty in the CDF measured value (11%) of the top-pair production cross section.

- Single Top Production cross section: We quote the theoretical uncertainty in the single-top cross section (13%).

- Diboson Production cross section: We quote the theoretical uncertainty being 10% in the WW and WZ cross sections and 20% for the ZZ process.

- Single EWK Boson Production cross section: Although the cross section for Z and W production are known to a high precision, we are using the inclusive processes in PYTHIA to perform estimations of Z/W+multijet contributions since PYTHIA parton showering does not properly reproduce the multijet spectrum, we estimate a 40% uncertainty in the predictions.

- Top quark mass: In the current analysis, the $t\bar{t}$ production background is estimated using MC with a top quark mass of 171.5 GeV/c^2. Since our signal optimization is based on a Neural Network trained with $t\bar{t}$ processes we include a systematic error due to the top pair neural network output dependence on the top quark mass. We compute this error measuring the number of top-pair events in the final selection by using a top quark mass of 174.5 GeV/c^2. The effect in the final regions varies in a range between 0.3% and 17% depending on the optimization.

6.8 Results

The signal region is analyzed after the background predictions are determined. As described above, we find 0.8 as an optimal value for the selection cut for both multijet-NN outputs and 0.6 (0.8) for the top-NN outputs in the large (small) Δm optimization within an interval of -1 to 1, where the background peaks at -1 and the signal peaks at 1. We observe 5 (2) events for the large (small) Δm optimization region, where 4.7 ± 1.5 (2.4 ± 0.8) are expected from background, as summarized in Table 6.6.

Since no significant deviation from the SM prediction is observed, the results are used to calculate an exclusion limit for the cross section of the described gluino process. We use a Bayesian method to determine the 95% credibility level (C.L.) upper limit on the $\tilde{g}\tilde{g}$ cross section, assuming a uniform prior probability density. We treat the various correlated uncertainties as nuisance parameters, which we remove by marginalization, assuming a Gaussian prior distribution. The obtained limit is such that no more than 8.0 (5.4) events are observed in the large (small) Δm signal region. Figure 6.8 shows the expected and observed limits as a function of

Optimizations	Large Δm	Small Δm
Electroweak bosons	0.17 ± 0.05	0.5 ± 0.3
Top-quark	1.9 ± 1.0	0.6 ± 0.4
Light-flavor jets	1.0 ± 0.3	0.6 ± 0.1
HF Multijets	1.6 ± 0.8	0.7 ± 0.3
Total expected SM	4.7 ± 1.5	2.4 ± 0.8
Observed	5	2
Optimized $\tilde{g}$ signal	14.9 ± 5.0	8.5 ± 2.8

Table 6.6: Number of expected and observed events in the signal regions. Predictions for the signal points are also shown. Correlated and uncorrelated uncertainties in the total background and expected signal were treated separately in the analysis although they are combined here.

$m(\tilde{g})$ for two values of the $\tilde{b}$ quark mass. The expected limit is computed by assuming that the observed number of events matches the SM expectation in each signal region.

The gluino production cross section limit is nearly independent of the sbottom mass between 250 and 300 GeV/c^2, and is around 40 fb for $m(\tilde{g}) = 350\ \mathrm{GeV}/c^2$. In addition, using the assumed model, a 95% C.L. limit is obtained in the parameter plane of the model. Figure 6.9 shows the excluded region in the gluino-sbottom mass plane, compared with the results from previous analyses [94, 95, 104, 63]. The limit obtained with the present analysis improves the results of previous searches using similar topology and also, under the assumptions discussed above, sets a more stringent limit on the sbottom and gluino production than dedicated sbottom searches in the region where those particles have similar masses.

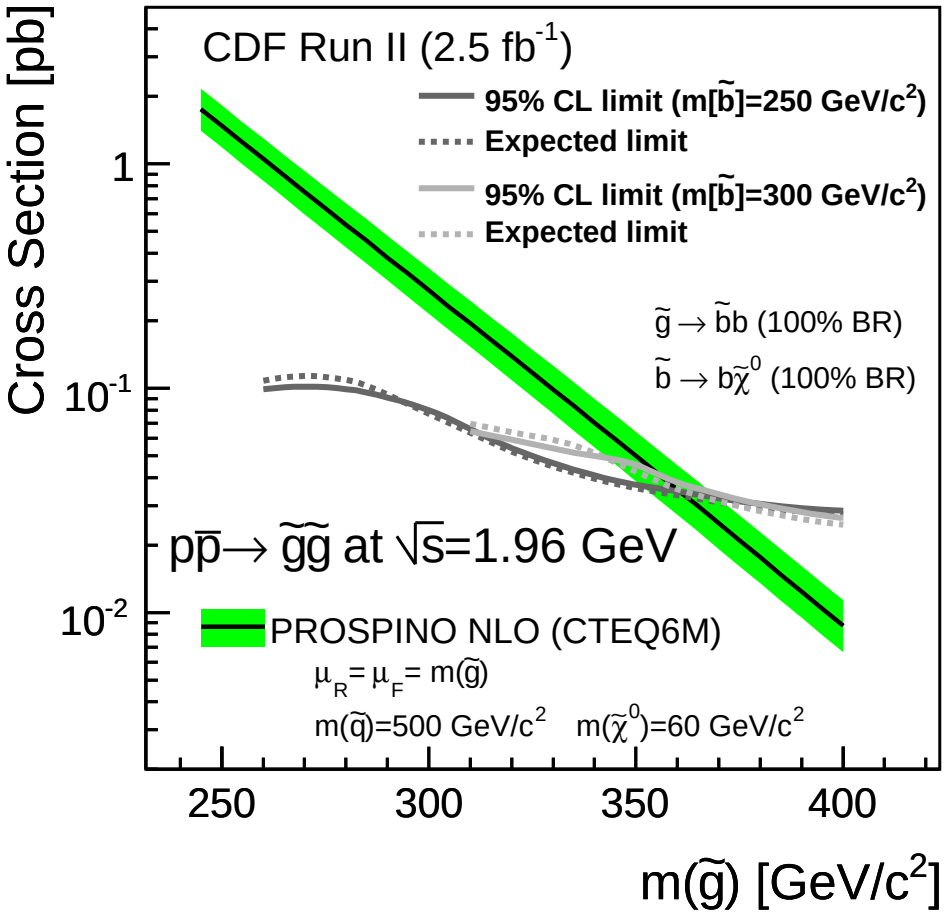

Figure 6.8: Observed (solid lines) and expected (dashed lines) 95% C.L. upper limit on the gluino cross section (solid line with band) as a function of the gluino mass for two assumed values of the sbottom mass. The shaded band denotes the uncertainty on the NLO $\tilde{g}\tilde{g}$ production due to the truncated higher-order terms and the parton distribution functions.

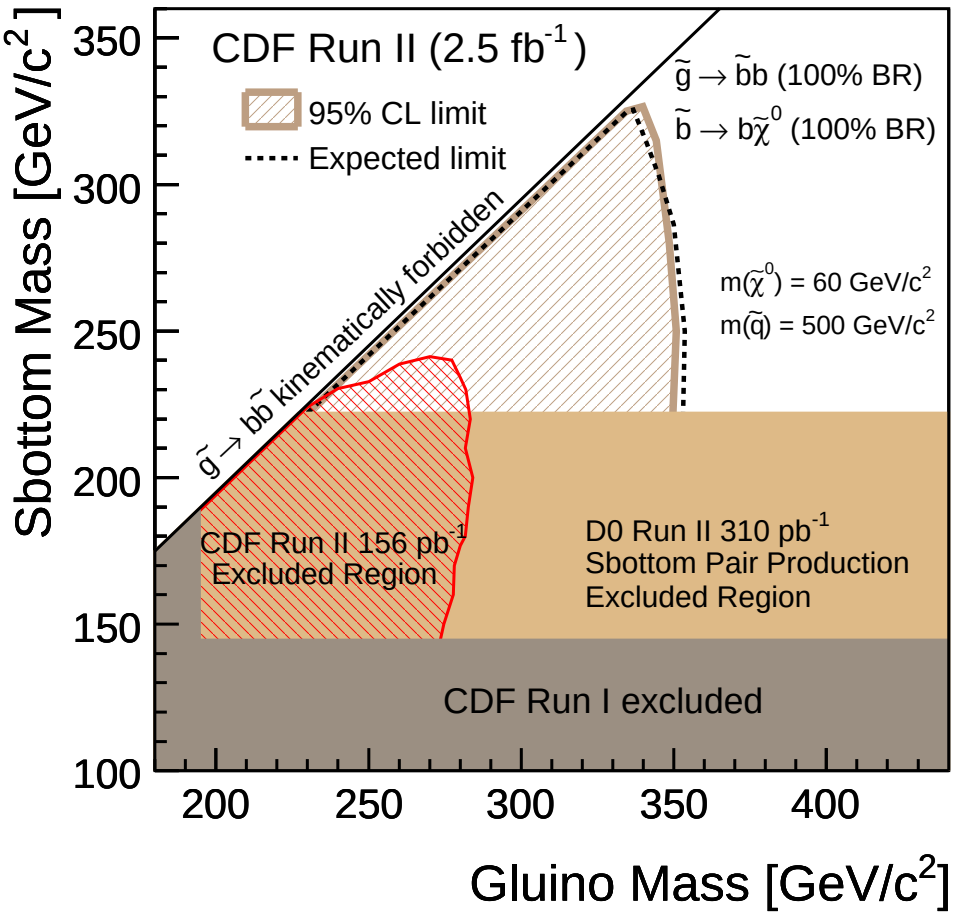

Figure 6.9: Excluded region at 95% C.L. in the $m(\tilde{g})$-$m(\tilde{b})$ plane for a $m(\tilde{\chi}^0) = 60$ GeV/c^2, $m(\tilde{q}) = 500$ GeV/c^2. The result is compared to the previous results from CDF in Run I [104], and Run II [63] and direct sbottom production by DØ [94].

Chapter 7

Search for Scalar Top Decaying into Charm and Neutralino

This chapter describes the second analysis presented in this thesis. We search for direct top squarks ($\tilde{t}$) production, $p\bar{p} \rightarrow \tilde{t}\tilde{t}$, where the stop decays to $c\tilde{\chi}^0$. The neutralino is taken to be the Lightest Supersymetric particle (LSP) and R-parity conservation is assumed. Therefore, the stop signature is 2 c-jets and missing transverse energy.

The theoretical motivation is described in chapter 2, section 2.3.2. In the following sections the analysis procedure, techniques, and result will be discussed.

7.1 Dataset and Basic Selection

The described analysis is based on 2.6 fb^{-1} of CDF Run II data collected between March 2003 and April 2008.

The data were collected with the three-level logic $\not\!\!E_T$+jets trigger. A sequence of cuts on the $\not\!\!E_T$ is required at each level plus additional cuts requiring two jets at level 2.

Events computed in the analyisis are required to have a reconstructed vertex with z-position within 60 cm of the nominal interaction point, $\not\!\!E_T \geq 50$ GeV and tracking activity consistent with the energy measured in the calorimeter to reject cosmics and beam-halo background. Two or more jets are required to accept the event. Jets are defined using a cone-based algorithm [89] with radius 0.7 and required to have a transverse energy (E_T) above 25 GeV and a pseudorapidity $|\eta| \leq 2.4$. At least one of the jets is required to be central ($|\eta| \leq 0.9$) and the jet with

the highest transverse energy must satisfy $E_T \geq 35$ GeV. Table 7.1 shows the list of basic cuts applied in the analysis.

Basic cuts
$\not\!\!E_T$ quality cuts (section 4.5)
At least 2 jets
$E_{T,jets} > 25$ GeV
$\|\eta_{jets}\| \leq 2.4$
$E_{T,j1} \geq 35$ GeV
$\not\!\!E_T > 50$ GeV
$\Delta R(j_1, j_2) > 0.1$ rad

Table 7.1: Basic selection applied in the analysis.

Since two c jets in the final state are expected, one of the jets is required to be originated from a heavy-flavor quark. In order to identify this heavy-flavor jet, the loose SecVtx tagging algorithm is used.

7.2 Trigger Efficiency

This section describes the trigger efficiency of the MET+JETS path computed for the analysis. A secuence of cuts are required at each trigger level in the path under study. The resolutions of the quantities involved increase with the trigger decision level:

- Level 1: $\not\!\!E_T > 25$ GeV
- Level 2: (depending on the period)
  - L2_TWO_JET10_L1_MET25
  - L2_CJET10_JET10_L1_MET25
  - L2_CJET10_JET10_L1_MET25_LUMI190
  - L2_CJET10_JET10_L1_MET25_DPS
  - L2_MET30_CJET20_JET15_DPS
- Level 3: $\not\!\!E_T > 35$ GeV

The trigger simulation for Monte Carlo events is not fully reliable, due to that, the trigger efficiency is computed in data samples used as reference. Monte Carlo events are weighted according to such efficiency which is a function of the kinematic properties of the events.

Thorough studies has been perfomed to parameterize the trigger efficiency for the dataset used in this analysis. This parameterization has been made in the appropriate variables for the several requirements of the trigger at all the levels and was validated using different reference samples 7.2.

Sample description	CDF name
Muon sample with $p_T > 18$ GeV requirement	HIGH_PT_MUON
Jet sample requiring at least one jet with $E_T > 50$ GeV	JET50
Jet sample requiring at least one jet with $E_T > 20$ GeV	JET20
$\not\!\!E_T$ requiring 25 GeV and prescaled	*MET Back-up*

Table 7.2: Samples used for the MET+JETS path trigger studies.

The final parameterization, obtained mainly using the *HIGH-PT MUON* sample, is directly applicable to the the analysis, since the jet selection and $\not\!\!E_T$ reconstruction are identical in both cases. The uncertainty associated to the trigger efficiency has been estimated by cross-checking the resulting parameterization with the jet samples.

Regarding the parameterization of the trigger efficiency, we have improved the precision of the calculations making use of specific parameterizations in different kinematic regions. This introduces a bit of complication in the practical implementation of the weighting of MC events, but it clearly allows the reduction of the uncertainties.

The trigger efficiency consist on six different parameterizations in six different kinematic regions, as shown in Table 7.3

Figure. 7.1 shows one of the six trigger turn-on efficiencies as a function of $\not\!\!E_T$. The turn-on efficiency is obtained multiplying the fitted functions computed at each trigger level. Four different trigger turn-on functions are shown and the ratio of this functions to the central one (extracted from the muon sample).

The effect of the uncertainty is small due to the kinematic selection performed in the analysis and to the improved parameterization of the turn-on applied to the MC events.

Kinematic regions	
$E_{T,j1} \leq 50\text{GeV}$	$+\Delta\phi(\vec{\not\!\!E}_T, \vec{j}_2) \leq 0.4$ rad
$50 \leq E_{T,j1} \leq 70\text{GeV}$	$+\Delta\phi(\vec{\not\!\!E}_T, \vec{j}_2) \leq 0.4$ rad
$E_{T,j1} \geq 70\text{GeV}$	$+\Delta\phi(\vec{\not\!\!E}_T, \vec{j}_2) \leq 0.4$ rad
$E_{T,j1} \leq 50\text{GeV}$	$+\Delta\phi(\vec{\not\!\!E}_T, \vec{j}_2) \geq 0.7$ rad
$50 \leq E_{T,j1} \leq 70\text{GeV}$	$+\Delta\phi(\vec{\not\!\!E}_T, \vec{j}_2) \geq 0.7$ rad
$E_{T,j1} \geq 70\text{GeV}$	$+\Delta\phi(\vec{\not\!\!E}_T, \vec{j}_2) \geq 0.7$ rad

Table 7.3: Kinematic regions used in the MET+JETS path trigger parameterization.

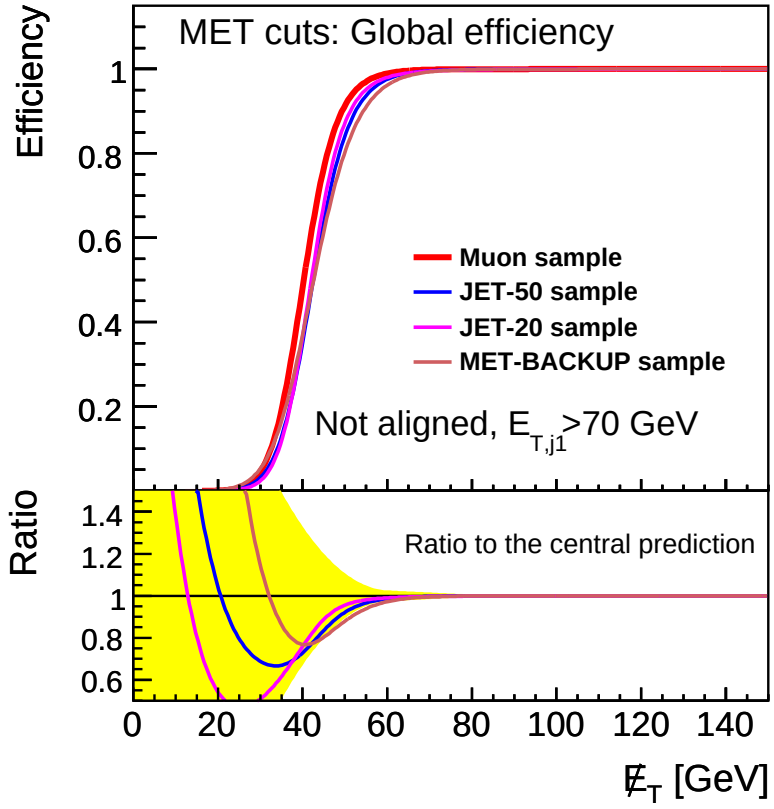

Figure 7.1: Total efficiency for the MET+JETS Trigger Path, as obtained from the several samples we are using in the study. This efficiency is one of the six trigger turn-on parametrizations used, in particular, the one for the region in which more signal is expected. The plot below shows the ratio to the efficiency obtained with the HIGH_PT_MUON sample, which we consider our central reference. The yellow area displays the size of the uncertainty we quote on the trigger efficiency.

7.3 Monte Carlo Signal Samples

The signal predictions are obtained using the program PROSPINO [61] to compute the total production cross section $p\bar{p} \rightarrow \tilde{t}\tilde{t}$, and PYTHIA [62] to estimate the event acceptance in the detector and in the application of our selection cuts.

Several signal Monte Carlo samples are generated with PYTHIA and passed through the detector simulation in order to cover the phase space under study as a function of the neutralino mass and stop mass. These samples are generated using the Tune AW [105] and setting explicitly the SUSY parameters of the model, which only affects the masses of the involved particles since the production process is via the strong interaction and all the decay branching ratio are set to 100%. The stop mass is varied between 90 GeV/c^2 to 195 GeV/c^2 and the neutralino mass from 60 GeV/c^2 to 125 GeV/c^2.

The generated signal points are showed in the figure 6.2 with the previous limit obtained by CDF [106], DØ [107], and LEP [108].

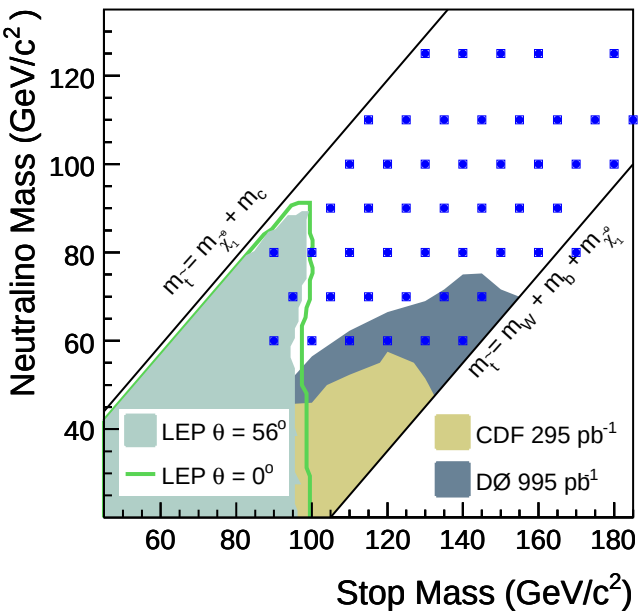

Figure 7.2: SUSY points (blue squares) generated with PYTHIA showed in the $m(\tilde{\chi}^0)$-$m(\tilde{t})$ plane. Previous limits by LEP, CDF, and DØ are shown.

7.4 Background Processes

Several SM processes, produced at Tevatron, have a final state that mimic the signal under study. Events selected in the analysis have as main charanteristics, large $\not\!\!E_T$, two jets with at least one of them originated from a heavy-flavor quark, and no leptons.

Part of the SM background in this analysis is predicted with MC simulation, in particular contributions from Z and W production in association with jets, $t\bar{t}$ production, single top and diboson production. In the case of $W/Z+$ jets processes, ALPGEN [109] and PYTHIA Monte Carlo generators are used. The ALPGEN prediction is used as the nominal estimation while the PYTHIA prediction is used as a cross check. Differences in shape between the two Monte Carlo estimations are taken as systematic uncertainties C. All the other background samples are generated with PYTHIA. Events are passed through the GEANT3-based [97] CDF II detector simulation and weighted by the probability that they would pass the trigger as determined in independent data samples.

tuning parameters set described above, and processed in a similar way as the signal events.

Background contributions from HF multijet production and light flavor jets falsely tagged as a heavy-falvour quark, are estimated from data.

In order to test the ability to model the backgrounds, and also to compute the data-driven backgrounds, several control regions are defined, as described in section 7.5.

7.4.1 Top Production

Top-quark pair-production and single top-quark production are considered as backgrounds in this analysis. Both contributions are measurable in the signal region. However, they are the smallest background contributions taken into account in the analysis. In contrast with the sbottom search, described in Chapter 6, where the top production is one of the largest backgrounds, in this analysis, due to the dijet selection and the one tag requirement, this contribution is highly suppressed.

The single top-quark event yields are normalized to the theoretical cross sections [98]. We use the top-quark pair production cross section of $\sigma_{t\bar{t}} = 7.02 \pm 0.63$ pb [110], as measured by CDF II in 2008.

7.4.2 W/Z and Diboson Production

W/Z and diboson events are the dominant background in the signal region. The presence of these event in the signal region, is mainly due to $W+$ jets production and $Z+$ jets, when the W decays into lepton and neutrino, and the Z boson decays into neutrinos.

As mention above, ALPGEN is the Monte Carlo generator used to compute the $W/Z+$ jets processes. ALPGEN calculates the matrix elements for processes containing additional radiated partons and passes the color information to the showering algorithm. This should give a more accurate modeling of the kinematics of the process than PYTHIA showering approximation, since it includes proper matrix element calculations of the radiation process. ALPGEN also calculates the leading-order cross section of each interaction it generates, which is useful for combining different processes. Once the events are generated they are passed to PYTHIA for parton showering. This procedure generates initial- and final-state gluon radiation for each event and allows them to decay to quark pairs, increasing the number of particles in the final state of the event. More particles may be added from effects of beam remnants or multiple interactions. This gives the final set of particles that are passed to the hadronization routine.

The way in which $W/Z+$ jets are generated in ALPGEN, using $W/Z + i$ partons, introduce a complication because of the double counting of events produced when a gluon, showered by PYTHIA, produces new partons in the final state. However, this issue is solved in ALPGEN package with the so-called MLM, a sort of matching between samples to decide which event is kept when a double counting occurs. The decision is made based on the angle between the partons.

After the procedure described above, event yields are normalized to the NLO cross sections as computed by MCFM [111].

An extra complication appears using samples including heavy flavor partons. In this case, the user is the one in charge of handle the double counting issue, using a generalization of the MLM method used in the light flavor samples.

The diboson event yields, estimated with PHYTIA, are normalized to the theoretical NLO cross sections [101, 102].

7.4.3 Mistags

The mistags are light-flavor jets falsely tagged as heavy flavor jets. Although the mistag efficiency is an order of magnitude smaller than the heavy flavor tagging efficiency, the large cross section of processes that produce light flavor jets make the mistag background one of the largest in the signal region, and the dominant one before optimization.

The way in which the mistag matrix is computed and applied, is explained in detail in section 5.2.

7.4.4 Heavy-Flavor Multijet Production

The HF multijet production has a very large cross section in comparison with the expected signal, however these processes usually do not produce $\not\!\!E_T$ in the final state. Events from multijet production pass our selection if a jet mismeasurement or a semi-leptonic decay from a meson produces $\not\!\!E_T$. In both cases the $\not\!\!E_T$ tends to be aligned with the first or second most energetic jet.

Due to the large cross section of the process, the amount of MC simulated events needed to model the background is huge. To generate such a sample, a large amount of informatic resources should be used during months. For this reason, a data driven method become mandatory to estimate this background.

To estimate the HF multijet background from data, we have developed MUTARE, described in section 6.4.5.

7.5 Control Regions

The SM processes predicted with MC or data-driven methods are tested in control regions defined as background-dominated samples in which the signal contribution is negligible. Two regions are defined by reversing the selection requirements introduced to suppress specific background processes. A third region is defined in order to check the analysis tools in a signal-like environment, but avoiding the application of cuts that would enhance the signal contribution to a measurable level. All the basic selection cuts showed in Table 6.1 are required. In addiction, loose SecVtx algorithm is applied requiring single HF-tagged events in each region.

The pre-optimization control region is defined as a signal-like region without optimization

cuts. Hence, this region is the benchmark for the optimization process. The other two regions are defined orthogonally to the pre-optimization one. The HF multijet region is a multijet enriched region, requiring the second leading E_T aligned with the $\not\!\!E_T$, in which the MUTARE matrix is computed. The lepton region, in which at least one lepton (defined in section 4.2) is required, is used to test the electroweak W/Z boson and top backgrounds, where they are dominant contributions. The lepton control region is also a good place to check the MUTARE prediction in lepton environment, testing the robustness of the method. The selection cuts defining each region are:

- **HF multijet control region:** second leading E_T jet ($\vec{j}_2$) aligned with the $\vec{\not\!\!E}_T$, where aligned means $\Delta\phi(\vec{\not\!\!E}_T, \vec{j}_2) \leq 0.4$ rad.
- **Lepton control region:** second leading E_T jet not aligned with the $\vec{\not\!\!E}_T$ ($\Delta\phi(\vec{\not\!\!E}_T, \vec{j}_2) \geq 0.7$ rad) and at least one isolated lepton (as defined in section 4.2).
- **Pre-optimization control region:** leading and second-leading E_T jets not aligned with the $\vec{\not\!\!E}_T$, and no identified isolated leptons.

The first jet transverse energy and the $\not\!\!E_T$ distributions for the multijet, lepton, and pre-optimization control regions, are shown in figure 7.3, figure 7.4, and figure 7.5. Good agreement between data and SM predictions is obtained in all control regions. Table 7.4 shows the various backgrounds contributions compare to data in each region.

Due to the intrinsic properties of the MUTARE method we do not expect an accurate prediction of the normalization in regions where the fraction of heavy flavor to the total multijet content is different to the one in which the parametrization was computed. For this reason the HF multijet prediction is normalized to data in the lepton control region for comparison of the kinematic distribution.

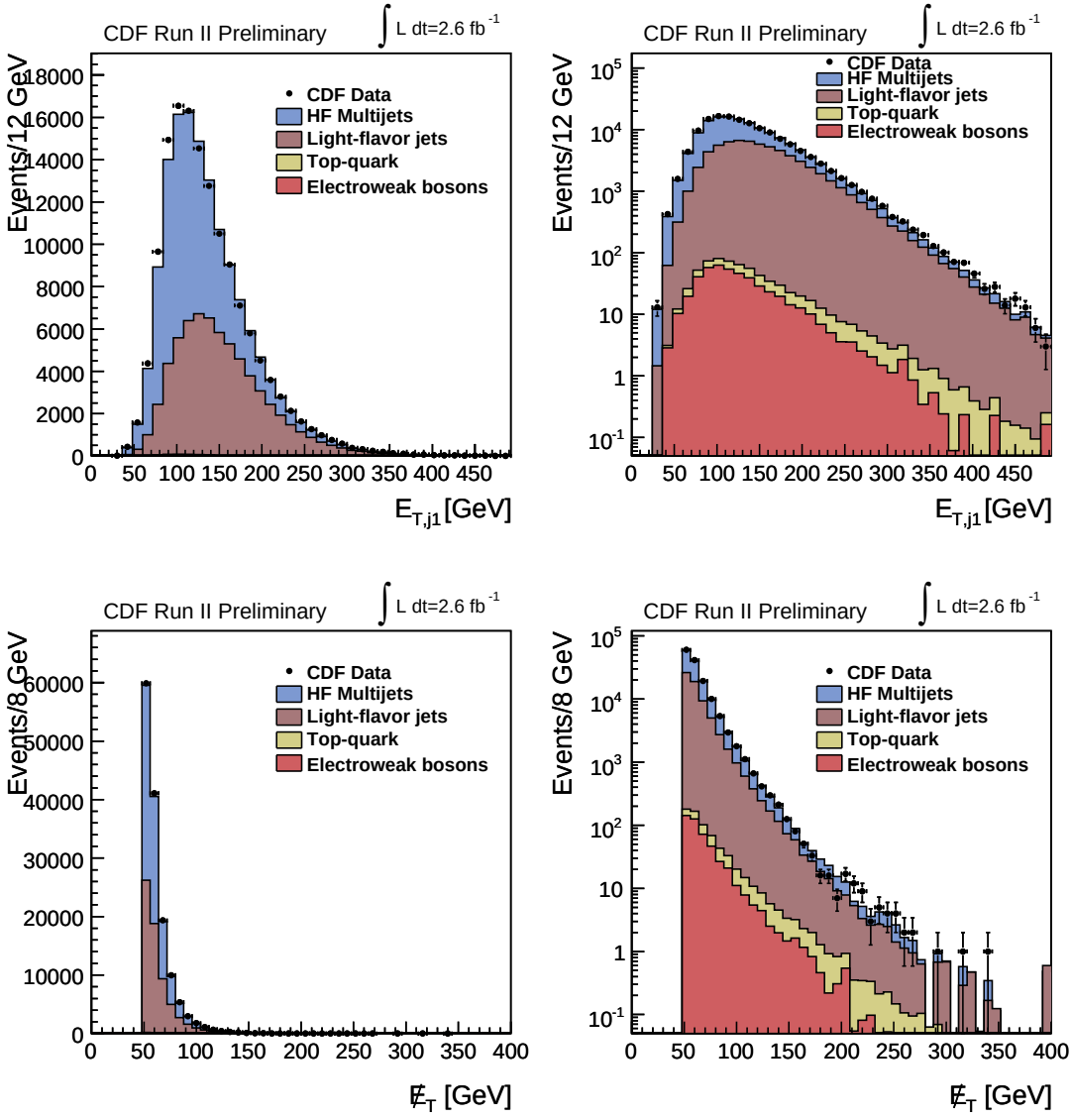

Figure 7.3: Leading jet E_T and $\not\!\!E_T$ in linear (left) and logarithmic (right) scales in the HF multijet control region.

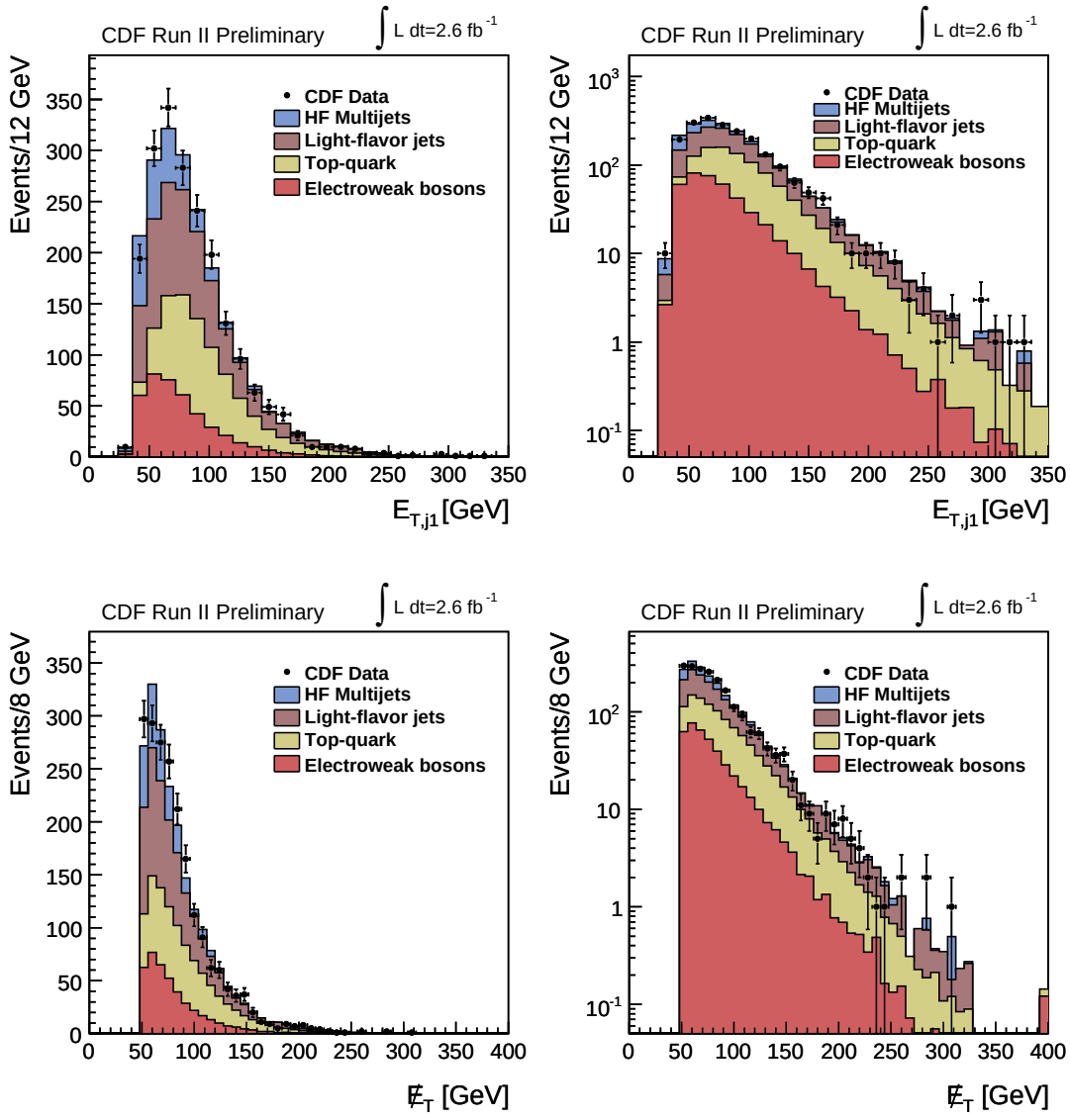

Figure 7.4: Leading jet E_T and $\not\!\!E_T$ in linear (left) and logarithmic (right) scales in the lepton control region.

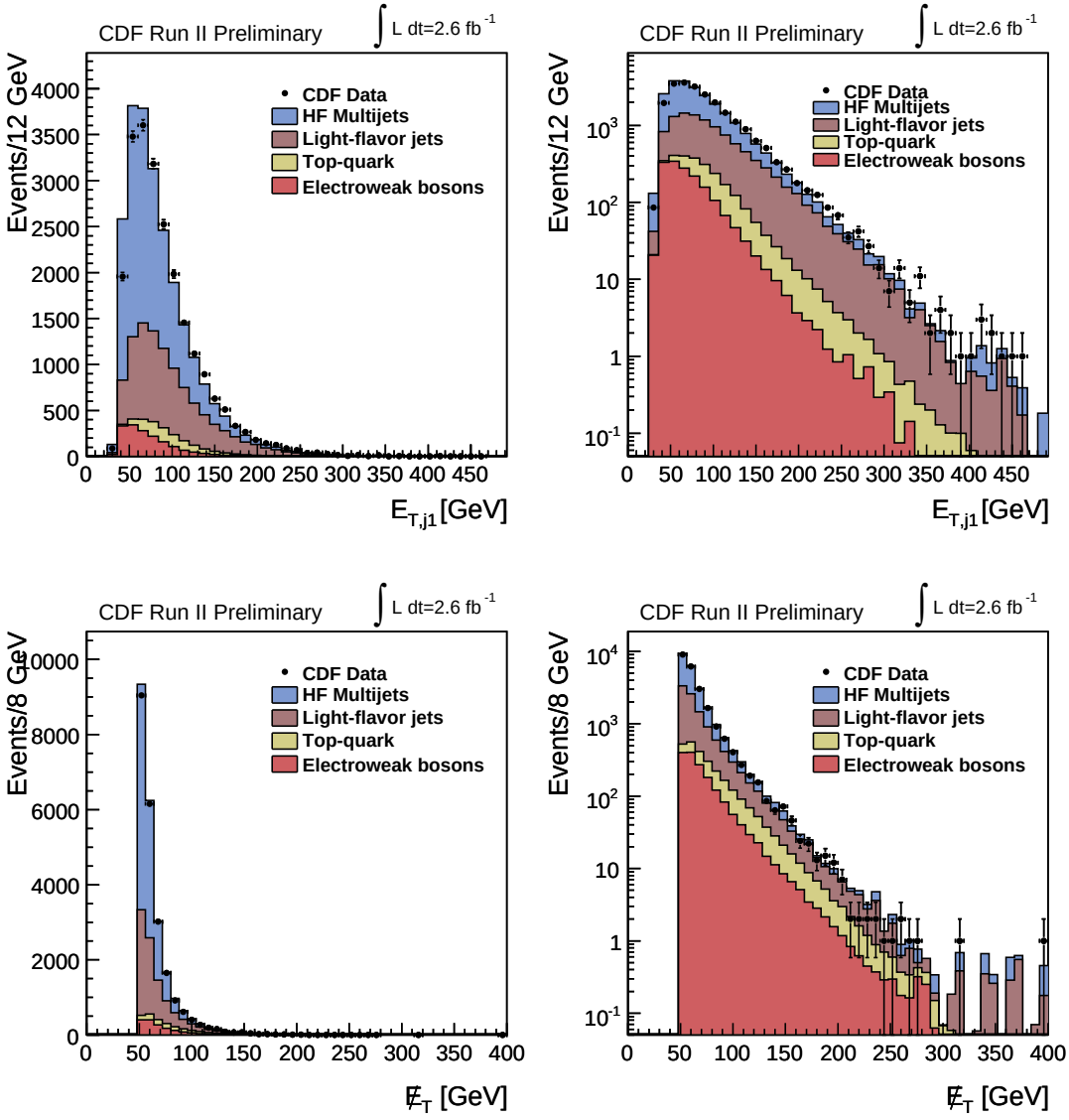

Figure 7.5: Leading jet E_T and $\not\!\!E_T$ in linear (left) and logarithmic (right) scales in the pre-optimization control region.

CDF Run II Preliminary 2.6 fb^{-1}

Regions	Multijet	Lepton	Pre-optimization
W/Z + jets production	457 ± 190	375 ± 156	1551 ± 644
Diboson production	17 ± 2	45 ± 5	118 ± 13
Top pair production	188 ± 21	547 ± 60	870 ± 96
Single top production	11 ± 2	71 ± 10	130 ± 19
HF QCD Multijets	75407 ± 23376	268 ± 83	12935 ± 4010
Light-flavour contamination	65839 ± 8427	720 ± 92	7741 ± 991
Total expected	141919 ± 24849	2026 ± 208	23345 ± 4182
Observed	143441	2026	22792

Table 7.4: Comparison of the total number of expected events with total uncertainties and observed single tagged events in the control regions.

7.6 Signal Optimization

In order to increase the signal over background ratio in the analysis, an optimization process was performed taking the pre-optimization selection as benchmark. The optimization process consists on the application of kinematic cuts and a Neural Network to reduce the HF multijet background, and finally a flavor separator to enhance the c jet contribution in the final state.

7.6.1 Heavy-Flavor Multijet Removal Cuts

As a first step in the optimization process, we select events with only two jets, as it is expected from the signal under optimization, and fulfilling the condition $\Delta\phi(\not\!\!E_T, Track\not\!\!E_T) < \pi/2$. This variable takes into account the angular difference between the "standard" $\not\!\!E_T$ from the calorimeter and the $Track\not\!\!E_T$ calculated with tracks. When the $\not\!\!E_T$ in the event is real, these two quantities are usually aligned in ϕ. However, when the $\not\!\!E_T$ comes from calorimetry mis-measurements, as HF multijet events (with no real $\not\!\!E_T$) populating the $\not\!\!E_T$ sample, the angular difference between the two quantities is more randomly distributed. The application of these cuts allow us to reduce drastically the HF multijet contribution in a simple way and also prevent us to train the neural network with these HF multijet events that are clearly different from the signal.

These two variables, number of jets, and $\Delta\phi(\not\!\!E_T, Track\not\!\!E_T)$ in which we are applying the cuts, are shown in figure 7.6.

7.6.2 Heavy-Flavor Multijet Neural Network

A Neural Network is applied as second step in the optimization process. The goal of this neural network is to remove HF multijet events.

After choosing the set of variables used as input for the neural network, a training and test evaluations have been performed with the framework of the TMVA package [103], using taggable jets (HF multijet like) as background and stop (m($\tilde{t}$) = 125 GeV/c^2, m($\tilde{\chi}_0$) = 70 GeV/c^2) MC as signal. The architecture of the neural network consists in two layers with N+1 and N nodes respectively, where N is the number of variables, and one output node as shown in figure 7.7. The variables used during the training and test process are listed in Table 7.5. All these variables are well modeled and are found as the ones proving the best distinction power between signal and background, as shown in appendix B.

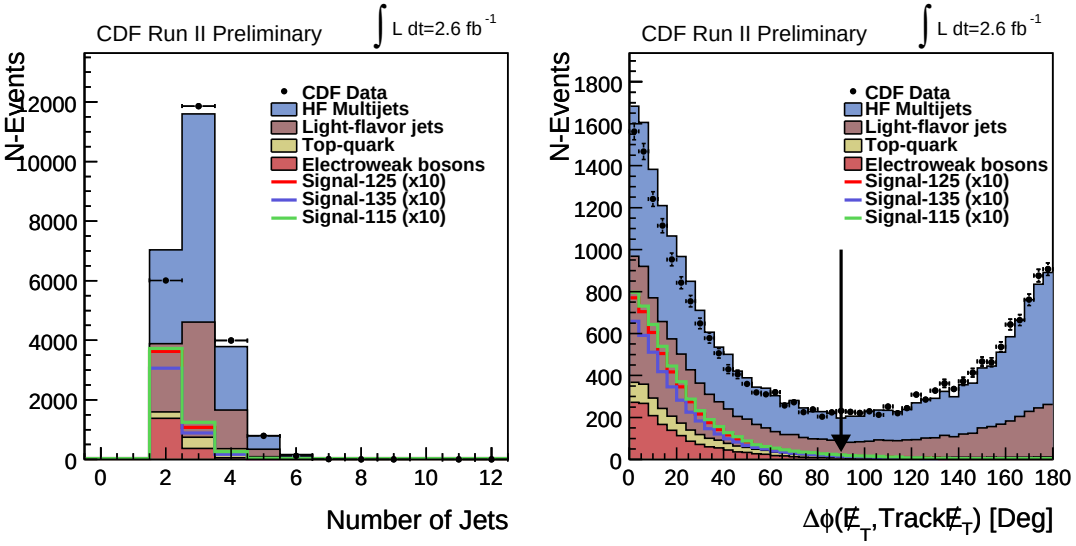

Figure 7.6: Number of jets (left) and $\Delta\phi(met, Track\not{E}_T)$ (right) distributions in the Pre-optimization region. The plots show the background prediction, data and stop signals with m($\tilde{t}$) = 115, 125, and 135 GeV/c^2 and m($\tilde{\chi}_0$) = 70 GeV/c^2.

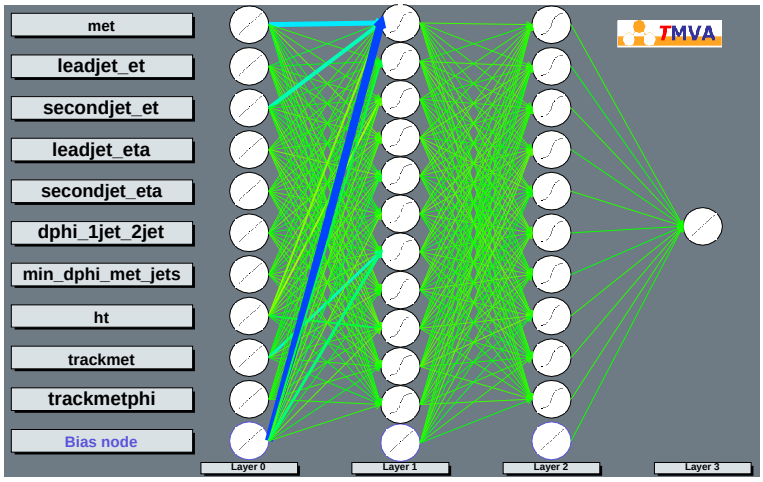

Figure 7.7: Neural network's architecture used for the training. The background is taggable jets from data (QCD-like) and the signal is stop MC with m($\tilde{t}$) = 125 GeV/c^2 and m($\tilde{\chi}_0$) = 70 GeV/c^2.

7.6.3 Neural Network Results

The neural network output obtained is distributed between -1 (backgroud like) and 1 (signal like). We select the events in the region between 0 and 1, applying a cut in the selection process, as shown in figure 7.8. Since the key point of the optimization is the application of the flavor separator, this cut on 0 may not have the best S/B ratio, but tries not to loose signal acceptance

HF multijet-NN variables	
$E_{T,j1}$	$\not\!\!\vec{E}_T$
$E_{T,j2}$	$Track\not\!\!\vec{E}_T$
η_{j1}	$min\Delta\phi(\not\!\!\vec{E}_T, jets)$
η_{j2}	$\Delta\phi(\not\!\!\vec{E}_T, Track\not\!\!\vec{E}_T)$
$\Delta\phi(\vec{j}_1, \vec{j}_2)$	$\sum_{i=1}^{N_jets} E_{T,ji}$

Table 7.5: List of input variables used in HF multijet-NN.

to exploit to the maximum the performance of further optimizations.

From this point on, we expect most of our sensitivity to the signal coming from the (0,1) output region, so we get a control region looking at the events in the (-1,0) interval. In fact, we are using this region (HF multijet enriched) to normalize the HF multijet prediction to data since we already know that our HF multijet prediction is slightly over-estimated in the pre-optimization region.

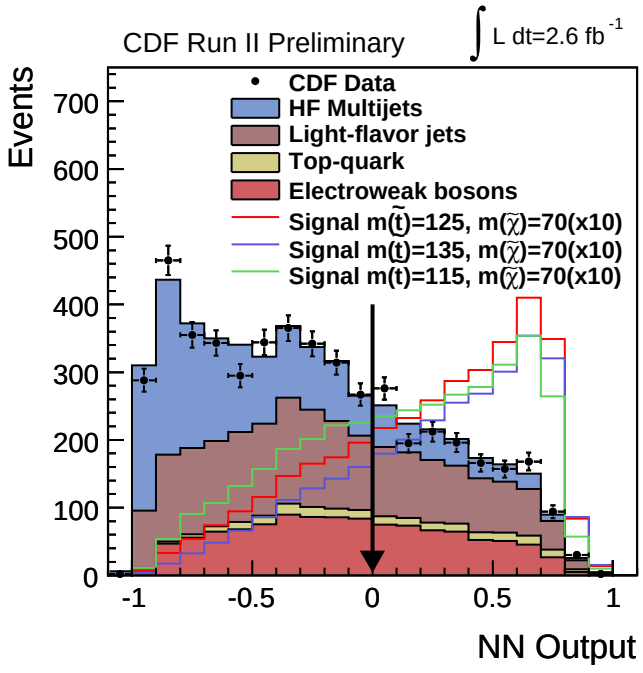

Figure 7.8: Output of the multijet-NN to reject HF multijet background. The arrow indicates the cut applied in the analysis.

7.6.4 Charm-jet Selection with CHAOS

The final stage in the stop signal optimization is the application of a flavor separator to enhance the sample with c jets. For this purpose, we develop CHAOS, a **C**harm **H**adron **A**nalysis **O**riented **S**eparator explicitly built for this analysis (described in section 5.3).

CHAOS is applied over the events already selected, cutting on the HF multijet-NN, with one heavy flavor tagged jet (loose SecVtx). The sum of the CHAOS outputs is distributed between 0 and 2 (c flavor). We select the events in the region between 1.65 and 1, applying a cut as shown in figure 7.9.

A scale factor on top of the SecVtx tagger is needed, for MC predictions, to take into account the differences in efficiency between data and MC. This scale factor is calculated explicitly for the cut we are applying in the analysis at 1.65 in the sum of the outputs, as shown in figure 7.9. The scale factors and efficiencies for b and c jets are described in section 5.4.

- $SF_{CHAOSb} = 1.14 \pm 0.22$
- $SF_{CHAOSc} = 1.01 \pm 0.15$

The application of CHAOS to data and MC is straight forward. However, obtaining the HF multijet and mistags prediction via MUTARE and mistag matrices after CHAOS is not possible. These two matrices are applied over taggable jets to obtain their predictions, nevertheless, to apply CHAOS tagged jets are needed.

To overcome this problem, we perform the following procedure. The amount of MUTARE and mistag prediction right before CHAOS application (Table 7.6) is known, so as far as we know the flavor efficiency of CHAOS cutting at 1.65 we apply this efficiency assuming the MUTARE as b-jets and the mistags as $light$-jets.

	Predictions
MUTARE	279.6
Mistags	658.3

Table 7.6: MUTARE and mistags prediction right before CHAOS.

The procedure used to compute the CHAOS' efficiencies is fully explained in section 5.4

In order to check the flavor composition of the MUTARE and mistags predictions in this region we perform a flavor-based template fit to data using the mass of the vertex variable. Using

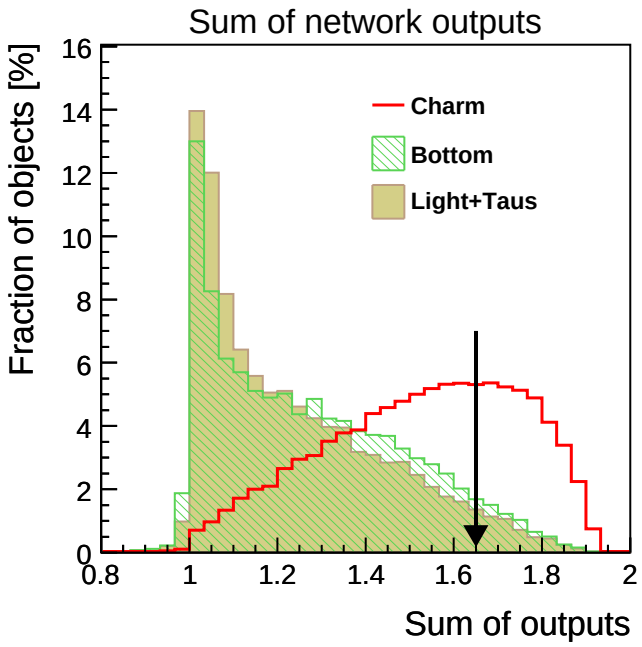

Figure 7.9: Sum of the CHAOS outputs in 1D applying the NN to the samples used for training. The arrow indicates the cut applied on the analysis to enhance the contribution of charm-jets.

the data distribution of the vertex mass subtracting all the backgrounds coming from MC we obtain the distribution of HF-multijet+mistags from data, right before the CHAOS application. Fitting flavor templates to the mass of the vertex extracted in this way we obtain the following amount of flavor contributions as is shown in figure 7.10.

- b jets from the fit = 388.2
- c jets from the fit ≈ 0
- $light$ jets from the fit = 492.4

From the fit we conclude that the amount of c jets is negligible at this point, therefore the procedure applying to the MUTARE prediction the b jet efficiency in CHAOS is a reasonable approach. The differences between the predictions and the numbers obtained from the fit are taken into account as systematics as explained in section 7.7.

One way to know if our light flavor template has a reasonable shape, is to compare it with the distribution obtained from negative tags from data. This comparison, for the mass of the vertex

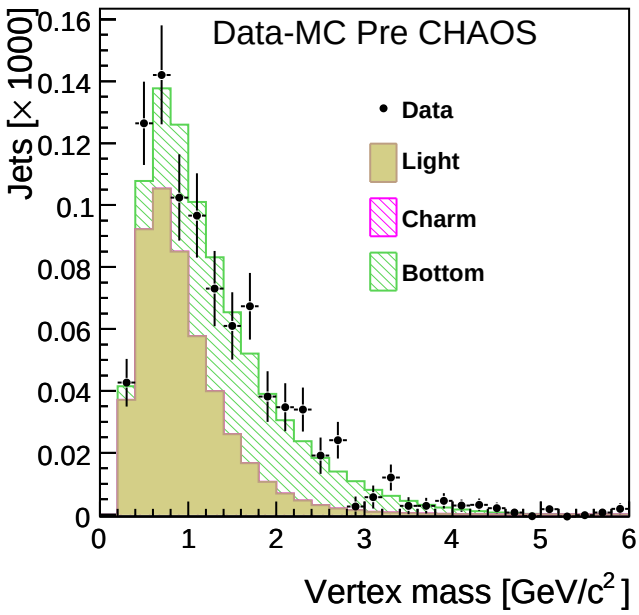

Figure 7.10: Mass of the vertex after multijet-NN cut in data subtracting all the backgrounds coming from MC. The colored histograms are flavor templates fitted to the data distribution.

and CHAOS sum of the outputs, is shown in figure 7.11. The agreement between negative tags and the template is quite good.

The values for CHAOS flavor efficiency cutting on 1.65 are:

- b-jets efficiency = 7.3%
- c-jets efficiency = 34.6%
- $light$-jets efficiency = 4.9%

Where the b-jet and c-jet efficiency comes from data (as is explain in section 5.4) and the $light$-jet efficiency comes from MC.

After the optimization process described in this section we come out with the final region as is shown in section 7.8, where the final numbers for data and predictions are summarized in Table 7.7.

As expected from a "blind search", the optimization procedure is made over the predictions. CDF II data, as shown in the figures, is plotted once the process is finished.

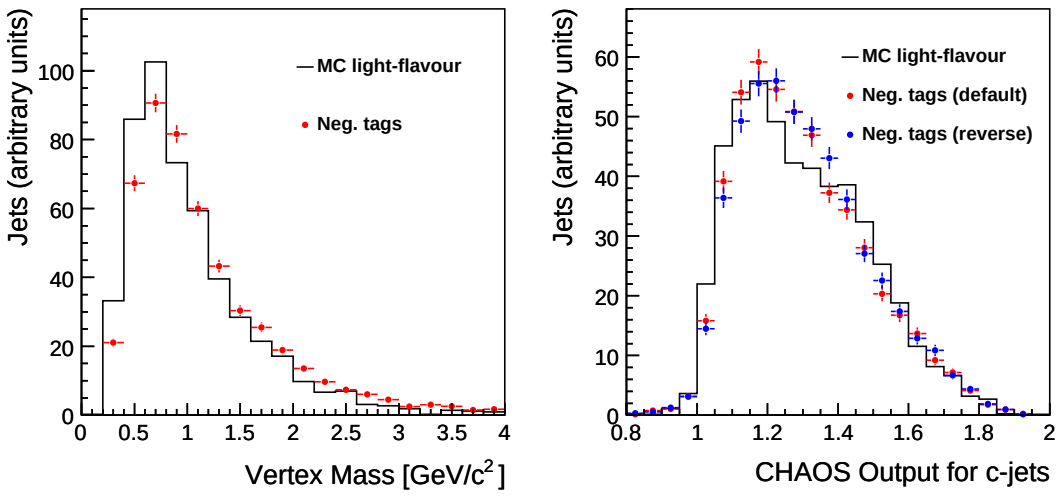

Figure 7.11: Light template from MC and negative tags from data in the vertex mass distribution (left) and CHAOS sum of the outputs (right).

7.7 Systematic Uncertainties

Systematic errors are the main source of uncertainty in this search. Some of these errors affect the overall normalization of the signal or background templates. This kind of systematic errors, so-called rate systematics, summarize effects that impact the number of events in the signal and background templates. However, the shapes of these templates are not affected by these sources of uncertainty.

Contrarily, some other systematic uncertainties make the shapes of the templates to vary. This second kind of systematic errors, named shape systematics, could also affect the overall number of events. These differences in shape are accounted for by producing sets of shifted templates in parallel to the nominal ones.

Since the shape of the various backgrounds is used to extract the final exclusion limit, the shape uncertainties in this analysis are as relevant as the rate uncertainties.

The systematic uncertainties on the signal and the background predictions, taking into account correlated and uncorrelated uncertainties, are studied.

- Jet Energy Scale [90]: A systematic error in the calorimeter energy scale affect the total transverse energy on the jets. The effect in the final region is negligible.
- Tagging Scale Factor: The difference between data and MC in c-tagging efficiency (10%) is taken as systematic uncertainty. The resulting uncertainty in the final region is 3.6%.
- CHAOS Scale Factor: The difference between data and MC is taken as systematic uncertainty. The resulting uncertainty in the final region is 9.2%.
- Mistag estimation: The systematic error assigned to the tag rate matrix is 4.8%.
- Luminosity: The systematic uncertainty in the luminosity is taken to be 6%, affecting to the normalization of all the MC estimated backgrounds.
- ISR/FSR: The uncertainty associated with the initial and final state radiation was evaluated by generating sample with more/less ISR/FSR. The effect in the final region is 1.7%.
- PDF: The PDF uncertainty has been determined to be 3.8% on the acceptance.
- HF QCD Multijet Background: We assign a conservative 30% uncertainty in the prediction based on the variation observed when matrix definition is changed.

- Top-Pair Production cross section: We quote the uncertainty in the CDF measured value (11%) of the top-pair production cross section.
- Single Top Production cross section: We quote the theoretical uncertainty in the single-top cross section (13%).
- Diboson Production cross section: We quote the theoretical uncertainty being 10% in the WW and WZ cross sections and 20% for the ZZ process.
- Single EWK Boson Production cross section: Although the cross section for Z and W production are known to a high precision, we are using the heavy flavor processes in ALPGEN to perform estimations of Z/W+multijet processes. Because of this, we estimate a 40% uncertainty in the predictions.
- Top quark mass: In the current analysis, the $t\bar{t}$ production background is estimated using MC with a top quark mass of 175 GeV/c^2. Since our signal optimization is based on a Neural Network trained with $t\bar{t}$ processes we include a systematic error due to the top pair NN output dependence on the top quark mass. We compute this error measuring the number of top-pair events in the final selection by using a top quark mass of 172.5 GeV/c^2.
- Differences in shape between ALPGEN and PYTHIA: We include a shape systematic uncertainty in the final selections due to the differences between ALPGEN and PYTHIA generators used to estimate the Z/W + jets processes.
- HF QCD Multijet and mistag estimation after CHAOS: We quote the uncertainty in the final region due to this estimations of 3.6% and 8.2% respectively.

7.8 Results

In the final signal region the number of observed events is in good agreement with the expectations from the SM processes, as summarized in Table 7.7. The uncertainty on the total expected number of events was computed taking into account the anti-correlations among the several background contributions. Kinematic distributions in the signal region are checked. $\not\!\!E_T$, $\mathrm{E}_{T,j1}$, $\mathrm{E}_{T,j2}$, and η_{j1} distributions are shown in figure 7.13.

Since no significant deviation from the SM prediction is observed, the result is used to calculate an exclusion limit for the cross section of the described stop process. We find the

CDF Run II Preliminary 2.6 fb^{-1}

	Signal Region
W/Z + jets production	60.9 ± 26.6
Diboson production	10.7 ± 1.9
Top pair production	4.6 ± 1.3
Single top production	3.2 ± 0.8
HF QCD Multijets	20.4 ± 15.2
Light-flavour contamination	32.2 ± 12.7
Total expected	132.0 ± 24.4
Observed	115
Signal m($\tilde{t}$)=125, m($\tilde{\chi}^0$)=70	90.2 ± 23.9
Signal m($\tilde{t}$)=135, m($\tilde{\chi}^0$)=70	78.0 ± 20.7
Signal m($\tilde{t}$)=115, m($\tilde{\chi}^0$)=70	82.4 ± 21.8

Table 7.7: Number of expected and observed events in the signal region. Predictions for the signal points are also shown. Correlated and uncorrelated uncertainties in the total background and expected signal were treated separately in the analysis although they are combined here.

output of the multijet-NN, in the region (0,1), after applying CHAOS (figure 7.12), as the best discriminant to extract a limit using shapes. We perform a likelihood fit to set a 95% C.L. limit in the production cross section as it is shown in figure 7.14, as a function of the stop-pair production cross section for given value of the neutralino mass.

For the assumed model, the sensitivity of the analysis is able to exclude $\tilde{t}$ masses up to 180 GeV/c^2 at 95 % C.L. In addition, using the assumed model, a 95% C.L. limit was obtained in the mass parameter plane of the model. Figure 7.15 shows the excluded region in the stop-neutralino mass plane of the analysis, compared with results from previous analyses [107, 106].

Currently the limit obtained with the present analysis clearly improves the results of previous searches using similar topology.

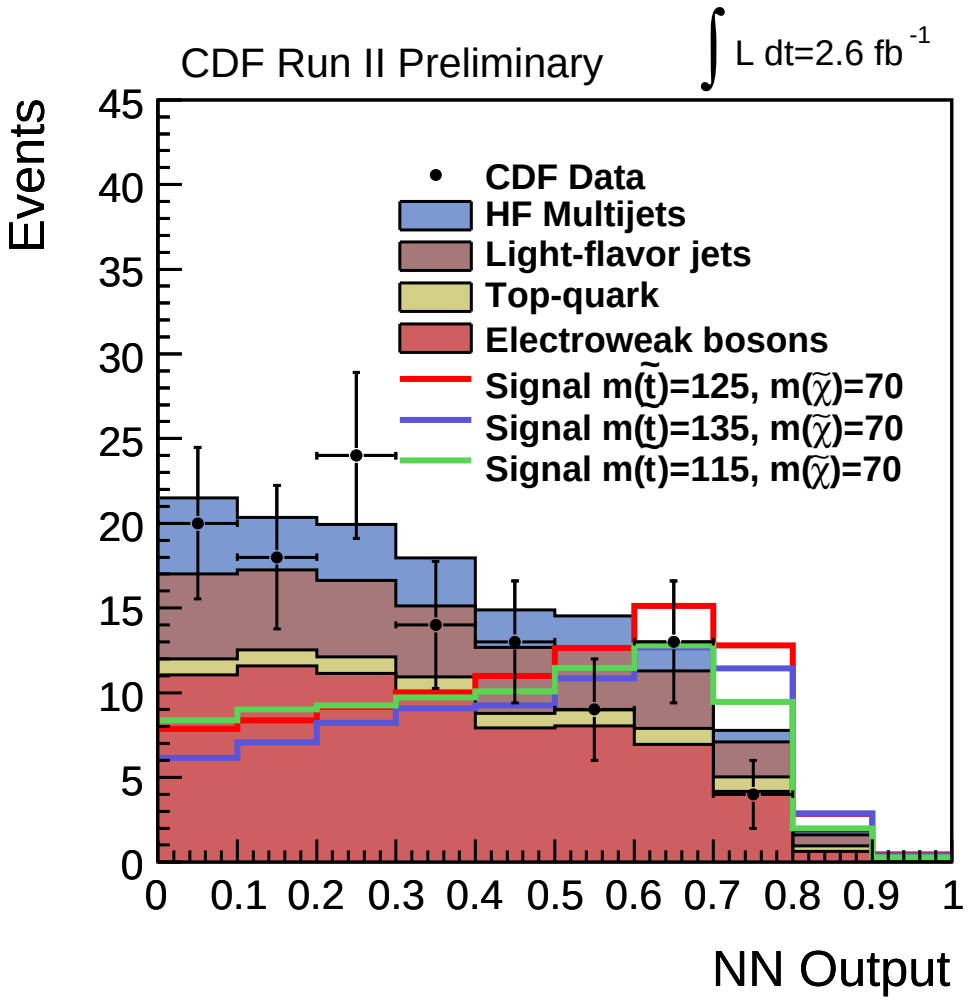

Figure 7.12: Observed final discriminant used to extract the limits from the shapes comparison.

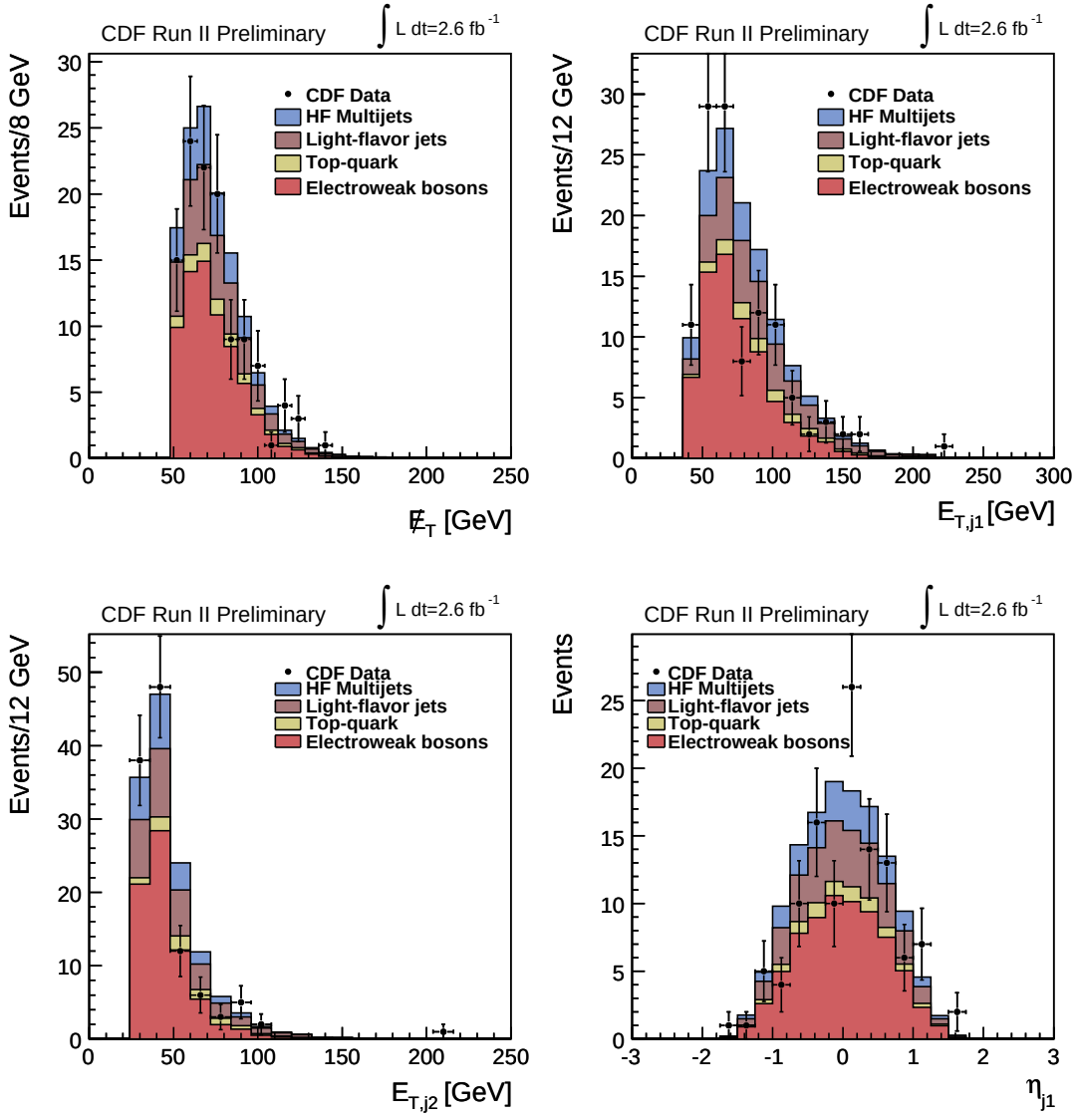

Figure 7.13: $\not\!\!E_T$, first jet E_T, second jet E_T, and first jet η in the final region.

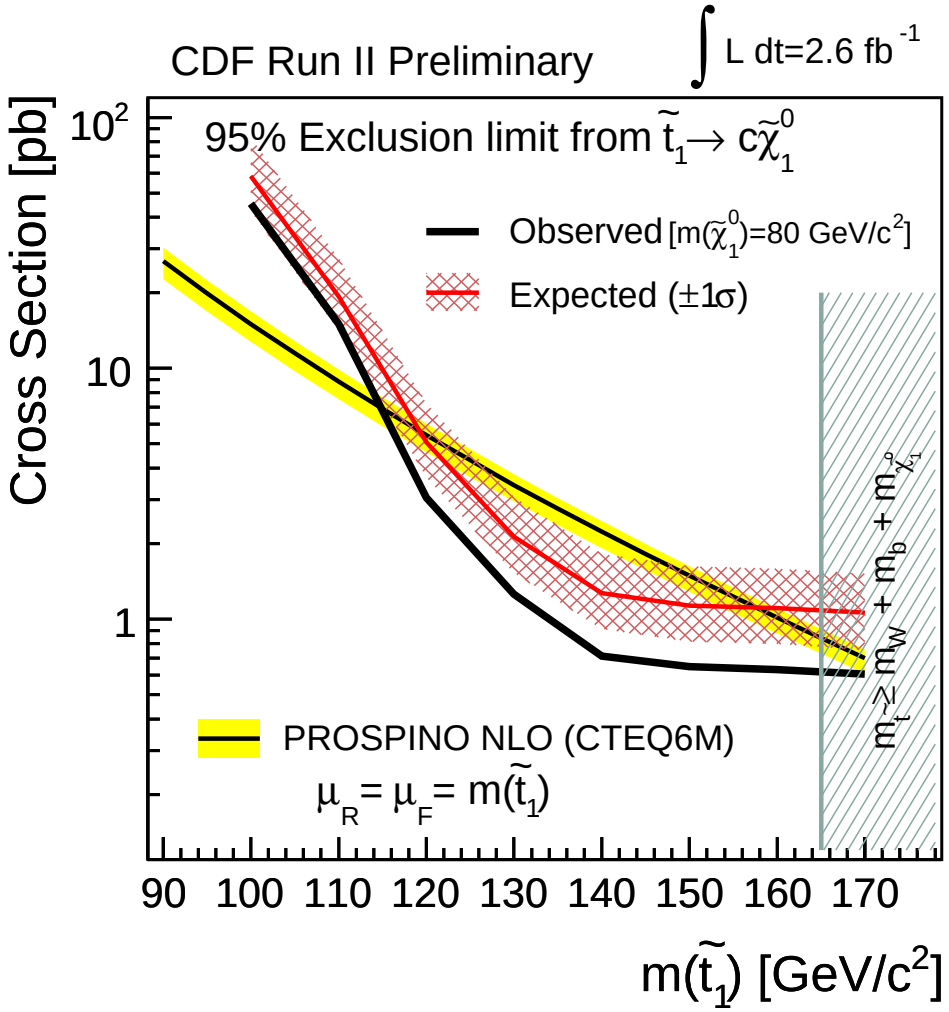

Figure 7.14: Observed 95% C.L. limit in terms of cross section for a m($\tilde{\chi}^0$) = 80 Gev/c^2 (black line) and expected limit (red line) with 1σ uncertainty band. The region where the branching ratio assumed for the analysis is no longer valid is also shown.

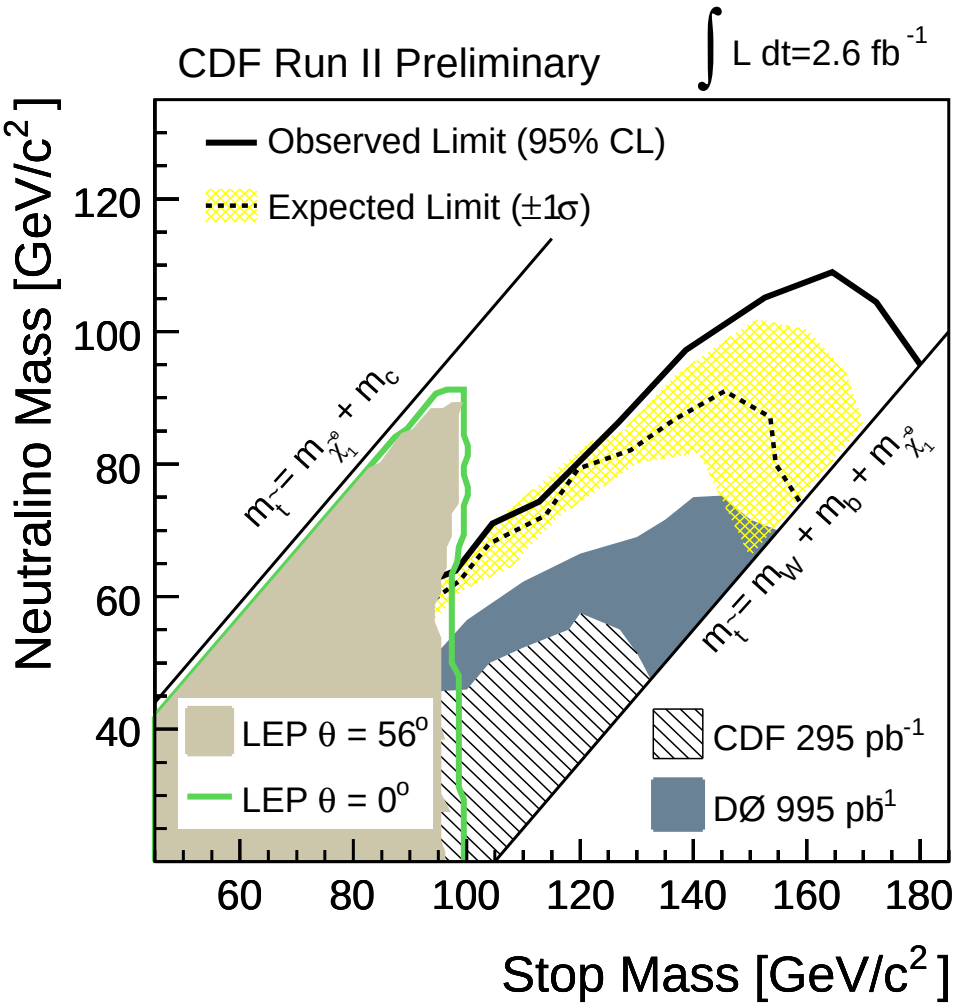

Figure 7.15: Excluded region at 95% C.L. in the $m(\tilde{\chi}^0)$-$m(\tilde{t})$ plane assuming R-parity conservation. The result is compared to the previous results from CDF [106], DØ [107], and LEP [108].

Chapter 8

Conclusions

Two different searches for third generation squarks in the $\not\!\!E_T$ plus jet sample have been performed. Since no significant deviation from the SM prediction is observed, the results have been used to calculate 95% C.L. exclusion limits for the cross section of the two SUSY processes.

The sensitivity achieved by these analyses is based on the robustness of the background descriptions and the strength of the signal optimization techniques. In these two aspects, special credit is due to the MUTARE method, to estimate the heavy flavor multijet background from data, and the CHAOS flavor separator. Developed for the analyses presented in this theses, these tools have moreover a broad spectrum of application in searches and measurements among the physics program.

The only experiment, up to now, capable of performing comparable searches is DØ . The stop search was performed by DØ achieving a sensitivity that provides a smaller excluded region, due partially to the smaller dataset used.

The Tevatron SUSY search program will be crucial in the next years, even with the beginning of the LHC program in the incoming months. In particular, scenarios where the third generation squarks are assumed to be very light, as the ones presented in this theses, remain important at the Tevatron energy scale. However, the conquest of the Terascale with the imminent LHC, will be the biggest challenge in the coming years. The work presented in this theses is made with two intentions: exploring the Tevatron's energy frontier searching for new physics, and keep improving the analysis techniques to get ready for the LHC data. Both intentions become real as described in the present theses, setting world best exclusion limits in the performed searches, and successfully developing and implementing new analysis techniques.

Appendix A

Performance of the NN in the Search for Gluino-mediated Bottom Squark

Two different neural networks are used during the optimization process in the search for gluino-mediated bottom squark. One of them is made to remove the HF multijet background and the other one to remove the top par production background.

The same set of variables are used in the multijet-NN and top-NN. Depending on the optimization, large or small Δm, the set of variables is different due to the cut on number of jets applied in each selection. All the variables are well modeled and are found as the ones providing the best separation power.

A.1 Multijet Neural Network

The variable used during the training of the multijet-NN for the large and small Δm optimization are shown in figures A.1 and A.2 comparing the signal and background.

The output of the neural networks for the two optimizations is shown in figure A.3 with training and test events.

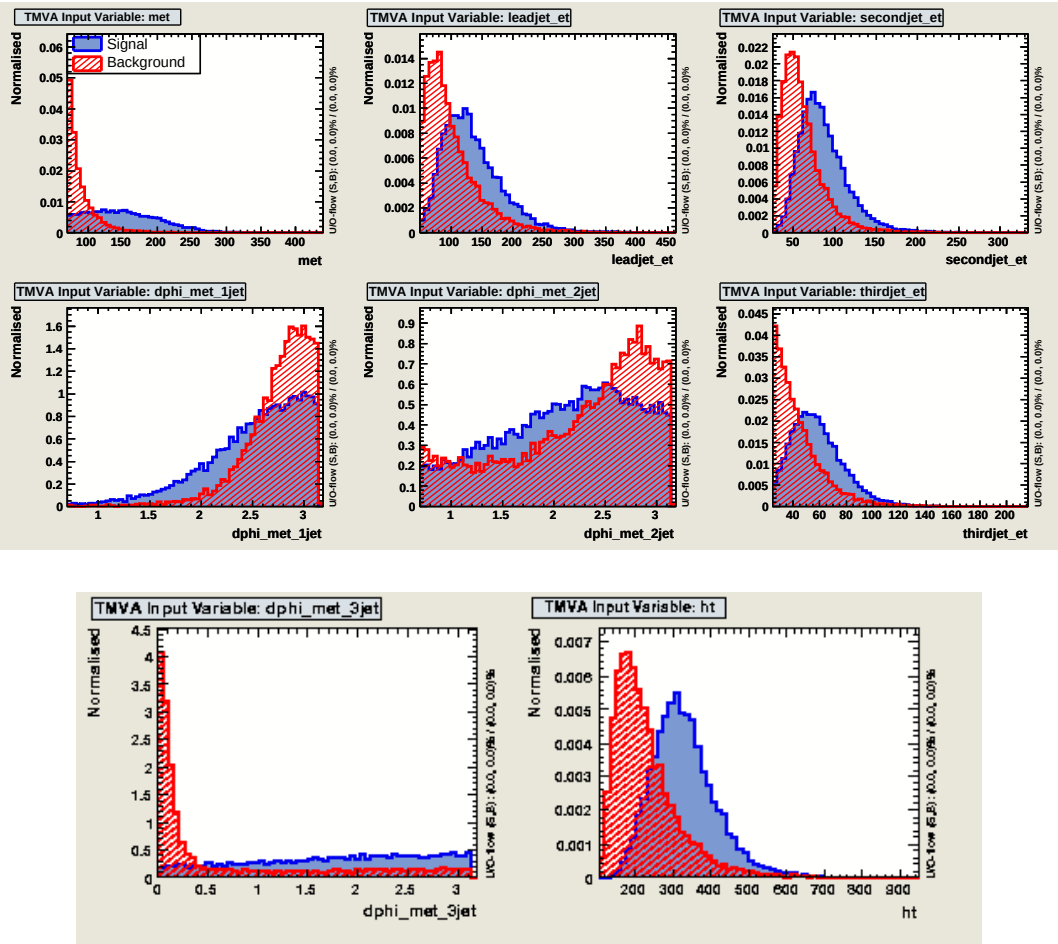

Figure A.1: Input variables used for the multijet-NN training in the large Δm optimization. Signal is plotted in blue and background (taggable jets) in red.

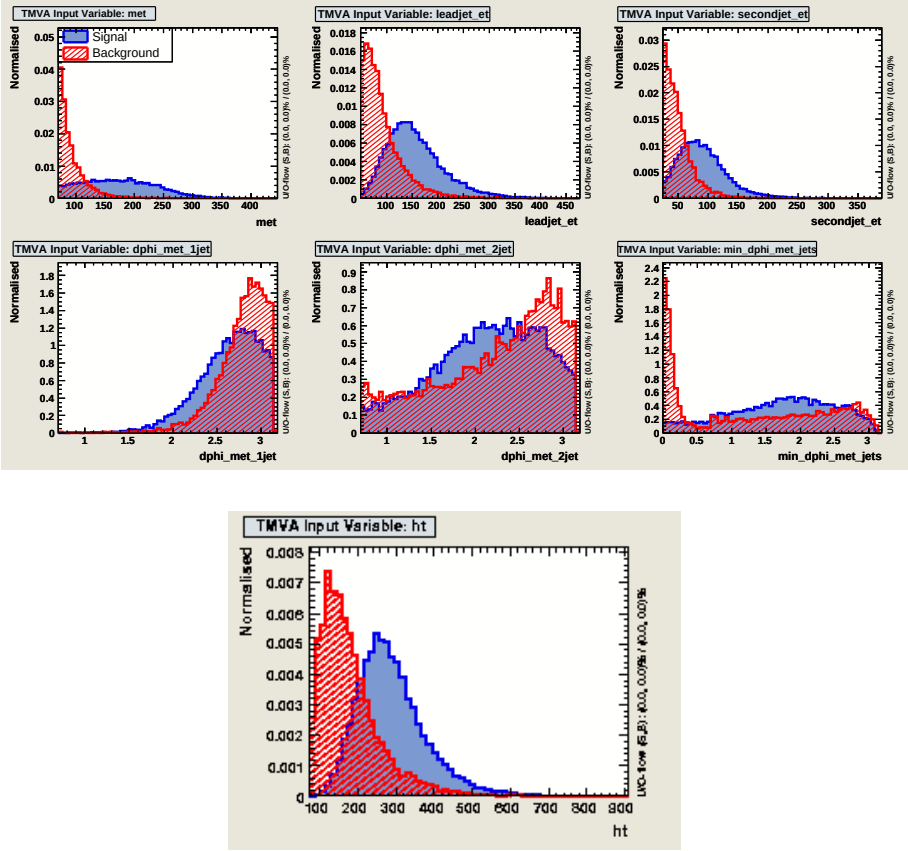

Figure A.2: Input variables used for the multijet-NN training in the small Δm optimization. Signal is plotted in blue and background (taggable jets) in red.

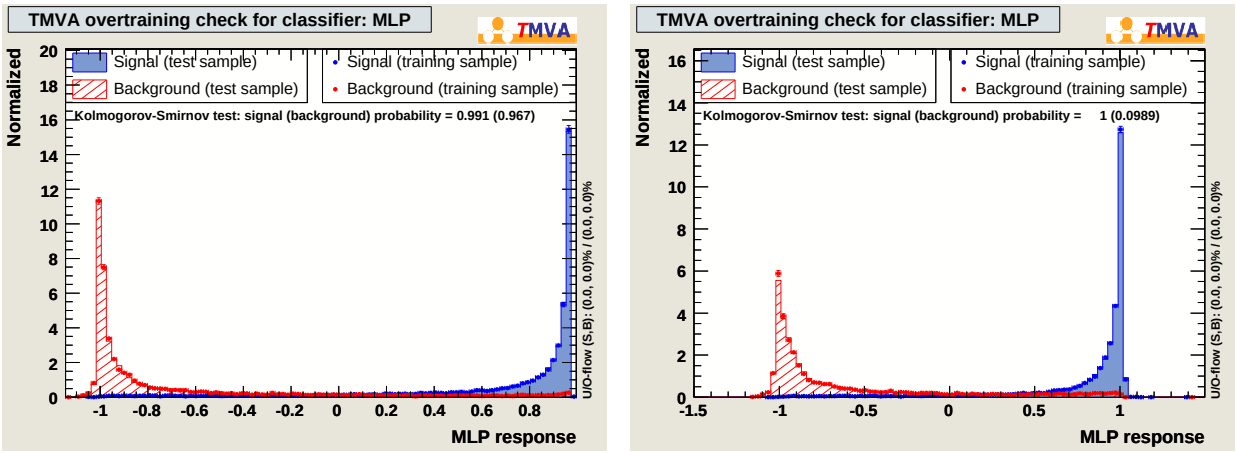

Figure A.3: Multijet-NN training and test output for the large Δm optimization (left) and small Δm optimization (right).

A.2 Top Neural Network

The variable used during the training of the top-NN for the large and small Δm optimization are shown in figures A.4 and A.5 comparing the signal and background.

The output of the neural networks for the two optimizations is shown in figure A.3 with training and test events.

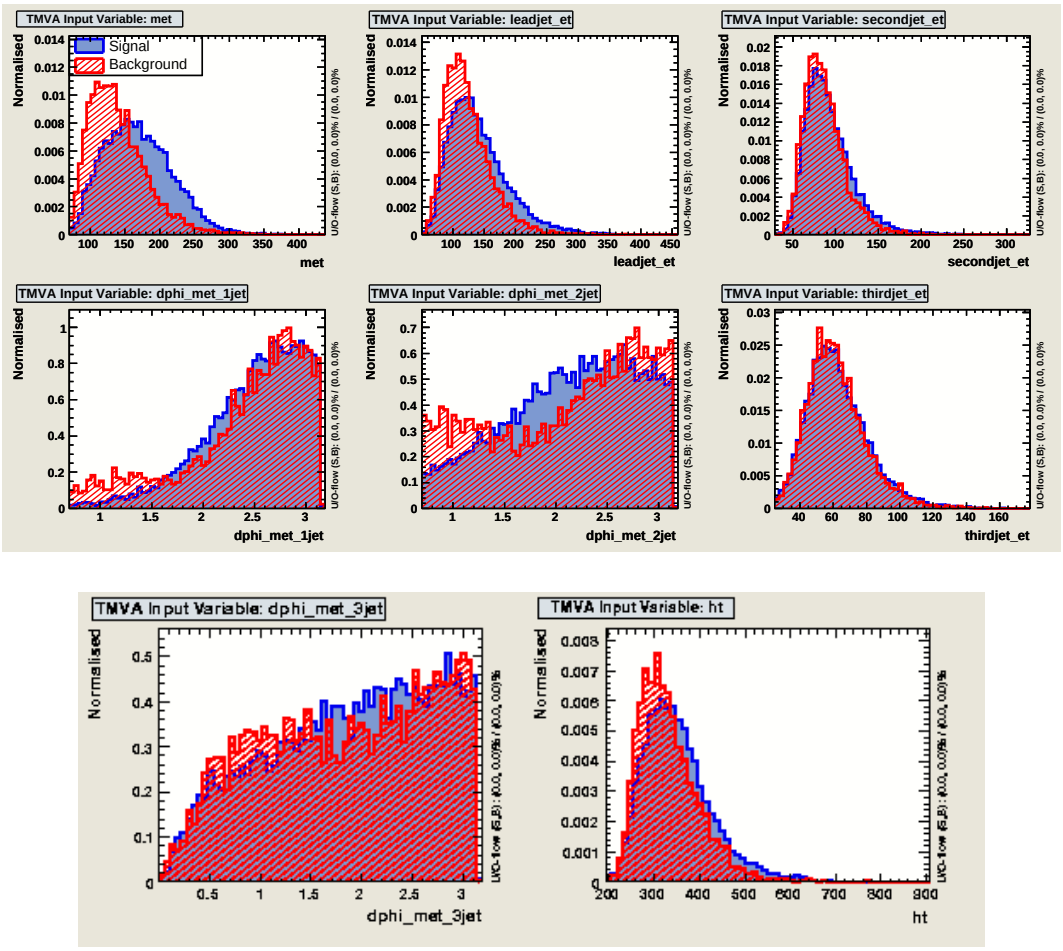

Figure A.4: Input variables used for the top-NN training in the large Δm optimization. Signal is plotted in blue and background (top pair production) in red.

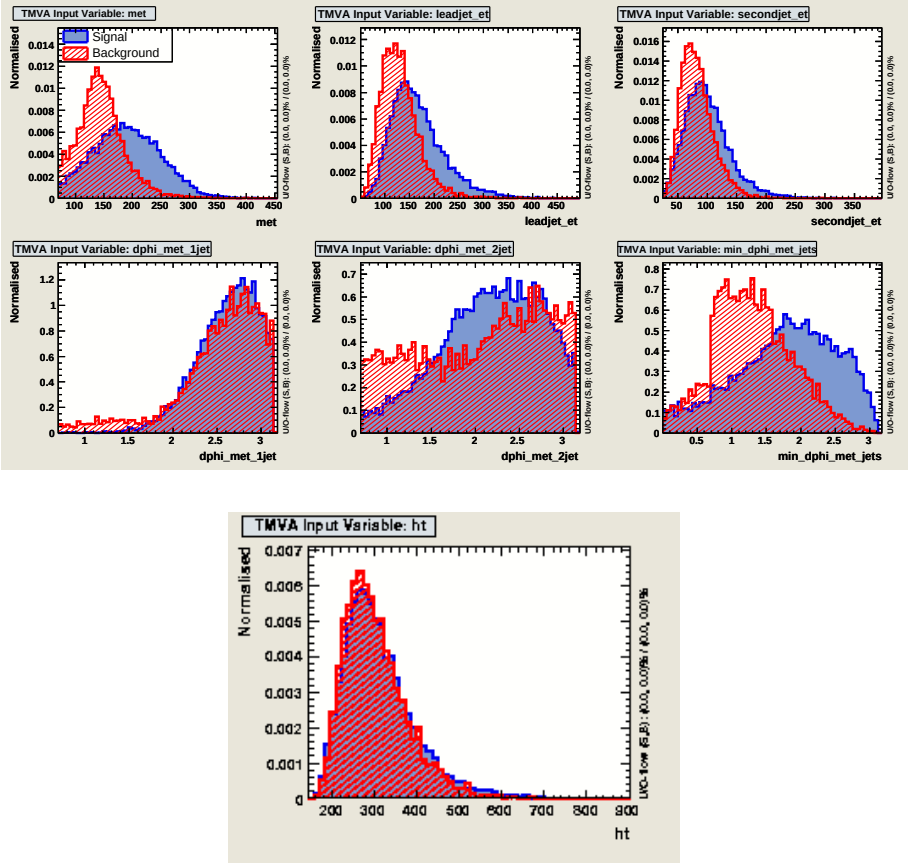

Figure A.5: Input variables used for the top-NN training in the small Δm optimization. Signal is plotted in blue and background (top pair production) in red.

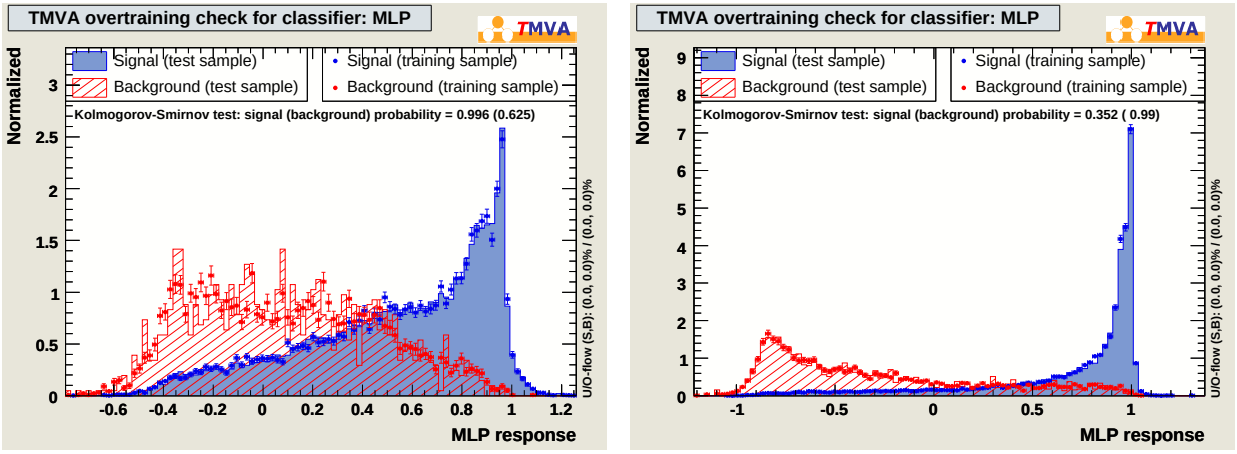

Figure A.6: Top-NN training and test output for the large Δm optimization (left) and small Δm optimization (right).

Appendix B

Performance of the NN in the Search for Scalar Top Decaying into $c + \tilde{\chi}^0$

A neural network is used during the optimization process in the search for scalar top decaying into charm and neutralino. The neural network is made to remove the HF multijet background. All the variables are well modeled and are found as the ones providing the best separation power, as shown in figure B.2.

The output of the neural network is shown in figure B.1 with training and test events.

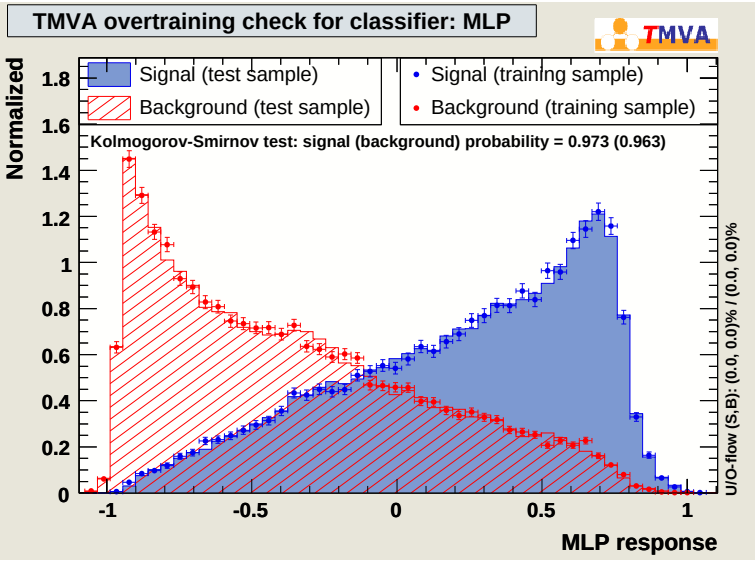

Figure B.1: Multijet-NN training and test output.

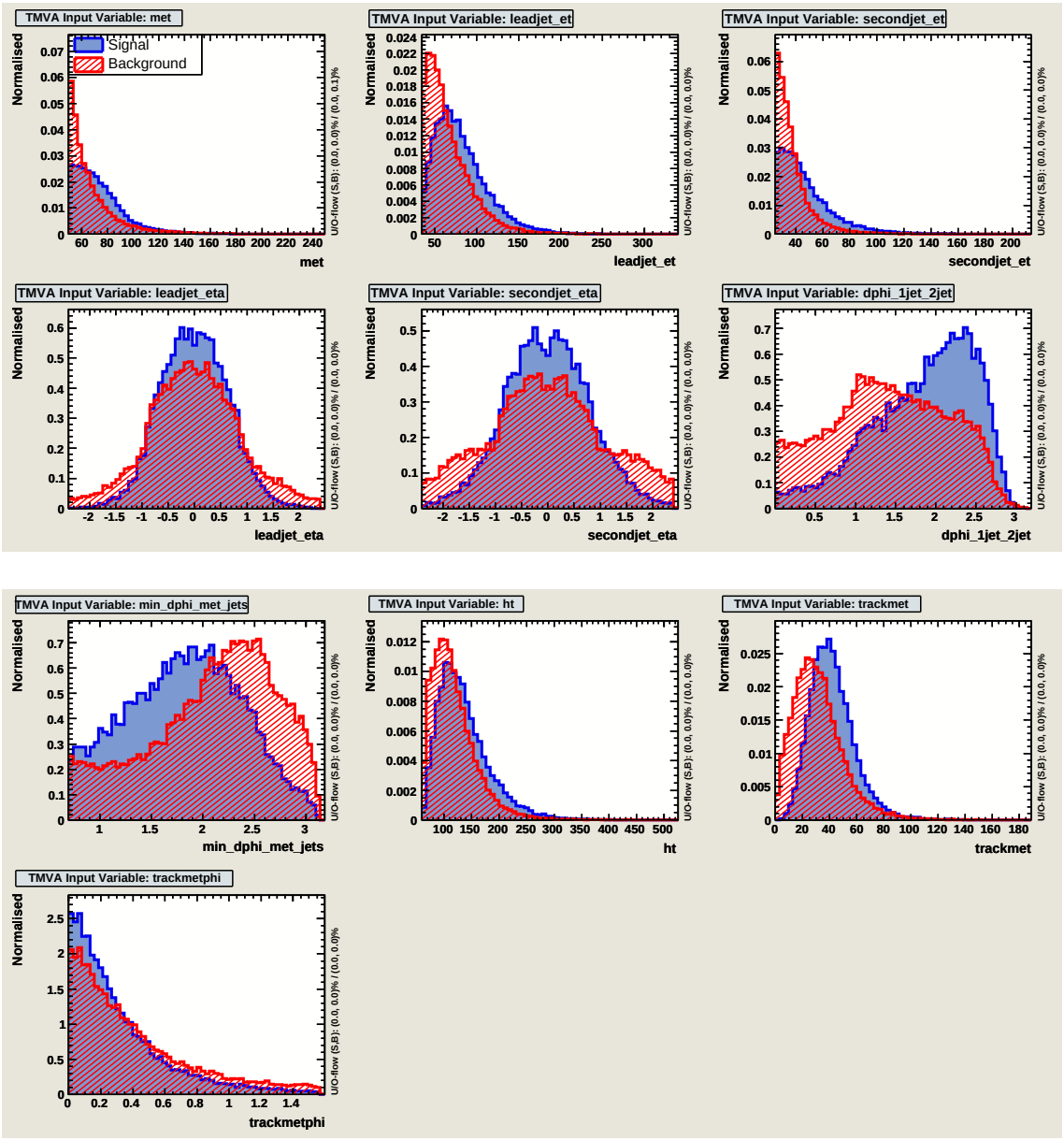

Figure B.2: Input variables used for the training of the multijet-NN

Appendix C

Alpgen vs Pythia Comparison in the Search for Scalar Top Decaying into $c + \tilde{\chi}^0$

The search for scalar top decaying into charm and neutralino is perform using ALPGEN generator to predict the $W/Z+$ jets background, as described in Chapter 7. However, we also run the whole analysis using PYTHIA event generator. The ALPGEN prediction is used as the nominal estimation while the PYTHIA prediction is used as a cross check. Differences in shape between the two Monte Carlo estimations are taken as systematic uncertainties.

This comparison between Monte Carlo generators is made with the analysis selection and is not intended to compare the two Monte Carlo themselves. The goal of this comparison is to see how sensitive we are to differences between both generators.

The figures in this appendix are the same as the ones shown in Chapter 7 but using PYTHIA instead of ALPGEN for the $W/Z+$ jets prediction. This means that the differences are only present in the red histogram labeled as Electroweak bosons.

Figures C.1,C.2, and C.3 show the leading jet E_T and $\not\!\!E_T$ in the three control regions defined in the analysis.

Figure C.4 shows the output of the multijet-NN, and figure C.5 shows the neural network output in the region (0,1) after CHAOS application. The latter plot is used to extract a shape systematic uncertainty used to compute the final limit.

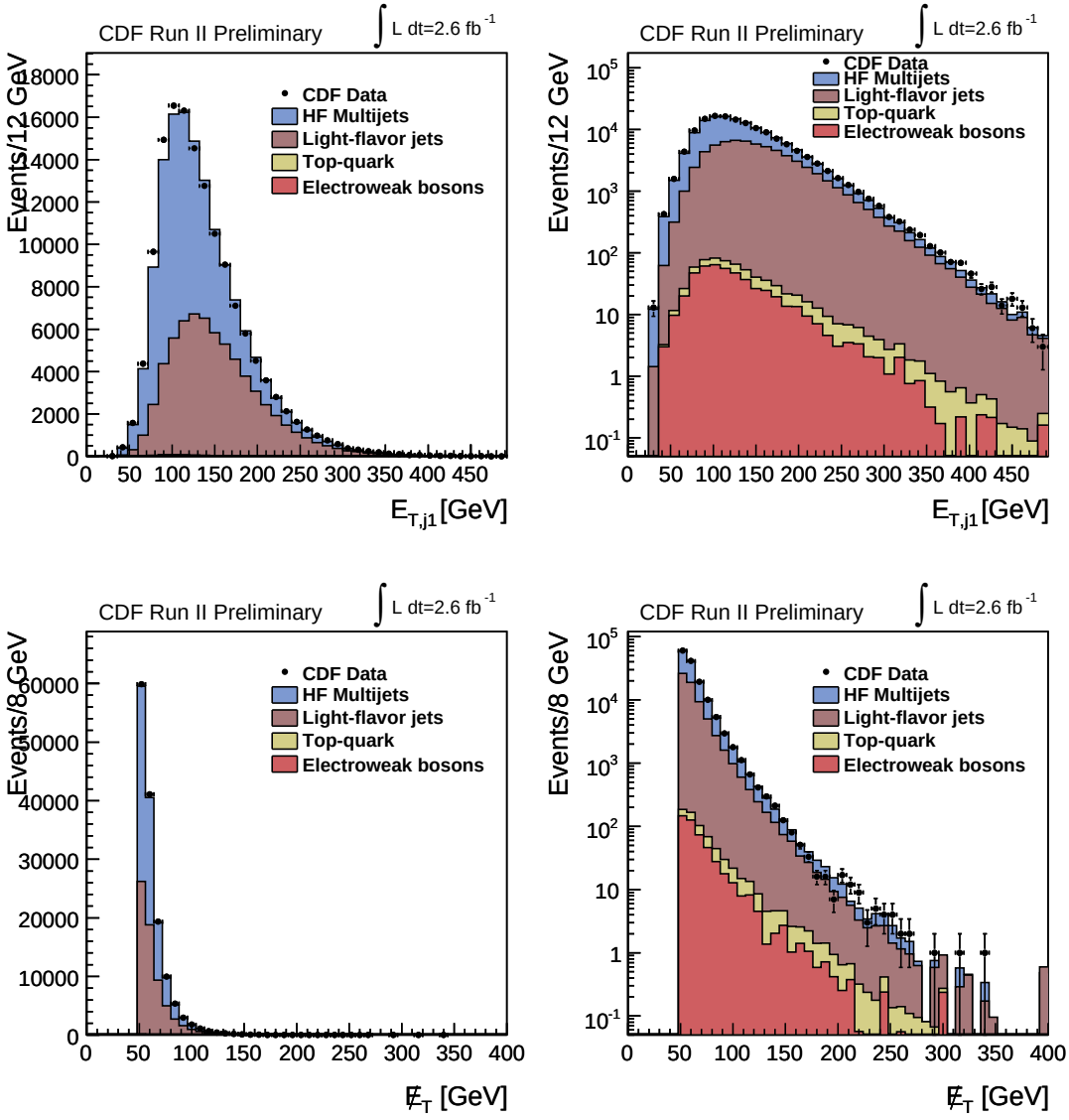

Figure C.1: Leading jet E_T and $\not\!\!E_T$ in linear (left) and logarithmic (right) scales in the HF multijet control region.

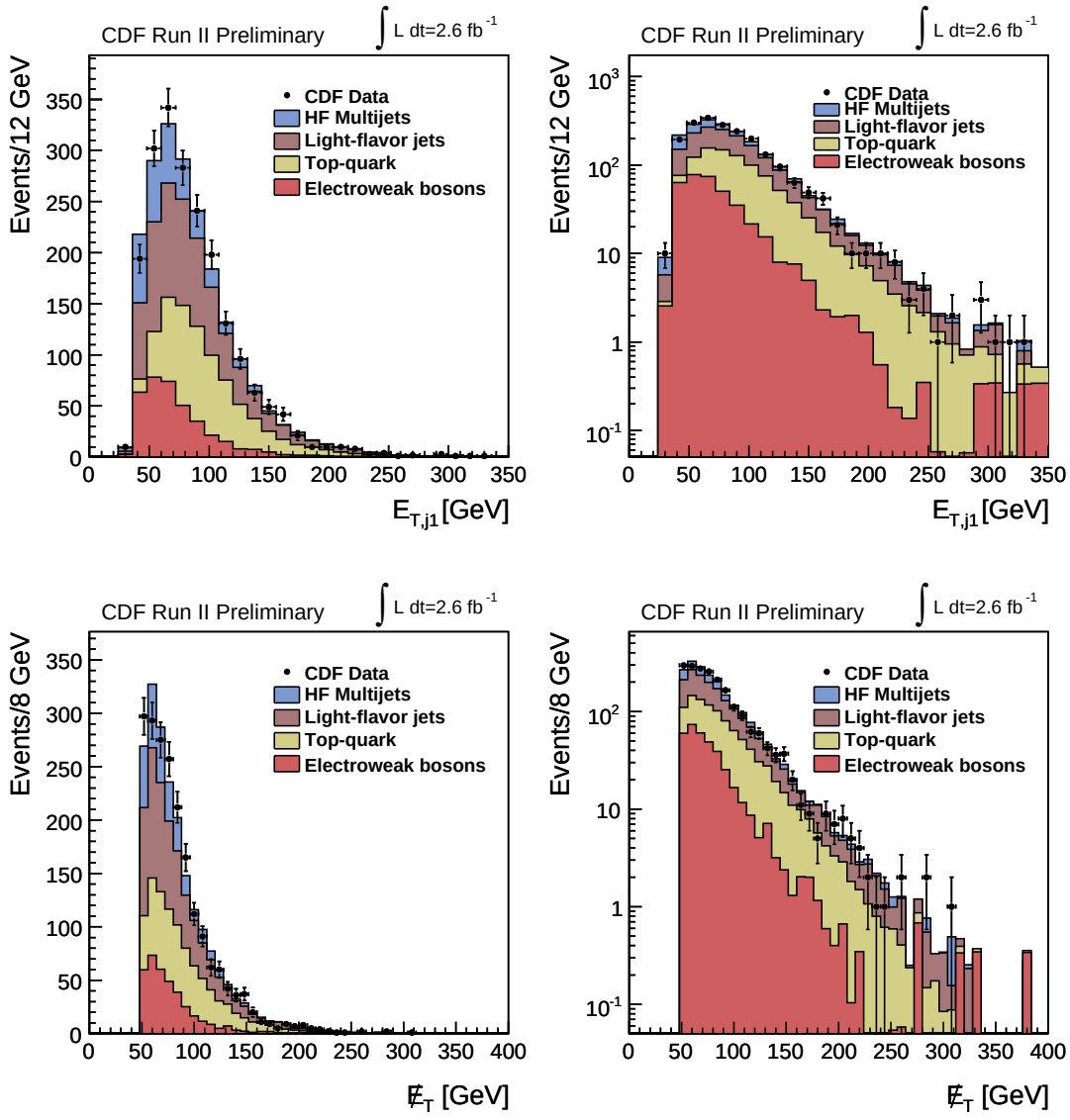

Figure C.2: Leading jet E_T and $\not\!\!E_T$ in linear (left) and logarithmic (right) scales in the lepton control region.

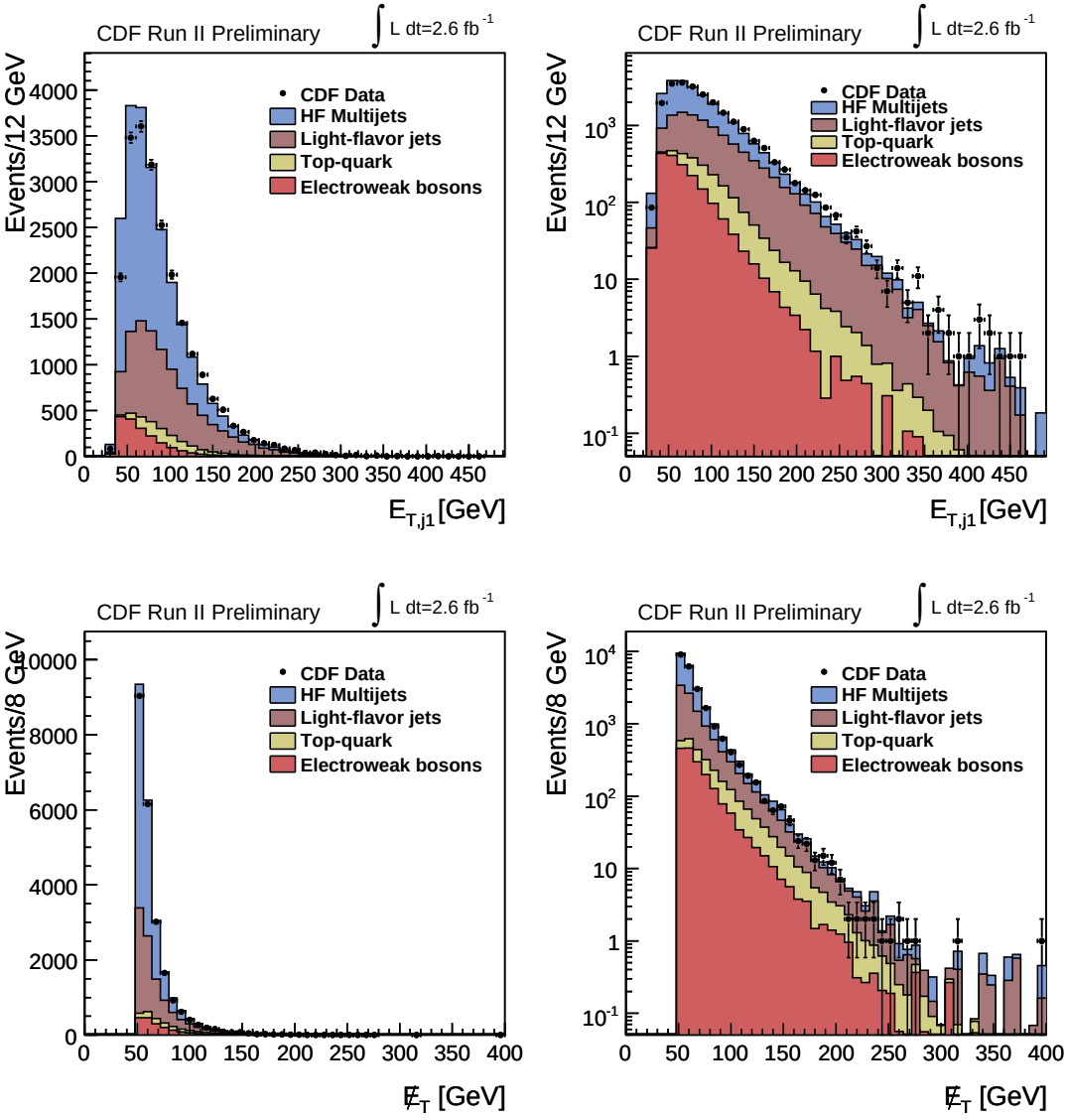

Figure C.3: Leading jet E_T and $\not\!\!E_T$ in linear (left) and logarithmic (right) scales in the pre-optimization control region.

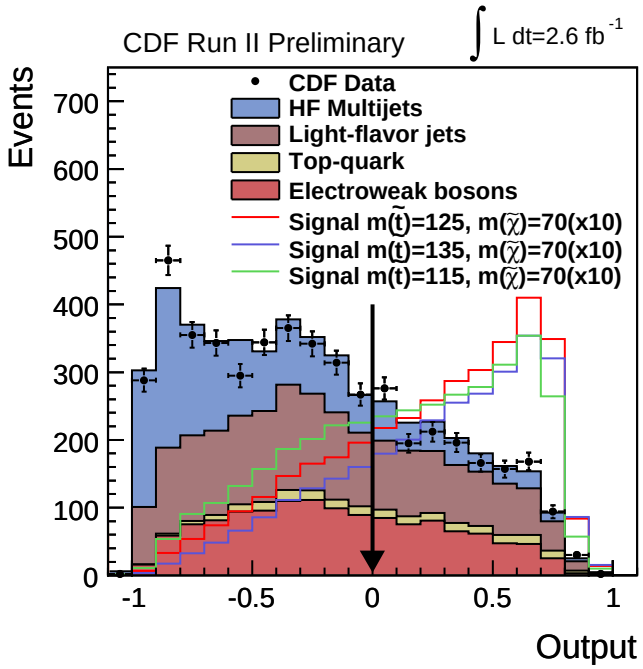

Figure C.4: Output of the NN to reject HF multijet background. The arrow indicates the cut applied in the analysis.

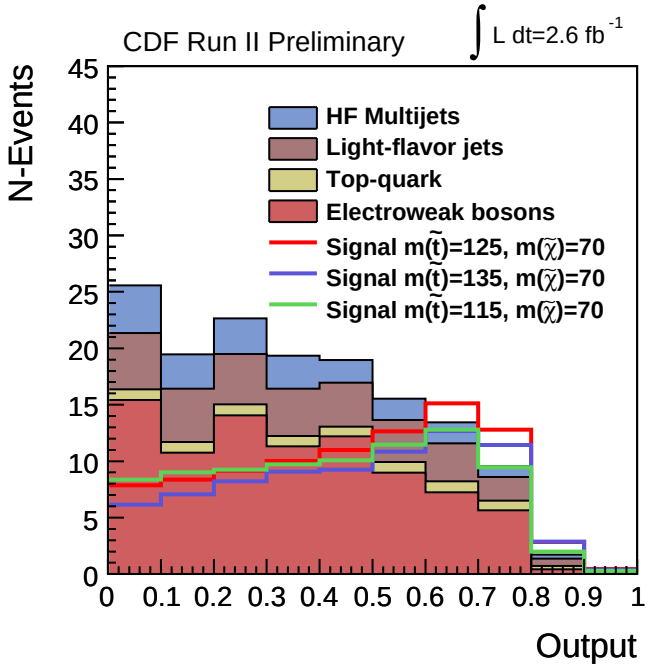

Figure C.5: Observed final discriminant used to extract the limits from the shapes.

Appendix D

Resumen en castellano

El Modelo Estándar (ME) de las partículas elementales ha demostrado ser una de las descripciones más precisas de la Naturaleza. El modelo, incluye las interacciones electromagnética, débil y fuerte, construyendo el Lagrangiano para describirlas desde principios de simetría.

En el marco del Modelo Estándar hay dos tipos de constituyentes fundamentales de la naturaleza: bosones y fermiones. Los bosones son las partículas responsables de intercambiar las interacciones entre los fermiones, que son los constituyentes de la materia. Los fermiones se dividen en seis quarks y seis leptones, formando una estructura de tres familias. Cada fermión y bosón así definido, tiene ademas su antipartícula.

A pesar del su éxito, varias dificultades apuntan a que el Modelo Estándar es una teoría válida a baja escala de energías. Sus limitaciones incluyen la dificultad de introducir la gravedad y la falta de justificación para el ajuste fino de algunas correcciones perturbativas. Ademas, algunos aspectos de la teoría no están entendidos, como el espectro de masas o el mecanismo de rotura de la simetría electrodébil.

Como respuesta a las carencias del Modelo Estándar nace la Supersimetría (SUSY), un nuevo marco teórico que solventa los citados problemas, manteniendo intacto el poder predictivo de la teoría. La SUSY introduce una nueva simetría que relaciona un nuevo bosón con cada fermión del ME y un nuevo fermión con cada bosón del ME. De esta forma, para cada bosón existente en el ME, debería existir un súper compañero fermiónico (denotado con el sufijo ino), y de la misma forma, para cada fermión existente en el ME, debería existir un súper compañero bosónico (denotado con el prefijo s). Además, se suele introducir otra simetría, llamada paridad R para prevenir interacciones con violación de numero bariónico y leptónico. Asumiendo conservación de paridad R, las súper partículas solo pueden ser producidas en pares y no pueden

desintegrarse completamente en partículas del ME. Este último punto implica la existencia de la partícula supersimétrica más ligera, que proporciona un candidato para materia oscura, como sugieren datos astrofísicos.

Tevatron es un colisionador hadrónico situado en Fermilab, EEUU. Este acelerador produce colisiones protón-antiprotón con una energía en el centro de masas de $\sqrt{s}$=1.96 TeV. En uno de los dos puntos de colisión del Tevatron, se encuentra CDF, un detector construido para analizar las colisiones producidas por el acelerador.

Introducción teórica

El Modelo Estándar de las partículas es un teoría cuántica de campos que ha demostrado describir muchos resultados experimentales con un nivel de precisión sin precedentes.

Basada en varias simetrías de grupos, el Modelo Estándar incluye las interacciones electromagnética, débil y fuerte. Los constituyentes básicos de la Naturaleza, de acuerdo con el Modelo Estándar, son un conjunto de fermiones y bosones. Los fermiones son los responsables de la materia, mientras que los bosones son los mediadores de las interacciones.

El sector fermiónico agrupa seis quarks, seis leptones y sus respectivas antipartículas, divididos en tres familias. Los miembros de esas familias son idénticos en todos los observables excepto por la masa. Nuestro mundo más inmediato está hecho con partículas de la primera familia: el quark u y d que forman los protones y neutrones de los núcleos y los electrones, y sus neutrinos asociados, como se mustra en la Tabla D.1. Las partículas de las otras dos familias son mas masivas y se desintegran rápidamente en partículas de la primera familia.

	1^{st} Generation	2^{nd} Generation	3^{rd} Generation
quarks	Up (u) 1.5-3.0 MeV/c^2	Charm (c) 1.25±0.09 GeV/c^2	Top (t) 173.1±1.3 GeV/c^2
	Down (d) 3.0-7.0 MeV/c^2	Strange (s) 95±25 MeV/c^2	Bottom (b) 4.20±0.07 GeV/c^2
leptons	Electron neutrino (ν_e) < 2 eV$/c^2$	Muon neutrino (ν_μ) < 0.19 MeV$/c^2$	Tau neutrino (ν_τ) < 18.2 MeV$/c^2$
	Electron (e) 0.511 MeV/c^2	Muon (μ) 105.66 MeV/c^2	Tau (τ) $1776.99^{+0.29}_{-0.26}$ MeV$/c^2$

Table D.1: El sector fermiónico del Modelo Estándar.

Las interacciones de los fermiones están mediadas por los constituyentes bosónicos del Modelo Estándar. Estos bosones llevan las fuerzas fundamentales derivadas de las simetrías, como se resume en la Tabla D.2.

Interacción	Partícula	Masa
electromagnética	fotón, γ	0
fuerte	gluón, g	0
débil	$W^{\pm}$	80.403±0.029 GeV/c^2
	Z^0	91.188±0.002 GeV/c^2

Table D.2: Los bosones de gauge del Modelo Estándar y sus interacciones.

Sin embargo, incluso si la gravedad es la interacción que ha sido conocida por mayor tiempo y es la más cercana a nuestra vida cotidiana, todavía no ha sido incluida satisfactoriamente en el marco del Modelo Estándar. Este es uno de los mayores argumentos en contra del Modelo Estándar como una teoría del todo, sugiriéndose de esta manera que debería existir una teoría más general. Esta nueva teoría debería incluir todas las simetrías del Modelo Estándar y simultáneamente aceptar esta cuarta interacción.

Incluso aceptando las peculiaridades del Modelo Estándar, este contiene por lo menos 19 parámetros libres, como acoplos, masas y mezclas, los cuales no están predichos pero deben ser medidos por los experimentos. Además, más parámetros serían necesarios si uno quiere acomodar observaciones que no proceden de la física de aceleradores, como la asimetría bariónica en cosmología, las masas de los neutrinos y sus mezclas.

El Modelo Estándar deja además varias cuestiones sin responder como por qué hay tres generaciones, dimensiones espaciales o colores, como entender las oscilaciones de los neutrinos, por qué son las cargas eléctricas del protón y del electrón exactamente opuestas o si el mecanismo de Higgs es realmente el proceso que a través del cual se produce la rotura electrodébil de la simetría. Además, el modelo no puede explicar cuales son los mecanismos para producir la asimetría de materia anti-materia observada en el universo, o cual es la relación entre las fuerzas fuerte y electrodébil. Quizás, la propiedad más sorprendente del Modelo Estándar es su precisa descripción de las interacciones entre partículas con masas 17 ordenes de magnitud menores que la escala de la masa Planck.

Para dar solución a estos problemas uno de los modelos más populares es el conocido como Supersimetría, un nuevo marco teórico que solventa los citados problemas, manteniendo intacto

el poder predictivo de la teoría. La SUSY introduce una nueva simetría que relaciona un nuevo bosón con cada fermión del ME y un nuevo fermión con cada bosón del ME. De esta forma, para cada bosón existente en el ME, debería existir un súper compañero fermiónico (denotado con el sufijo ino), y de la misma forma, para cada fermión existente en el ME, debería existir un súper compañero bosónico (denotado con el prefijo s). Además, se suele introducir otra simetría, llamada paridad R para prevenir interacciones con violación de numero bariónico y leptónico. Asumiendo conservación de paridad R, las súper partículas solo pueden ser producidas en pares y no pueden desintegrarse completamente en partículas del ME. Este último punto implica la existencia de la partícula supersimétrica más ligera, que proporciona un candidato para materia oscura, como sugieren datos astrofísicos.

Esta tesis presenta dos búsquedas de squarks de la tercera familia. En el marco de la Superimetría y en particular en su mínima extensión, el MSSM, se espera una gran mezcla de los estados de masa dependiendo de ciertos parámetros de la teoría: $\tan\beta$ y $A_{t,b}$.

En particular para el caso del $\tilde{b}$, la masa de este squark podría ser significativamente más pequeña que la masa de los otros squarks:

$$m^2_{\tilde{b}_{1,2}} = \frac{1}{2}[m^2_{\tilde{b}_L} + m^2_{\tilde{b}_R} \pm \sqrt{(m^2_{\tilde{b}_L} - m^2_{\tilde{b}_R})^2 + 4m^2_b(A_b - \mu tan\beta)^2}] \tag{D.1}$$

Además, la sección eficaz de producción de gluino es casi un orden de magnitud mayor que la del sbottom de una masa similar. A las energías alcanzadas en Tevatron, los gluinos se producen principalmente a través de aniquilación quark-antiquark y fusión de gluones, figure D.1. Si el sbottom es sufientemente ligero, entonces la desintegración a dos cuerpos $\tilde{g} \to b\tilde{b}$ estaría cinemáticamente permitida.

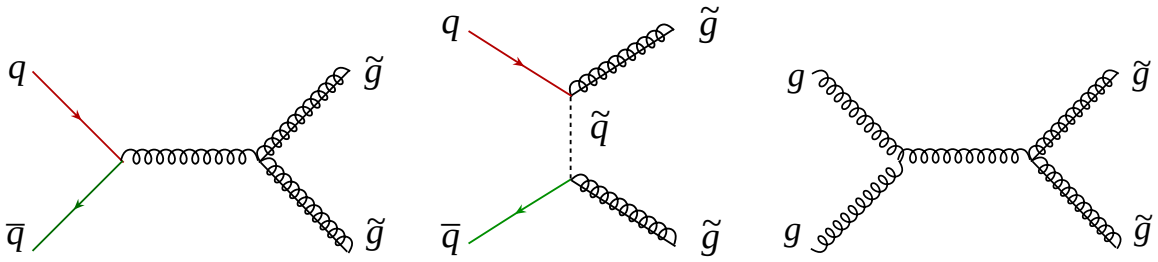

Figure D.1: Mecanismos de producción de gluinos a primer orden a la energía de centro de masas de Tevatron.

En la región de interés para este análisis ($m_t, m_{\tilde{\chi}^+} > m_{\tilde{b}} > m_{\tilde{\chi}^0}$), la desintegración dominante es sbottom a bottom quark y neutralino $\tilde{b} \to b\tilde{\chi}^0$, con ninguna otra desintegración posible, puesto que exigimos que $m_{\tilde{b}} < m_t, m_{\tilde{\chi}^+}$. Por lo tanto, asumimos un tasa de desintegración del

100% para el $\tilde{b} \rightarrow b\tilde{\chi}^0$. La cadena completa de desintegración del gluino se muestra en la figura D.2.

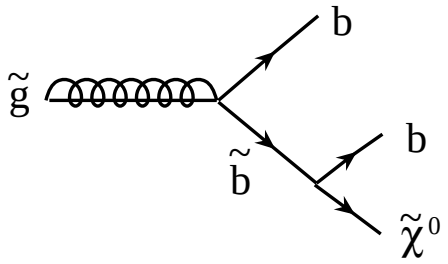

Figure D.2: Desintegración del gluino en quark bottom y sbottom.

En el caso del stop, dada la gran masa del quark top, la separación entre estados de masa aparece de forma natural:

$$m^2_{\tilde{t}_{1,2}} = \frac{1}{2}[m^2_{\tilde{t}_L} + m^2_{\tilde{t}_R} \pm \sqrt{(m^2_{\tilde{t}_L} - m^2_{\tilde{t}_R})^2 + 4m^2_t(A_t - \mu cot\beta)^2}] \tag{D.2}$$

Asumiendo conservación de paridad-R, los quarks stop se producen en pares, como se muestra en la figura D.3 y la partícula supersimétrica más ligera debe ser estable. Si además no tiene color y es neutra, escapará a la detección produciendo momento trasnverso neto en el estado final.

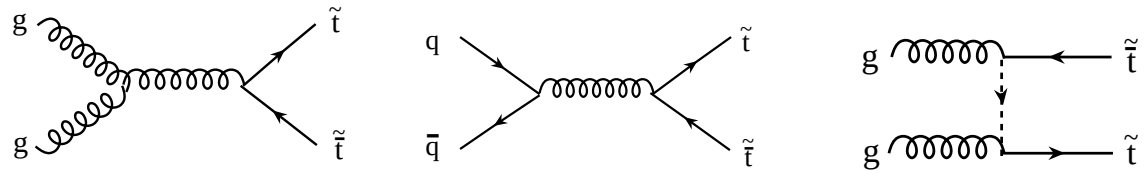

Figure D.3: Mecanismos de producción de stop a primer orden a la energía en el centro de masas del Tevatron.

Este escenario es accesible en el rango $m_{\tilde{t}_1} < m_b + m_{\tilde{\chi}^+}$ y $m_{\tilde{t}_1} < m_W + m_b + m_{\tilde{\chi}^0}$ en el cual, la desintegración dominante de $\tilde{t}_1$ es el proceso de cambio de sabor $\tilde{t}_1 \rightarrow c\tilde{\chi}^0$ que típicamente se asume como un 100%, tal y como se muestra en la figura D.4. La desintegración $\tilde{t}_1 \rightarrow t\tilde{\chi}^0$ está cinematicamente prohibida por encima del rango de masas del $\tilde{t}_1$ accesible a día de hoy en el Tevatron. Por otro lado, la desintegración a tres cuerpos $\tilde{t}_1 \rightarrow bff'\tilde{\chi}^0$ es despreciable. En

este caso particular, el estado final consiste en dos c-jets y momento transverso neto procedente del $\tilde{\chi}^0$.

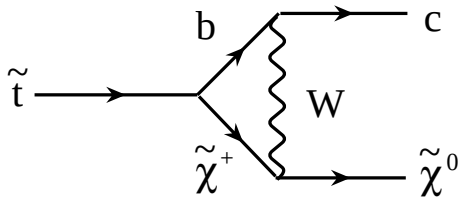

Figure D.4: Desintegración de stop en charm y neutralino.

Dispositivo experimental

El acelerador Tevatron situado en el Fermi National Accelerator Laboratory (Fermilab) en Batavia (Illinois, EEUU) es un colisionador protón-antiprotón con una energía en el centro de masas de 1.96 TeV. Estas instalaciones tienen cinco aceleradores y anillos de almacenamiento usados en etapas sucesivas para acelerar las partículas hasta 980 GeV.

El ciclo de aceleración empieza con la producción de protones a partir de hidrógeno ionizado, que se aceleran hasta 750 KeV por un Cockroft-Walton. Estos iones preacelerados se inyectan en el Linac donde se aceleran hasta 400 GeV. Al final de este proceso, los iones pasan a través de una hoja de carbono para arrancar sus electrones y producir protones. Dentro del Booster los protones se agrupan en paquetes y se aceleran hasta una energía de 8 GeV. En el Main Injector, estos protones se aceleran hasta 150 GeV y se inyectan en el paso final en el Tevatron.

La producción de antiprotones es significativamente más complicada. El ciclo empieza con la extracción de protones a 120 GeV del Main Injector y su posterior colisión contra un blanco de acero inoxidable. Este proceso produce una amplia variedad de partículas entre las que se encuentran los antiprotones. Las partículas emergen del blanco con diferentes ángulos y son focalizadas hacia la linea de aceleración. Con el objetivo de seleccionar solo antiprotones, el haz de partículas se envía a través de un imán pulsado que actúa como expectrómetro. Los antiprotones asi producidos son inyectados en el Debuncher, un acelerador que aumenta su energía hasta 8 GeV. Después de este proceso, el haz de antiprotones se dirige al Accumulator,

un anillo de almacenamiento. Desde ahí, los antiprotones son finalmente inyectados en el Main Injector y acelerados hasta 150 GeV, desde donde se inyectan al Tevatron de la misma manera que los protones.

El detector CDF II se encuentra en operación desde 2001. Es un detector multipropósito que combina varios subdetectores dispuestos de forma cilíndrica y concentrica respecto al eje de del haz de partículas. CDF II, mostrado en la figura D.5, está formado por:

- Un sistema de identificación de trazas que proporciona la medida del momento de las partículas cargadas, la posición del vértice primario de la interacción en el eje z, y permite, a su vez, reconstruir vértices secundarios.
- Un calorímetro cuyo propósito es medir la energía de las partículas cargadas producidas en la interacción.
- Cámaras de deriva y centelleadores para la detección de muones.

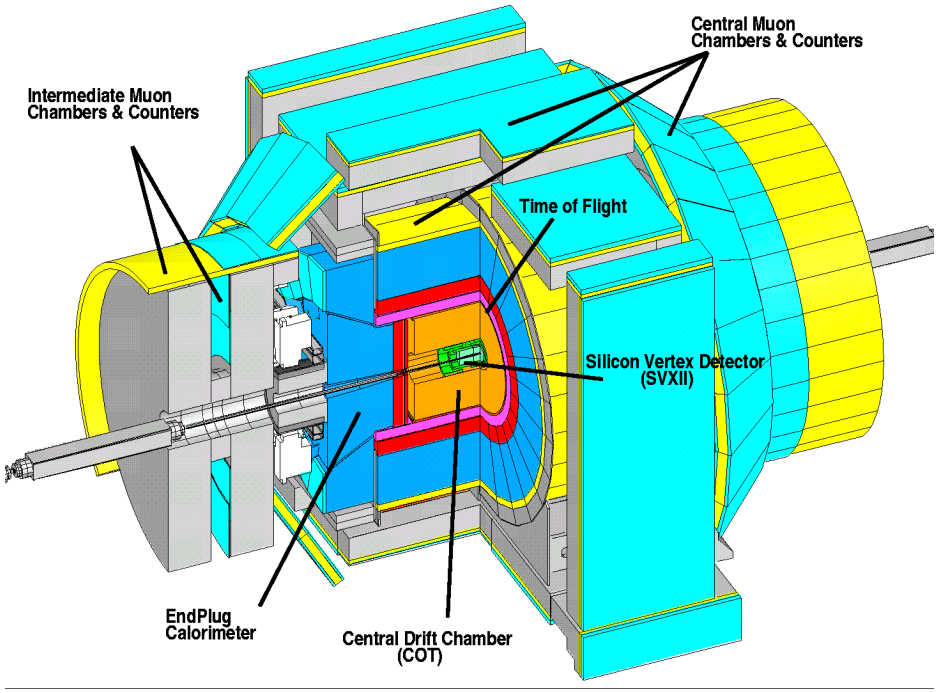

Figure D.5: Vista del detector CDF Run II.

En los siguientes párrafos se llevará a cabo una breve introducción a cada uno de los subdetectores empezando por los más cercanos a la tubería del haz y siguiendo hacia el exterior en dirección radial.

Los sistemas de identificación de trazas se encuentran dentro de un solenoide superconductor de 1.5 m de radio y 4.8 m de longitud que genera un campo magnético de 1.4 T paralelo al eje del haz de partículas. La parte más interna del sistema de identificación de trazas es un detector de microtiras de silicio resistente a la radiación. Se extiende desde un radio de 1.2 cm hasta 28 cm, cubriendo las regiones centrales del detector.

La capa más interna de silicio se conoce como L00 y está formada por microtiras activas solo por uno de sus lados. Las siguientes cinco capas de silicio después del L00, constituyen el SVXII. Finalmente, las dos capas más externas forman el ISL. Las siete capas que forman el SVXII y el ISL contienen material sensible por los dos lados y proporcionan información de la posición de las partículas con una precisión de 9 micras en el mejor de los casos.

Rodeando el detector de silicio se encuentra la Central Outer Tracker (COT), la pieza fundamental del sistema de detección de trazas de CDF II. La COT es una cámara de deriva cilíndrica de 3.1 m de longitud, que cubre en la zona radial una región desde los 40 a los 137 cm. Esta formada por 96 capas de hilos sensibles que están agrupados de forma radial en 8 supercapas. El número total de hilos sensibles de la COT es 30240. Aproximadamente la mitad de estos hilos van en la dirección z y la otra mitad están inclinados un pequeño ángulo (2 grados) con respecto a la dirección z. La combinación de estos dos tipos de hilos permite la medida de posiciones en z.

El sistema de calorímetros de CDF II se encuentra rodeando el sistema de detección de trazas en la parte exterior del solenoide. Los distintos calorímetros que componen el sistema son detectores basados en centelleadores segmentados en torres proyectivas que apuntan a la región de interacción.

El calorímetro está dividido en dos regiones: la región central y el “plug”. Cada una de estas regiones esta dividida en parte electromagnética y hadrónica. La parte electromagnética proporciona información para reconstruir objetos como electrones o fotones, mientras que la parte hadrónica se usa para la reconstrucción de jets.

Por último, en la parte más externa de CDF II se encuentran las cámaras de muones. El sistema de detección de muones consiste en un conjunto de cámaras de deriva y centelleadores que están instalados en la parte exterior del calorímetro.

Como complemento a los sistemas de detección, CDF II cuenta con un complejo sistema de adquisición de datos. La tasa media de interacciones en el Tevatron es de 2,53 Mhz. Esta tasa de interacción es órdenes de magnitud superior a la máxima tasa que el sistema de adquisición de datos puede soportar. Además, la mayoría de las colisiones producidas son de un interés nulo

para el análisis de datos. Por estos motivos, CDF cuenta con un sistema automático de selección de sucesos a tiempo real, trigger. El trigger decide si el correspondiente suceso medido por el detector va a ser almacenado en cinta para su posterior análisis o descartado definitivamente.

El sistema de trigger de CDF consiste en tres niveles de decisión. Los dos primeros niveles están basados en hardware y el tercero consiste en una granja de procesadores. Las decisiones tomadas por el sistema están basadas en información de los sucesos con complejidad creciente. El nivel 1 del trigger es un sistema síncrono que lee sucesos y toma decisiones cada vez que se produce un cruce de protones y antiprotones. El nivel 1 del trigger reduce la tasa de sucesos de 2,53 MHz a menos de 50 kHz. El hardware de este nivel 1 consiste en tres lineas paralelas de procesado que alimentan a la unidad global de decisión de nivel 1. Una de las lineas se encarga de encontrar objetos basados en medidas del calorímetro, L1 CAL, otra encuentra muones, L1 MUON, mientras que la tercera encuentra trazas en la COT, L1 TRACK. Puesto que los muones y electrones necesitan la presencia de una traza apuntando al correspondiente detector, la información de estas trazas se envía a las lineas de calorímetro, muones y trazas.

Finalmente, la unidad global de decisión de nivel 1 toma una decisión basada en los objetos de interés encontrados por diferentes procesos del nivel 1.

Como segundo paso en sistema de decisión tenemos el nivel 2 del trigger que es un sistema asíncrono que procesa sucesos recibidos desde el nivel 1. Después del nivel 2, la tasa de sucesos se reduce a 1 kHz.

Una vez que el suceso es aceptado a nivel 2, tiene que ser procesado completamente con toda la información disponible en el detector. Esta operación tiene lugar en el granjas de procesadores a nivel 3. El nivel 3 reconstruye el suceso utilizando algoritmos que usan toda la información disponible en el detector y mejoran la resolución utilizada en los niveles anteriores. Esto incluye una reconstrucción tridimensional de las trazas, el emparejamiento entre trazas y calorímetro o sistema de muones. Los sucesos que pasan satisfactoriamente los requisitos del nivel 3 son transferidos al sistema de almacenado en cinta magnética. La tasa media de procesado a nivel 3 por suceso es de unos pocos segundos. La tasa de sucesos cumpliendo los requisitos de nivel 3 se reduce a 50 Hz.

Reconstrucción de sucesos

Para realizar un analis de datos, la información obtenida del detector tiene que ser procesada con el objetivo de reconstruir observables. Esta reconstrucción implica algoritmos matemáticos y definiciones muy relacionadas con el detector en si mismo.

Los análisis descritos en esta tesis están basados en jets, momento transverso neto y de forma indirecta, electrones y muones.

De especial relevancia es la reconstrucción del vértice primario de interacción. El vértice no es un objeto de análisis como tal, sin embargo, es la referencia inicial para la reconstrucción de cualquier otro objeto final.

En los análisis presentados en este trabajo no se esperan leptones en el estado final. Por lo tanto, durante los procesos de optimización de señal se aplica un rechazo de este tipo de objetos. Esta condición de rechazo implica la identificación de dicho objeto.

Para la identificación de electrones se requiere, básicamente, una deposición de energía aislada en el calorímetro central de más de 10 GeV/c. Por su parte, los muones candidatos han de tener una traza en las cámaras de deriva con momento transverso de más de 10 GeV/c y sin ninguna condición en las cámaras de muones.

De especial interés para nuestros estudios son los sucesos que después de la interacción de quarks y gluones producen chorros de partículas conocidos como jets. Estos jets son reconocibles por sus deposiciones de energía en el calorímetro.

Existen varios algoritmos para la reconstrucción de jets. La mayoría de ellos están basados en información puramente calorimétrica, sin embargo, también se pueden encontrar algoritmos que incorporan información de trazas. La identificación de jets usada en estas búsquedas se basa por completo en el algoritmo JETCLU.

Este algoritmo comienza buscando una torre en el calorímetro con energía superior a 1 GeV, luego por agrupación de torres adyacentes dentro de un radio dado desde la torre de mayor energía a la de menor energía se construye un pre-jet. Una torre puede estar asignada a uno y solo un pre-jet. En el siguiente paso, se calcula el centro de cada pre-jet y se define un nuevo cono incluyendo torres con energía superior a 100 MeV. Si el centro del nuevo pre-jet cambia, el cono es redefinido y se añaden nuevas torres de forma iterativa. Cuando se encuentra una solución estable, se evita el solapamiento entre objetos uniéndolos o separándolos pre-jets contiguos y de esta forma se define el objeto final, jet.

Por último, la energía del jet se corrige por la dependencia del calorímetro con la pseudo-

rapidez y la energía procedente de interacciones múltiples.

El último de los objetos definidos es el momento transverso neto. La presencia de partículas indetectables en un suceso es inferida por la medida de momento transverso no nulo en el detector. Esta cantidad se reconstruye basandose por completo en información del calorímetro.

Algoritmos de tagging

El hecho de que la mayoría de los sucesos de procesos considerados fondos contengan solo quarks ligeros en sus estados finales, hace al tagging de sabores pesados una de las herramientas más poderosas a la hora de eliminar fondos. Diferentes algoritmos y separadores de sabor se usan de forma extensiva en la física de partículas.

Los hadrones B en jets provinientes de la fragmentación de quarks b, tienen de media una distancia de vuelo de unas 500 micras, produciendo vértices secundarios con respecto al punto de interacción. Estos hadrones viajan alejandose del vértice primario y desintegrandose a través de una cascada de partículas. Los productos cargados de esta desintegración se pueden reconstruir generalmente como trazas desplazadas. La intersección de estas trazas forma vértices secundarios en el punto donde los hadrones se habian desintegrado.

El algoritmo SecVtx busca trazas desplazadas combinando trazas dentro de un jet "taggable". Los jets son taggable si la E_T^{raw} >10 GeV, η <2.4, y tienen al menos dos *good tracks*. El algoritmo primero intenta combinar tres o más trazas con requisitos de selección suaves. Si esto falla, se intenta repetir el procedimiento con pares de trazas con requisitos más duros. El desplazamiendo del vértice secundario con respecto al vértice primario en el plano transverso viene dado por:

$$L_{xy} = \vec{d} \cdot \hat{p}_T \tag{D.3}$$

donde $\vec{d}$ es el desplazamiento del vértice secundario y $\hat{p}_T$ es vector unitario en la dirección del momento del jet.

Como complemento a los algoritmos de tagging se pueden construir separadores de sabor utilizando tecnicas más sofisticadas. En el desarrollo del trabajo presentado en esta tesis ha sido necesario desarrollar una de estas herramientas construida explicitamente para optimizar uno de los análisis. El CHAOS, **C**harm **H**adron **A**nalysis **O**riented **S**eparator, se usa para determinar cuando un tagged jet ha sido producido por la hadronización de un quark ligero, falsamente

identificado como un quark pesado, un quark b, o un quark c. Dependiendo del sabor del partón original, el tagged jet y su vértice secundario tienen diferentes características, principalmente relacionadas con las trazas.

Usando propiedades de las trazas que forman el vértice secundario y las trazas del jet en una red neuronal, CHAOS nos permite aumentar la presencia de c-jets en nuestro estado final.

CHAOS es una red neuronal basada en SNNS. La estructura incluye tres capas, una capa de entrada con 22 nodos, una capa oculta con 22 nodos y una capa de salida con 2 nodos produciendo una salida bidimensional. La red neuronal utiliza un conjunto de 22 variables, relacionadas en su mayoría con propiedades de las trazas. Estas variables se pueden encontrar en la Tabla D.3 y han sido seleccionadas de forma cuidadosa para estar bien reproducidas por la simulación y para tener un comportamiento estable, evitando dependencias con la cinematica de los jets.

Variables de entrada del CHAOS	
Mass of the vertex	Average $\|d_0\|$ of good tracks
Charge of the vertex	Average $\|d_0$ significance$\|$ of good tracks
L_{xy} significance	Fraction of good tracks with $\|d_0$ significance$\|$ >1
$\frac{Number\ of\ pass{-}1\ tracks}{Number\ of\ good\ tracks}$	Fraction of good tracks with $\|d_0$ significance$\|$ >3
$\frac{Number\ of\ vertex's\ tracks}{Number\ of\ good\ tracks}$	Fraction of good tracks with $\|d_0$ significance$\|$ >5
$\frac{\sum p_T(good\ tracks)}{E_T}$, where E_T is the jet E_T	$\frac{P_T}{E_T}$, where P_T is the P_T of the secondary vertex
$z_t = \frac{\sum p_T(pass{-}1\ tracks)}{\sum p_T(good\ tracks)}$	Fraction of vertex p_T in the leading track
$r_{vtx} = \frac{p_T\ of\ the\ vertex}{\sum p_T(good\ tracks)}$	Fraction of vertex p_T in the second leading track
Signed d_0 of the leading vertex track	Signed d_0 significance of the leading vertex track
Signed d_0 of the second leading vertex track	Signed d_0 significance of the second leading vertex track
ϕ_{jet}	η_{jet}

Table D.3: Listas de variables usadas en el CHAOS.

La salida bidimensional de la red neuronal permite la separacion de tres sabores diferentes. Cortando en esta salida se puede seleccionar el sabor deseado. En nuestro caso particular utilizamos el CHAOS para seleccionar jets c, como se muestra en la figura D.6.

Las eficiencias de selección para jets b y c se resumen en la Tabla D.4. Los números presentados son obtenidos para un corte en el CHAOS de 1.65.

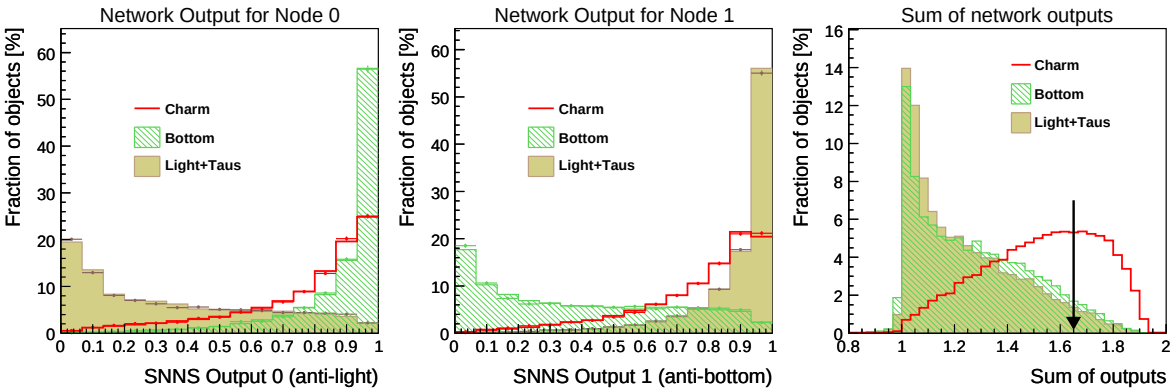

Figure D.6: Figuras de salida del CHAOS en 1-D.

	c jets	b jets
Eficiencia (Datos)	0.346 ± 0.052	0.073 ± 0.014
Factor de escala$_{CHAOS}$	1.01 ± 0.15	1.14 ± 0.22

Table D.4: Eficiencia de selección de c y b tagged jets y factores de escala (SF$_{CHAOS}$) para un corte en el CHAOS de 1.65.

Búsqueda de sbottom producido a través de gluinos

El primero de los análisis de datos presentado en este trabajo es la búsqueda de sbottom quarks a través de la desintegración de gluinos. Asumiendo paridad R, los gluinos se producen en pares, desintegrándose cada uno de ellos en bottom quark y sbottom quark. A su vez, cada sbottom se desintegra en bottom quark y neutralino. Como resultando un estado final con cuatro b-jets y momento transverso neto procedente de los neutralinos, que escapan a la detección. Se asume en que la cadena de desintegración descrita ocurre en un 100 % de las veces.

Con un estado final semejante, el uso de herramientas como el “tagging” es obligatorio para una optimización adecuada. El primer paso en cualquier análisis es la correcta estimación de los fondos. Varios procesos del Modelo Estándar, producidos en el Tevatron, tienen un estado final que similar a nuestra señal de sbottom. Los sucesos seleccionados en el análisis tienen como principales características: un momento transverso neto elevado, gran multiplicidad de jets, jets procedentes de quarks pesados y la ausencia de leptones.

Los fondos del Modelo Estándar que tienen estas características son:

- Producción e quark top
- Producción de dibosones
- Producción de W/Z + jets
- Producción de multijes
- Producción de multijes ligeros

El mayor desafío del análisis es, sin duda, la estimación de uno de los fondos mayoritarios, la producción de multijets, a partir de los datos. Puesto que la simulación de este fondo mediante métodos de Monte Carlo supondría un gasto ingente de recursos informáticos, se ha estimado la contribución como un cociente de "tagged jets" sobre proto-"tagged jets", en una muestra representativa y parametrizado con respecto a varias variables. El método que se ha desarrollado recibe el nombre de MUTARE. La forma precisa de obtener la estimacion del MUTARE es la siguiente:

$$R_{MUTARE} = \frac{N_{tags} - N_{mistags} - N_{tags}^{MC}}{N_{taggable} - N_{taggable}^{MC}} \tag{D.4}$$

donde N_{tags} es el número de tagged jets, $N_{mistags}$ es el numero de jets procedentes de quarks ligeros identificados de forma erronea como jets procedentes de quarks pesados, N_{tags}^{MC} es el número de tagged jets procedentes de procesos no-multijet estimados a partir de Monte Carlo, $N_{taggable}$ es el número de taggable jets, y $N_{taggable}^{MC}$ es el número de taggable jets procedentes de procesos no-multijet estimados a partir de Monte Carlo.

La predicción final se obtiene después de sustraer la contribución de sabores pesados procedentes de procesos no-multijet.

$$N_{events}^{HF\ multijet} = R(N_{taggable}^{data} - N_{taggable}^{MC}) \tag{D.5}$$

Una vez demostrado que los fondos son reproducibles en regiones de control definidas "a priori", se lleva a cabo una optimización de la señal de sbottom usando dos redes neuronales en dos regiones cinemáticas distintas. La primera de las redes neuronales se utiliza para la eliminación de multijets, el fondo dominante antes de cualquier optimización y la segunda red neuronal se utiliza para elliminar la producción de $t\bar{t}$, el fondo dominante en el estado final.

El proceso descrito se lleva a cabo para dos señales de sbotton distintas para tener en cuenta dos regiones cinemáticas bien diferenciadas. Estas dos regiones se caracterizan por la diferencia

de masas entre el gluino y el sbottom. Los valores particulares elegidos para las optimizaciones son los siguientes:

- Optimización con gran $\Delta m \Rightarrow$ M($\tilde{g}$) = 335 GeV/c^2, M($\tilde{b}$) = 260 GeV/c^2
- Optimización con pequeño $\Delta m \Rightarrow$ M($\tilde{g}$) = 335 GeV/c^2, M($\tilde{b}$) = 315 GeV/c^2

Como resultado de esta búsqueda no se ha encontrado ninguna desviación de la predicción del Modelo Estándar en el espacio de fases estudiado y se ha procedido a extraer un límite en la sección eficaz de producción del sbottom con un 95% de nivel de confianza, como se muestra en la figura D.7.

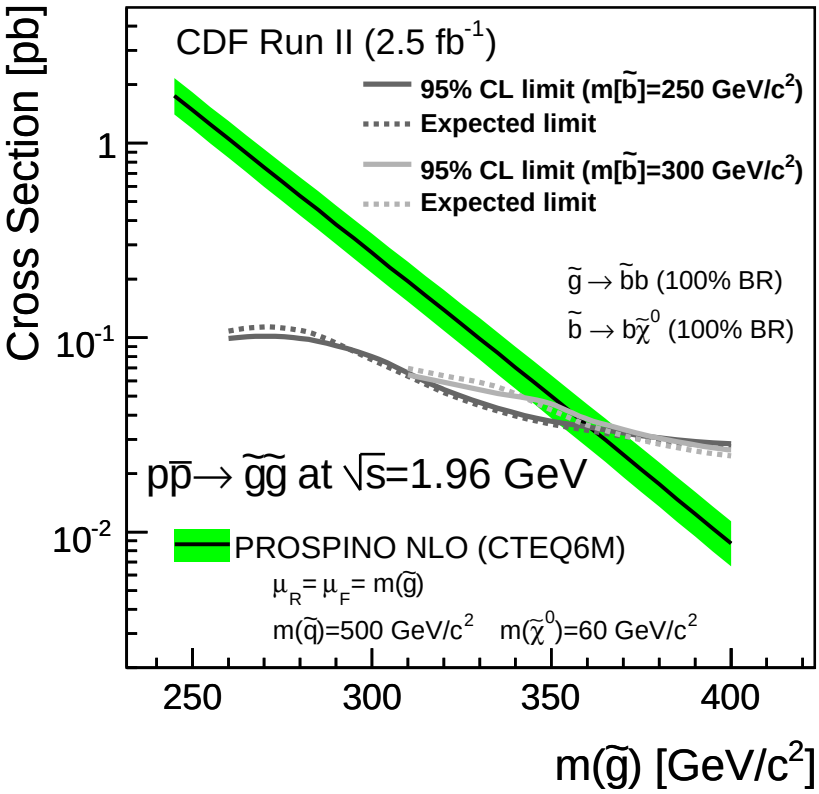

Figure D.7: Límites con un 95% de nivel de confianza en la sección eficaz de producción, observado (linea solida) y esperado (linea de puntos).

Búsqueda de stop desintegrandose en charm y neutralino

El segundo análisis llevado a cabo como parte de la presente tesis, es la búsqueda de quark stop desintegrandose en quark charm y neutralino. Puesto que el stop se produce en pares asumiendo paridad R, el estado final está compuesto por dos charm jets y momento transverso neto procedente de los neutralinos. Este análisis es en muchos aspectos similar al descrito anteriormente por lo que la estimación de los fondos se lleva a cabo practicamente de la misma forma.

En este caso, los sucesos seleccionados en el análisis tienen como principales características: un momento transverso neto moderado, jets procedentes de c quarks y la ausencia de leptones.

Los fondos del Modelo Estándar que tienen estas características son los mismos que se han descrito en análisis anterior pero con una proporción diferente:

- Producción e quark top
- Producción de dibosones
- Producción de W/Z + jets
- Producción de multijes
- Producción de multijes ligeros

Sin embargo, el mayor reto en este caso es enriquecer la muestra en su estado final con charm jets, algo no trivial con los algoritmos de "tagging" estándar usados en CDF II. Por este motivo se ha tenido que desarrollar un separador de sabor para jets, basado en una red neuronal con nodo de salida en dos dimensiones que permite distinguir el sabor de los jets separándolos en charm, bottom y jets ligeros (u,d,s). El anteriormente mencionado CHAOS.

El proceso de optimización se ha llevado a cabo utilizando una señal de stop con las siguientes características:

- m($\tilde{t}$) = 125 GeV/c^2, m($\tilde{\chi}_0$) = 70 GeV/c^2

El primer paso en la optimización es la eliminación de gran parte del fondo de multijets mediante una red neuronal entrenada para distinguir la señal de stop y la producción de multijets. Una vez seleccionados los sucesos aplicando un corte en el discriminante de la red neuronal, se

aplica el CHAOS para aumentar la contribucion de jets c en el estado final. Aplicando nuevamente un corte, esta vez en el CHAOS a 1.65, se obtiene la región final.

No se ha encontrado ninguna desviación de la predicción del Modelo Estándar en el espacio de fases estudiado y se ha procedido a extraer un límite en la sección eficaz de producción del sbottom con un 95 % de nivel de confianza.

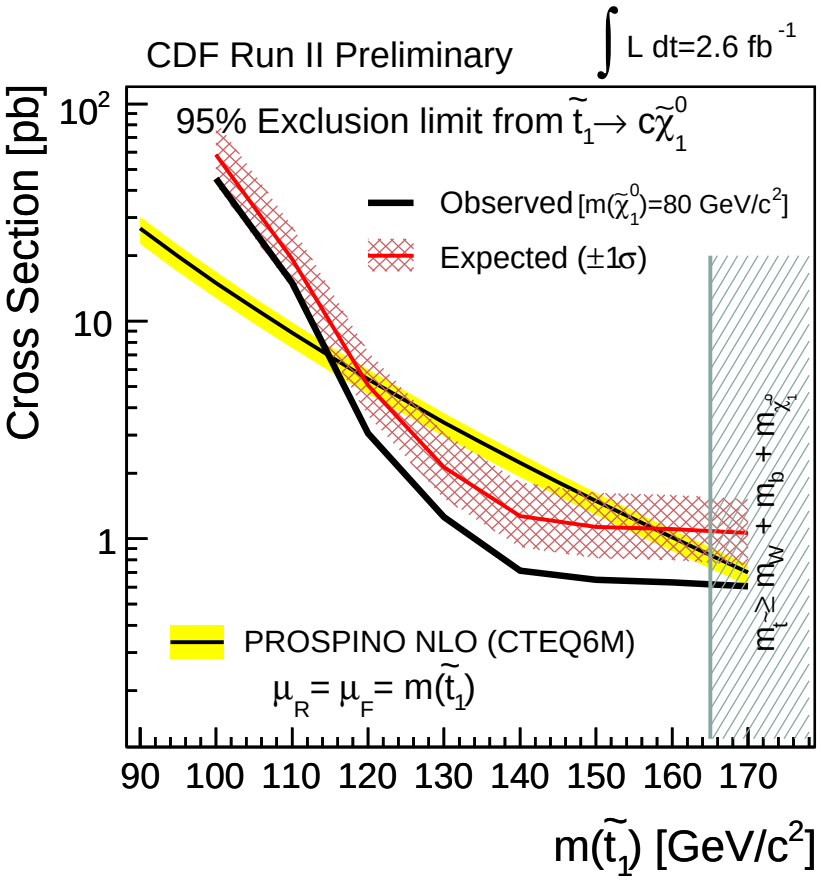

Figure D.8: Límite observado con un 95% de nivel de confianza en terminos de sección eficaz para una m($\tilde{\chi}^0$) = 80 Gev/c^2 (linea negra) y límite esperado (linea roja) con una banda de incertidumbre de 1σ.

Errores sistemáticos

En los dos análisis descritos se han llevado a cabo detallados estudios de los errores sistemáticos. En esta sección describiremos los errores procedentes de la búsqueda de stop desintegrandose en charm y neutralino, ya que incluyen errores en la forma además de los errores que afectan a la normalización.

Los errores sistemáticos son la mayor fuente de incertidumbre en cualquiera de las dos búsquedas presentandas en esta tesis. Algunos de ellos afectan a la normalización de la señal o los fondos. Esta clase de errores tiene un impacto directo en el número de suscesos. Sin embargo, la forma de las predicciones no está afectada por este tipo de errores.

Por el contrario, algunos errores sistematicos producen una variación en la forma de las predicciones. Esta segunda clase de errores sistemáticos se conoce como errores de forma y puede afectar a su vez al numero de sucesos predichos.

Dado que la forma de los fondos es utilizada para la extracción de los límites de exclusión, este tipo de errores de forma son especialmente importantes.

Los errores sistemáticos en señal y fondos han sido estudiados teniendo en cuenta correlaciones y anticorrelaciones entre ellos.

- Escala de Energía de los Jets: Un error sistemático en la escala de energía del calorímetro afecta a la energía transversa total de los jets. El efecto en la región final es despreciable.
- Factor de Escala del Tagging: Las diferencias entre datos y Monte Carlo en eficiencia de tagging son tenidas en cuenta como un error sistemático. El error resultante en la región final es de un 3.6%.
- Factor de Escala del CHAOS: La diferancia entre datos y Monte Carlo es tomada como un error sistemático. El error resultante en la región final es del 9.2%.
- Estimación de Mistags: El error asignado es del 4.8%.
- Luminosidad: El error sistemático debido a la luminosidad es del 6%.
- ISR/FSR: La incertidumbre asociada a los estados inicial y final de radiación ha sido evaluado generando muestras con mayor y menor ISR/FSR. El efecto en la región final es del 1.7%.
- PDF: El error en las PDF ha sido determinado como un 3.8% en la aceptancia.

- Fondo de Multijet (MUATRE): Asignamos una incertidumbre del 30%.
- Sección eficaz de producción de $t\bar{t}$: Se cita una incertidumbre del 11%.
- Sección eficaz de producción de top: La incertidumbre en este proceso es del 13%.
- Sección eficaz de producción de dibosones: Citamos una incertidumbre del 10% en WW y WZ y un 20% para los procesos ZZ.
- Sección eficaz de producción de procesos electrodébiles: Asignamos un 40% de incertidumbre en la predicción de estos procesos.
- Masa del quark top: En el presente análisis, la producción de $t\bar{t}$ se estima usando métodos de Monte Carlo con una masa del quark top de 175 GeV/c^2. Puesto que nuestra optimización de señal está basada en una red neuronal entrenada con procesos de $t\bar{t}$, incluimos un error sistemático debido a las dependencia de la red neuronal con la masa utilizada. Calculamos este error midiendo el número de sucesos de top en selección final usando una masa para el quark top de 172.5 GeV/c^2.
- Diferencias de forma entre ALPGEN y PYTHIA: Incluimos un sistemático en la forma en las selecciones finales debido a las diferencias entre los generadores ALPGEN y PYTHIA usados para estimar los procesos de Z/W + jets.
- Estimación de multijets y mistags después del CHAOS: Citamos una incertidumbre en la región final del 3.6% y 8.2% respectivamente.

Conclusiones

Dos búsquedas de squarks de la tercera familia en la muestra de jets y momento transverso neto han sido llevadas a cabo. Puesto que no se han encontrado desviaciones significativas con respecto a las predicciones del Modelo Estándar, los resultados han sido utilizados para extraer límites con un 95% de nivel de confianza en la sección eficaz de producción de estos dos procesos de SUSY.

La sensibilidad alcanzada por estos análisis está basada en la robustez de la descripción de los fondos y en el poder de la técnicas de optimización de la señal. En estos dos últimos aspectos, merece un crédito especial el método MUTARE, para la estimación del fondo de multijets a partir de datos y el CHAOS. Estas dos herramientas, desarrolladas para la realización

de estos dos análisis tienen además un amplio espectro de aplicación a lo largo del programa de física.

El único experimento, a día de hoy, capaz de realizar unas búsquedas semejantes es D0. La búsqueda de stop ha sido llevada a cabo por D0, alcanzando una sensibilidad que proporciona una región de exclusión menor, en parte debido a la menor cantidad de datos usados.

El programa de búsqueda de SUSY en Tevatron será crucial en los próximos años, incluso después del inicio del LHC en los próximos meses. En particular, escenarios en los que los squarks de la tercera familia se asumen como ligeros, como los mostrados en la presente tesis, segiran siendo importantes a la escala de energías de Tevatron. Sin embargo, la conquista de la escala del TeV en el LHC, será sin duda el mayor de los retos en los años venideros. El trabajo realizado en esta tesis se ha hecho con dos claras intenciones: explorar las frontera energética de Tevatron buscando nueva físisca y desarrollar técnicas de análisis en preparación para los nuevos datos del LHC.

Ambas intenciones se han hecho realidad en la presente tesis, en primer lugar fijando los mejores limites de exclusión del mundo para los análisis llevados a cabo y por últimos desarrollando e implementando de forma satisfactoria nuevas técnicas de análisis.

Bibliography

[1] D. N. Spergel et al. Wilkinson microwave anisotropy probe (wmap) three year results: Implications for cosmology. *Astrophys.J.Suppl.*, 170:377, 2007.

[2] Mary K. Gaillard, Paul D. Grannis, and Frank J. Sciulli. The standard model of particle physics. *Rev. Mod. Phys.*, 71:S96–S111, 1999.

[3] A.D. Martin F. Halzen. *Quarks and Leptons: An Introductory Course in Modern Particle Physics*. Wiley Text Books, 1984.

[4] David Griffiths. *Introduction to Elementary Particles*. Wiley, 1987.

[5] W. M. Yao et al. Review of particle physics. *J. Phys.*, G33:1–1232, 2006.

[6] CDF and DØ Collaborations. Combination of cdf and DØ results on the mass of the top quark. hep-ex/0903.2503, 2009.

[7] R. P. Feynman. Mathematical formulation of the quantum theory of electromagnetic interaction. *Phys. Rev.*, 80:440–457, 1950.

[8] R. Keith Ellis, W. James Stirling, and B. R. Webber. Qcd and collider physics. *Camb. Monogr. Part. Phys. Nucl. Phys. Cosmol.*, 8:1–435, 1996.

[9] G. Dissertori, I. G. Knowles, and M. Schmelling. *High energy experiments and theory*. Oxford, UK: Clarendon (2003) 538 p.

[10] A. D. Martin, W. J. Stirling, R. S. Thorne, and G. Watt. Update of parton distributions at nnlo. *Phys. Lett.*, B652:292–299, 2007. MRST Webpage, http://durpdg.dur.ac.uk/hepdata/mrs.html.

[11] H. L. Lai et al. Improved parton distributions from global analysis of recent deep inelastic scattering and inclusive jet data. *Phys. Rev.*, D55:1280–1296, 1997. CTEQ Webpage, http://www.phys.psu.edu/∼cteq/.

[12] D. Stump et al. Uncertainties of predictions from parton distribution functions. i: The lagrange multiplier method. *Phys. Rev.*, D65:014012, 2002.

[13] J. Pumplin et al. Uncertainties of predictions from parton distribution functions. ii: The hessian method. *Phys. Rev.*, D65:014013, 2002.

[14] E. Fermi. An attempt of a theory of beta radiation. 1. *Z. Phys.*, 88:161–177, 1934.

[15] S. L. Glashow. Partial symmetries of weak interactions. *Nucl. Phys.*, 22:579–588, 1961.

[16] Abdus Salam and John Clive Ward. Electromagnetic and weak interactions. *Phys. Lett.*, 13:168–171, 1964.

[17] Steven Weinberg. A model of leptons. *Phys. Rev. Lett.*, 19:1264–1266, 1967.

[18] L. D. Faddeev and V. N. Popov. Feynman diagrams for the yang-mills field. *Phys. Lett.*, B25:29–30, 1967.

[19] G. Arnison et al. Experimental observation of lepton pairs of invariant mass around 95 GeV/c^2 at the CERN SPS collider. *Phys. Lett.*, B126:398–410, 1983.

[20] G. Arnison et al. Experimental observation of isolated large transverse energy electrons with associated missing energy at $\sqrt{s}$ = 540 GeV. *Phys. Lett.*, B122:103–116, 1983.

[21] H. Georgi, Helen R. Quinn, and Steven Weinberg. Hierarchy of interactions in unified gauge theories. *Phys. Rev. Lett.*, 33:451–454, 1974.

[22] Leonard Susskind. Dynamics of spontaneous symmetry breaking in the weinberg- salam theory. *Phys. Rev.*, D20:2619–2625, 1979.

[23] Stephen P. Martin. A supersymmetry primer. 1997.

[24] Hitoshi Murayama. Supersymmetry phenomenology. 2000.

[25] Rudolf Haag, Jan T. Lopuszanski, and Martin Sohnius. All possible generators of supersymmetries of the s matrix. *Nucl. Phys.*, B88:257, 1975.

[26] Robert Nyden Hill and Edward H. Kerner. Unique canonical representation of the inhomogeneous lorentz group in relativistic particle dynamics. *Phys. Rev. Lett.*, 17:1156, 1966.

[27] Joseph Polchinski and Leonard Susskind. Breaking of supersymmetry at intermediate-energy. *Phys. Rev.*, D26:3661, 1982.

[28] Edward Witten. Dynamical breaking of supersymmetry. *Nucl. Phys.*, B188:513, 1981.

[29] Romesh K. Kaul. Gauge hierarchy in a supersymmetric model. *Phys. Lett.*, B109:19, 1982.

[30] Ugo Amaldi, Wim de Boer, and Hermann Furstenau. Comparison of grand unified theories with electroweak and strong coupling constants measured at lep. *Phys. Lett.*, B260:447–455, 1991.

[31] Ugo Amaldi, Wim de Boer, Paul H. Frampton, Hermann Furstenau, and James T. Liu. Consistency checks of grand unified theories. *Phys. Lett.*, B281:374–383, 1992.

[32] Paul Langacker and Ming-xing Luo. Implications of precision electroweak experiments for m_t, ρ_0, $sin^2\theta_W$ and grand unification. *Phys. Rev.*, D44:817–822, 1991.

[33] John R. Ellis, S. Kelley, and Dimitri V. Nanopoulos. Probing the desert using gauge coupling unification. *Phys. Lett.*, B260:131–137, 1991.

[34] F. Gliozzi, Joel Scherk, and David I. Olive. Supersymmetry, supergravity theories and the dual spinor model. *Nucl. Phys.*, B122:253–290, 1977.

[35] S. Heinemeyer, W. Hollik, D. Stockinger, A. M. Weber, and G. Weiglein. Precise prediction for m(w) in the mssm. *JHEP*, 08:052, 2006.

[36] H. E. Haber, (ed.) Harvey, Jeffrey A., and (ed.) Polchinski, J. Recent directions in particle theory: From superstrings and black holes to the standard model. proceedings, theoretical advanced study institute in elementary particle physics, boulder, usa, june 1-26, 1992. pages 589–686. Singapore, Singapore: World Scientific (1993) 827 p.

[37] David J. Gross and R. Jackiw. Effect of anomalies on quasirenormalizable theories. *Phys. Rev.*, D6:477–493, 1972.

[38] C. Bouchiat, J. Iliopoulos, and P. Meyer. An anomaly free version of weinberg's model. *Phys. Lett.*, B38:519–523, 1972.

[39] Luis Alvarez-Gaume and Edward Witten. Gravitational anomalies. *Nucl. Phys.*, B234:269, 1984.

[40] John F. Gunion, Howard E. Haber, Gordon L. Kane, and Sally Dawson. The higgs hunter's guide. SCIPP-89/13.

[41] S. Dawson. The mssm and why it works. 1997.

[42] Savas Dimopoulos and Howard Georgi. Softly broken supersymmetry and su(5). *Nucl. Phys.*, B193:150, 1981.

[43] N. Sakai. Naturalness in supersymmetric guts. *Zeit. Phys.*, C11:153, 1981.

[44] P. Fayet. Spontaneously broken supersymmetric theories of weak, electromagnetic and strong interactions. *Phys. Lett.*, B69:489, 1977.

[45] Pierre Fayet. Relations between the masses of the superpartners of leptons and quarks, the goldstino couplings and the neutral currents. *Phys. Lett.*, B84:416, 1979.

[46] Steven Weinberg. Supersymmetry at ordinary energies. 1. masses and conservation laws. *Phys. Rev.*, D26:287, 1982.

[47] N. Sakai and Tsutomu Yanagida. Proton decay in a class of supersymmetric grand unified models. *Nucl. Phys.*, B197:533, 1982.

[48] Savas Dimopoulos, Stuart Raby, and Frank Wilczek. Proton decay in supersymmetric models. *Phys. Lett.*, B112:133, 1982.

[49] John R. Ellis, Dimitri V. Nanopoulos, and Serge Rudaz. Guts 3: Susy guts 2. *Nucl. Phys.*, B202:43, 1982.

[50] Glennys R. Farrar and Pierre Fayet. Phenomenology of the production, decay, and detection of new hadronic states associated with supersymmetry. *Phys. Lett.*, B76:575–579, 1978.

[51] F. Zwirner. Observable delta b=2 transitions without nucleon decay in a minimal supersymmetric extension of the standard model. *Phys. Lett.*, B132:103–106, 1983.

[52] Lawrence J. Hall and Mahiko Suzuki. Explicit r-parity breaking in supersymmetric models. *Nucl. Phys.*, B231:419, 1984.

[53] John R. Ellis, G. Gelmini, C. Jarlskog, Graham G. Ross, and J. W. F. Valle. Phenomenology of supersymmetry with broken r-parity. *Phys. Lett.*, B150:142, 1985.

[54] Graham G. Ross and J. W. F. Valle. Supersymmetric models without r-parity. *Phys. Lett.*, B151:375, 1985.

[55] Sally Dawson. R-parity breaking in supersymmetric theories. *Nucl. Phys.*, B261:297, 1985.

[56] Savas Dimopoulos and Lawrence J. Hall. Lepton and baryon number violating collider signatures from supersymmetry. *Phys. Lett.*, B207:210, 1988.

[57] Carl E. Carlson, Probir Roy, and Marc Sher. New bounds on r-parity violating couplings. *Phys. Lett.*, B357:99–104, 1995.

[58] Gautam Bhattacharyya. R-parity-violating supersymmetric yukawa couplings: A mini-review. *Nucl. Phys. Proc. Suppl.*, 52A:83–88, 1997.

[59] D. J. H. Chung, L. L. Everett, G.L. Kane, S. F. King, J. Lykken, and L. Wang. The soft supersymmetry breaking lagrangian: Theory and applications. *Phys. Rept.*, 407, 2005.

[60] A. Bartl, W. Majerotto, and W. Porod. Squark and gluino decays for large tan beta. *Z.Phys.C*, C64:499–508, 1994. Erratum-ibid.C68:518,1995.

[61] W. Beenakker et al. Squark and gluino production at hadron colliders. *Nucl. Phys.*, B492:51–103, 1997.

[62] Torbjorn Sjostrand, Leif Lonnblad, and Stephen Mrenna. PYTHIA 6.2: Physics and manual. 2001.

[63] A. Abulencia et al. A search for scalar bottom quarks from gluino decays in p anti-p collisions at $\sqrt{s} = 1.96$ tev. *Phys. Rev. Lett.*, 96:171802, 2006.

[64] J. Pumplin et al. New generation of parton distributions with uncertainties from global QCD analysis. *J. High Energy Phys.*, 0207:012, 2002.

[65] D. Stump et al. Inclusive Jet Production, Parton Distributions, and the Search for New Physics. 2003.

[66] Fermilab Beam Division. http://www-bd.fnal.gov.

[67] Fermilab Beam Division. Run II Handbook. http://www-bd.fnal.gov/runII/index.html.

[68] R. Blair et al. The CDF II detector: Technical design report. Technical report, FNAL, 1996. FERMILAB-PUB-96/390-E.

[69] A. Sill. CDF Run II silicon tracking projects. *Nucl. Instrum. Meth.*, A447:1–8, 2000.

[70] Anthony Allen Affolder et al. CDF central outer tracker. *Nucl. Instrum. Meth.*, A526:249–299, 2004.

[71] CDF Tracking Group. see http://www-cdf.fnal.gov/internal/detectors/parameters.html and http://www-cdf.fnal.gov/cdfsim/validation/cot/cotVal.html.

[72] C. Paus et al. Design and performance tests of the CDF time of flight system. *Nucl. Instrum. Meth.*, A461:579–581, 2001.

[73] C. Grozis et al. A time of flight detector for CDF. *Int. J. Mod. Phys.*, A16S1C:1119–1121, 2001.

[74] C. Grozis et al. The time of flight detector at CDF. *Nucl. Phys. Proc. Suppl.*, 93:344–347, 2001.

[75] L. Balka et al. The CDF central electromagnetic calorimeter. *Nucl. Instrum. Meth.*, A267:272, 1988.

[76] S. Bertolucci et al. The CDF central and endwall hadron calorimeter. *Nucl. Instrum. Meth.*, A267:301, 1988.

[77] M. G. Albrow et al. The CDF plug upgrade electromagnetic calorimeter: Test beam results. *Nucl. Instrum. Meth.*, A480:524–546, 2002.

[78] C. M. Ginsburg. CDF Run II muon system. *Eur. Phys. J.*, C33:s1002–s1004, 2004.

[79] D. Acosta et al. The CDF Cherenkov luminosity monitor. *Nucl. Instrum. Meth.*, A461:540–544, 2001.

[80] D. Acosta et al. The performance of the CDF luminosity monitor. *Nucl. Instrum. Meth.*, A494:57–62, 2002.

[81] F. Abe et al. Measurement of the $\bar{p}p$ total cross-section at $\sqrt{s} = 546$ GeV and 1800 GeV. *Phys. Rev.*, D50:5550–5561, 1994.

[82] S. Klimenko, J. Konigsberg, and Tony M. Liss. Averaging of the inelastic cross sections measured by the CDF and the E811 experiments. FERMILAB-FN-0741.

[83] S. Jundariani *et al.* Luminosity uncertainty for Run II up until August 2004. CDF/ANA/7446, 2005.

[84] H.J. Frisch and P.J. Wilson. Trigger tower organization and summing in $\eta - \phi$ space for Run II and beyond. CDF/DOC/TRIGGER/CDFR/2045, 2001.

[85] The XFT system webpage. http://www.physics.ohio-state.edu/∼hughes/xft/.

[86] The XTRP webpage. http://web.hep.uiuc.edu/engin/cdf/xtrp/.

[87] I. Vila. Performance and first physics results of the SVT trigger at CDF II. 2003. hep-ph/0307165.

[88] The Trigger and Datasets Working Group. Run II trigger table and datasets plan. CDF/PHYS/TRIGGER/CDFR/4718, 2001.

[89] F. Abe et al. *Phys. Rev.*, D45:1448–1458, 1992.

[90] A. Bhatti et al. *Nucl. Instrum. Methods*, A566:2, 2006.

[91] D. Acosta et al. Measurement of the $t\bar{t}$ production cross section in $p\bar{p}$ collisions at $\sqrt{s} = 1.96$ tev using lepton + jets events with secondary vertex b-tagging. *Phys. Rev.*, D71:052003, 2005.

[92] A. Zell et al. Stuttgart neural network simulator. *http://www.ra.cs.uni-tuebingen.de/SNNS/contact.html*.

[93] T. Aaltonen et al. Search for gluino-mediated bottom squark production in $p\bar{p}$ collisions at $\sqrt{s} = 1.96$ tev. *Phys. Rev. Lett.*, 102:221801, 2009.

[94] V.M. Abazov et al. Search for pair production of scalar bottom quarks in $p\bar{p}$ collisions at $\sqrt{s} = 1.96$ tev. *Phys. Rev. Lett*, 97:171806, 2006.

[95] T. Affolder et al. Search for scalar top and scalar bottom quarks in $p\bar{p}$ collisions at $\sqrt{s} = 1.8$ tev. *Phys. Rev. Lett.*, 84:5704, 2000.

[96] H. L. Lai et al. Global QCD analysis of parton structure of the nucleon: CTEQ5 parton distributions. *Eur. Phys. J.*, C12:375–392, 2000.

[97] R. Brun et al. GEANT 3 manual, CERN Program Library Long Writeup. 1994.

[98] B. H. Harris et al. The fully differential single top quark cross-section in next to leading order qcd. *Phys. Rev. D*, 66:2002, 054024.

[99] CDF Collaboration. Combination of top pair production cross-section with 760pb^{-1}. *CDF/PHYS/TOP/PUBLIC/8148*, 2006.

[100] T. Aaltonen et al. Search for the higgs boson in events with missing transverse energy and b quark jets produced in proton-antiproton collisions at $\sqrt{s} = 1.96$ tev. *Phys. Rev. Lett.*, 100:211801, 2008.

[101] M. Cacciari. The t anti-t cross-section at 1.8-tev and 1.96-tev: A study of the systematics due to parton densities and scale dependence. *J. High Energy Phys.*, 0404:068, 2004.

[102] J. R. Campbell. An update on vector boson pair production at hadron colliders. *Phys. Rev. D*, 60:113006, 1999.

[103] A. Hocker et al. TMVA - Toolkit for Multivariate Data Analysis. *arXiv:physics/0703039*.

[104] T. Affolder et al. Search for gluinos and scalar quarks in $p\bar{p}$ collisions at $\sqrt{s} = 1.8$ tev using the missing energy plus multijets signature. *Phys. Rev. Lett.*, 88:041801, 2002.

[105] R.D. Field. Contribution to the APS/DPF/DPB Summer Study on the Future of Particle Physics (Snowmass 2001), Snowmass, Colorado, 30 June 21 July 2001 [hep-ph/0201192]; CDF Note 6403; R.D. Field (CDF Collaboration), presentations at the the 'Matrix Element and Monte Carlo Tuning Workshop', Fermilab, 4 October 2002 and 2930 April 2003, talks available from webpage http://cepa.fnal.gov/psm/MCTuning/; R. Field and R. C. Group (CDF Collaboration), hep-ph/0510198; R.D. Field (CDF Collaboration), further recent talks available from webpage http://www.phys.ufl.edu/rfield/cdf/.

[106] T. Aaltonen et al. Searches for direct pair production of supersymmetric top and supersymmetric bottom quarks in $p\bar{p}$ collisions at $\sqrt{s} = 1.96$ tev. *Phys. Rev. D*, 79:072010, 2007.

[107] V.M. Abazov et al. Search for scalar top quarks in the acoplanar charm jets and missing transverse energy final state in $p\bar{p}$ collisions at $\sqrt{s} = 1.96$ tev. *Phys. Lett. B*, 665:1, 2008.

[108] LEPSUSYWG/04-07.1. *http://lepsusy.web.cern.ch/lepsusy/*.

[109] M.L. Mangano et al. Alpgen, a generator for hard multiparton processes in hadronic collisions. *J. High Energy Phys.*, 0307:001, 2003.

[110] CDF Collaboration. Top quark pair production cross section and forward-backward asymmetry at the tevatron. *arXiv:0810.3350*, 2008.

[111] J. Campbell and K. Ellis. MCFM - Monte Carlo for FeMtobarn processes.